Technische Universität Dortmund
Fakultät Physik

Investigation of Transient Processes at the DELTA Electron Storage Ring Using a Digital Bunch-by-Bunch Feedback System

Dissertation

zur Erlangung des Doktorgrades
der Fakultät Physik
der Technischen Universität Dortmund

vorgelegt von

Markus Höner
geb. am 22.09.1986 in Werne

2015

Vorsitzender der Prüfungskomission:
Prof. Dr. Jan Kierfeld
1. Gutachter:
Prof. Dr. Shaukat Khan
2. Gutachter:
Prof. Dr. Metin Tolan
Vertreter der wissenschaftlichen Mitarbeiter:
Dr. Michael Paulus
Tag der Disputation:
1. Juli 2015

Für Katrin,
meinen Bruder
und meine Eltern

Abstract

At the 1.5-GeV synchrotron radiation source DELTA, operated by the TU Dortmund University, intensive synchrotron radiation in the spectral range from hard X-rays to THz radiation is generated by the circular deflection of highly relativistic electron bunches.
Interacting with the vacuum chamber wall, the electron bunches create electric fields, which can act back on subsequent bunches. With increasing beam current, the excitation is enhanced so that the electron beam is unstable, which means that the electron bunches oscillate longitudinally or transversely relative to their reference position. The oscillations reduce the quality of the synchrotron radiation and limit the maximum storable beam current.
Within the scope of this thesis, the beam instabilities at the storage ring were systematically investigated. A digital bunch-by-bunch feedback system was installed and commissioned, which allows to detect and digitize the position of each electron bunch at each turn. Based on the input signal, a correction signal is calculated in order to suppress transverse and longitudinal oscillation of the bunches.
In addition, it is possible to excite dedicated bunches. The systematic excitation of all coupled-bunch modes allowed for the first time to determine the damping rates of all 192 eigenmodes of the electron beam. The current dependence of the damping rates was investigated and an instability threshold was found.
Besides the investigation of multibunch instabilities, single-bunch instabilities are discussed. In addition, the acquisition unit of the digital feedback system can be triggered on external events. This was used to investigate the injection process and beam losses. It was shown that the transverse feedback system increases the injection efficiency.
Another aspect of this thesis is the improvement of the signal quality of ultrashort coherent synchrotron radiation pulses, which are generated by the short-pulse facility at DELTA. The short-pulse facility is based on coherent harmonic generation (CHG), in which an interaction of femtosecond laser pulses with electron bunches creates coherent synchrotron radiation in the VUV regime. It was shown that in hybrid mode the signal intensity can be increased by the use of the longitudinal feedback system.

Kurzdarstellung

An der 1.5-GeV Synchrotronstrahlungsquelle DELTA, betrieben von der Technischen Universität Dortmund, wird intensive Synchrotronstrahlung im Spektralbereich von harter Röntgenstrahlung bis zur THz-Strahlung durch die Kreisbeschleunigung hochrelativistischer Elektronenpakete erzeugt.
Die Elektronenpakete erzeugen durch die Wechselwirkung mit der Vakuumkammerwand elektromagnetische Felder, die auf nachfolgende Pakete zurückwirken können. Mit wachsendem Strahlstrom verstärkt sich diese Wechselwirkung, sodass der Elektronenstrahl instabil wird, d.h., dass alle Elektronenpakete anfangen um ihre Sollposition longitudinal oder transversal zu schwingen. Diese Oszillationen reduzieren zum Einen die Qualität der emittierten Synchrotronstrahlung und zum Anderen wird durch die Schwingungen der Maximalstrom begrenzt.
Im Rahmen dieser Arbeit wurden die Strahlinstabilitäten am Elektronenspeicherring DELTA systematisch untersucht. Es wurde ein digitales Regelsystem installiert und in Betrieb genommen, welches in der Lage ist, die Position jedes Elektronenpakets bei jedem Umlauf zu detektieren und zu digitalisieren. Auf Grundlage des Eingangssignals kann ein Korrektursignal berechnet werden, um sowohl transversale als auch longitudinale Schwingungen jedes Paketes zu unterdrücken.
Darüber hinaus ist es möglich, gezielt einzelne Pakete zu Schwingungen anzuregen. Die systematische Anregung aller Schwingungsmoden des Elektronenstrahls erlaubte es im Rahmen dieser Arbeit erstmalig, die Dämpfungszeiten aller 192 Eigenmoden des Elektronenstrahls zu bestimmen. Die Stromabhängigkeit der Dämpfungsraten wurde untersucht, und eine Instabilitätsschwelle für die longitudinale Oszillation gefunden.
Neben der Untersuchung von Strahlinstabilitäten mit mehreren Elektronenpaketen wurde das Verhalten eines einzelnen Elektronenpakets im Speicherring untersucht.
Die Datennahme des digitalen Regelsystems kann auf externe Ereignisse getriggert werden, was dazu verwendet wurde, den Injektionsprozess und das Auftreten von Strahlverlusten zu untersuchen. Dabei konnte gezeigt werden, dass eine transversale Dämpfung des Strahls mit Hilfe des Regelsystems eine Vergrößerung der Injektionseffizienz bewirkt.
Ein weiterer Aspekt dieser Arbeit ist die Verbesserung der Signalqualität kohärenter Synchrotronstrahlung, die im Rahmen der DELTA Kurzpulsquelle erzeugt wird. Die Kurzpulsquelle basiert auf dem Coherent Harmonic Generation Prinzip (CHG), bei dem durch die Wechselwirkung von Femtosekunden-Laserpulsen mit den Elektronenpaketen kohärente Synchrotronstrahlung im VUV-Spektralbereich erzeugt wird. Es konnte gezeigt werden, dass sich im *Hybrid*-Modus die Signalintensität durch das longitudinale Regelsystem vergrößern lässt.

Contents

1 Introduction

With the discovery of X-rays in 1895 by W.C. Röntgen [1], the basis for the study of the inner structure of materials was established. Since then, X-ray radiation evolved to an important tool in materials science, physics, chemistry, biology and medicine. Typically, X-ray radiation is created in an X-ray tube, where a thermionic cathode emits electrons, which are accelerated and hit an anode. Due to the sudden deceleration, bremsstrahlung and characteristic X-ray radiation is emitted. Since the radiation is emitted into a large solid angle, the intensity is typically too small for the requirements of modern science. Nowadays, intense X-ray radiation is created in electron storage rings or free-electron lasers.

1.1 Synchrotron Radiation

Synchrotron radiation is electromagnetic radiation emitted by the circular acceleration of highly relativistic charged particles, usually electrons, in a magnetic field. The emitted synchrotron radiation covers a photon energy range from the THz regime to high-energy X-rays. The first direct observation of synchrotron radiation was made in 1947 at the 70-MeV synchrotron of General Electric [2]. In a simplified treatment, the radiation results from the fact that the electric field lines of a highly relativistic electron can not instantly follow the acceleration of the electron, but are subject to retardation. While for a static electron (Fig. 1a), the electric field lines are diverging isotropically, a circular acceleration of highly relativistic electrons creates a shockwave propagating with the velocity of light (Fig. 1b/c).

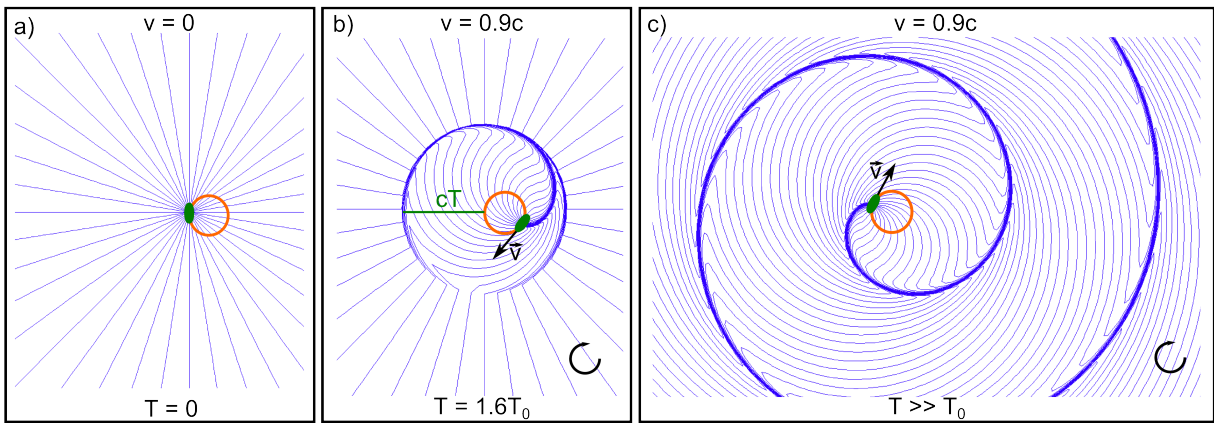

Figure 1: Electric field lines (blue) of a particle (green) on a circular path (orange). Shown is the particle at rest (a), for a particle velocity $v = 0.9\,\mathrm{c}$ after 1.6 turns (b) and after several turns (c). The radiation shockwave propagates with the velocity of light c. The field distribution was calculated using the code Radiation2D [3].

Due to the high photon flux density compared to other radiation sources, synchrotron radiation quickly evolved to an important instrument for materials science. The first dedicated electron storage ring (Tantalus I in Wisconsin) was built in 1968 [4]. Ever since, many other facilities were built, providing synchrotron radiation from bending magnets. In order

to increase the photon flux density, so-called undulators and wigglers were installed in the storage ring, starting in the 1970s [5]. These devices deflect the electrons periodically, which improves the radiation quality. A figure of merit of the quality of the radiation is the spectral brightness (e.g. [6])

$$B = \frac{\dot{N}_\gamma}{4\pi^2 \sigma_x \sigma_y \sigma_{x'} \sigma_{y'} \Delta E/E_\gamma}$$

with the rms size of the spatial distribution $\sigma_{x,y}$, the rms size of the angular distribution $\sigma_{x',y'}$ and the the photon flux $\dot{N}_\gamma$. The energy interval $\Delta E/E_\gamma$ is often defined to be a range of 0.1% of the respective photon energies. Since an undulator has a small spectral bandwidth and a small angular divergence, it has a much higher brightness compared to a wiggler or dipole magnet.

1.2 Beam Instabilities

Many efforts were made in the last decades to increase the brilliance of synchrotron radiation, which means decreasing the source size and angular divergence of the radiation and increasing the electron beam current. The electrons interact with the surrounding vacuum chamber, which creates electromagnetic fields that can act back on other electrons inside the bunch or in the following electron bunches. Due to the high beam current, these effects become more and more important and result in different types of collective instabilities (e.g.[7, 8]). In case of a long-range interaction between different bunches, the bunches perform so called coupled-bunch oscillations, which were theoretically described by Sacherer in the 1970s [9, 10]. The growth rate $1/\tau$ of the oscillation amplitude is proportional to the number of electrons N_e. Due to different damping mechanisms in an electron storage ring, there is a certain threshold for the beam current above which these instabilities show up. The instabilities reduce the brilliance of the radiation or even cause a beam loss. While a transverse oscillation of the electron bunches increases the time-averaged size and angular divergence of the radiation pulses, a longitudinal oscillation implies an additional energy spread, which results in a broadening of the line width of undulator spectra.

1.2.1 Cures of Beam Instabilities at DELTA

The 1.5-GeV electron storage DELTA is operated by the Center for Synchrotron Radiation [11] of the TU Dortmund University as a synchrotron radiation source and for research in accelerator physics. The first beam was injected into the storage ring in 1996 [12]. Since 2000, the facility is in continuous operation [13].
At DELTA, different approaches aim at the characterization and suppression of beam instabilities in order to increase the brilliance of the synchrotron radiation.
In 2004, the DORIS-type RF cavity used for the compensation of energy losses of the electron bunches due to synchrotron radiation, was characterized. It was possible to assign some of the

observed multibunch modes to the higher-order modes (HOMs) of the cavity [14]. In order to suppress these cavity-induced instabilities, a cavity prototype with additional damping ports was installed in 2004 [15, 16] and no more cavity-induced instabilities were observed [17]. However, other multibunch instabilities were still excited, the source of which could not be localized in the storage ring. Even though the operation of the damped cavity was successful in terms of suppressing beam instabilities, it was removed after one year of operation due to vacuum leaks and cooling problems. It was replaced by the initial DORIS-type cavity, which was upgraded using ferrite-damping antennas [18]. With this configuration, the same multibunch modes were suppressed as with the HOM-damped cavity [19], so that the source of the remaining instabilities is still not known.

A further approach to increase the brilliance of the storage ring was the insertion of an additional passive 3rd-harmonic cavity in 2007 [20]. With a variable plunger, the resonance frequency could be varied, resulting in a lengthening of the electron bunches. This resulted in a reduction of the scattering between the electrons (Touschek scattering) which increased the lifetime of the electron beam. Since the passive cavity influenced the bunch length of the beam, even if the plunger was moved to the neutral position, the cavity was removed after a short test period.

In 2009, a remote-controllable phase modulation of the RF-generator voltage, which drives the klystron of the cavity, was added [21]. This phase modulation suppresses all multibunch instabilities in standard beam operation. In addition, the phase modulation results in a higher average bunch length, which increases the beam lifetime. In contrast to a 3rd-harmonic cavity, the system can be completely switched off e.g. for the operation of the DELTA short-pulse facility, where a high electron density and therefore a short bunch length is required.

In order to suppress beam instabilities without bunch lengthening, a bunch-by-bunch feedback system was tested in 2009 showing the capabilities of such a system [22]. In 2011, a bunch-by-bunch feedback system was permanently installed and commissioned as part of this thesis [23, 24].

1.2.2 Bunch-by-Bunch Feedback Systems

A bunch-by-bunch feedback system detects the position of every bunch over several turns and creates a correction signal, which acts back on the bunch in order to damp its oscillation (see Fig. 2). The feedback system at DELTA operates in the longitudinal, horizontal and vertical plane independently. Since the beam position of every bunch at every turn is digitized over several thousand turns, the feedback system is a powerful tool for the analysis of transient processes of the electron beam, e.g. the injection of bunches into the storage ring.

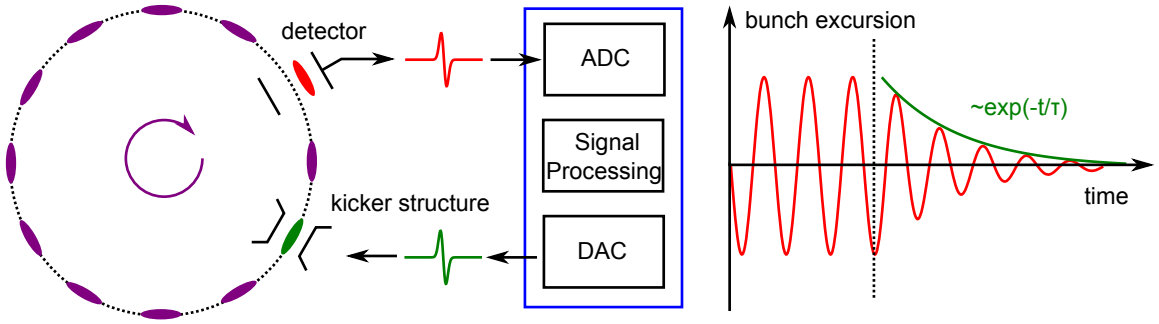

Figure 2: Sketch of the basic operation scheme of a digital bunch-by-bunch feedback system. The feedback loop contains the detector to determine the bunch position, the analog-to-digital converter (ADC) to digitize the data, the signal processing unit which calculates the output signal, the digital-to-analog converter (DAC) to create the analog correction signal, the kicker structure and the electron beam. When the feedback loop is closed (right, dashed line), the bunch oscillation shows an exponential damping behaviour. Typically, the damping time τ is in the millisecond regime.

1.3 Goal of this Thesis

The goal of this thesis is the investigation of beam instabilities and transient processes at the electron storage ring DELTA. A digital bunch-by-bunch feedback system is in use to measure the longitudinal and transverse beam position and to temporarily excite beam instabilities in order to investigate the damping behaviour of beam instabilities and the coupling mechanism between different bunches. In particular, the excitation of only a dedicated fraction of the bunch train to investigate the coupling to the other bunches is a new approach. Besides these measurements, a simulation tool was created in order to simulate the longitudinal coupling of these bunches due to higher-order modes of the accelerating cavity and other resonant elements. In addition, the benefits of the bunch-by-bunch feedback system to the short-pulse-facility are presented. An overview of the transverse and longitudinal electron beam dynamics is given in Sect. 2, while Sect. 3 introduces the relevant instability mechanisms. In Sect. 4, the requirements and limitations of digital bunch-by-bunch feedback systems are discussed. In order to cross-check the bunch-coupling measurements described later, the simulation of beam-cavity interactions is discussed in Sect. 5. Section 6 gives an overview of the DELTA synchrotron light source including the DELTA short-pulse facility. Section 7 gives an overview of the experimental setup and describes in detail the bunch-by-bunch feedback system. Finally, Sects. 8 and 9 show the experimental results, which are compared with simulation results. Sect. 8 focuses on the the analysis of beam instabilities at the DELTA storage ring, while Sect. 9 shows the use of the bunch-by-bunch feedback system in order to investigate transient processes at DELTA such as the injection into the storage ring and the benefits of the feedback system to the short-pulse facility. Finally, first measurements at the booster synchrotron BoDo are presented.

2 Electron Beam Dynamics

In this section, the electron beam dynamics in a accelerator or storage ring is discussed.

2.1 Coordinate System

Highly-relativistic electrons move with almost the velocity of light and have a total energy which is orders of magnitudes larger than their rest energy. In a particle accelerator or storage ring, these electrons are held on a closed path (orbit) by magnetic fields, which are generated by dipole and quadrupole magnets.
Due to synchrotron radiation, the electrons lose energy continuously. The lost energy is restored by RF cavities.
In order to describe the propagation of all particles through the ring, the following formalism is used (see e.g. [25]). The position of every particle is given by the 6-element vector

$$\begin{pmatrix} x \\ x' = \frac{dx}{ds} \\ y \\ y' = \frac{dy}{ds} \\ z \\ \delta E \end{pmatrix} \hat{=} \begin{pmatrix} \text{horizontal displacement} \\ \text{horizontal angle} \\ \text{vertical displacement} \\ \text{vertical angle} \\ \text{longitudinal displacement} \\ \text{relative energy deviation} \end{pmatrix}. \tag{2.1}$$

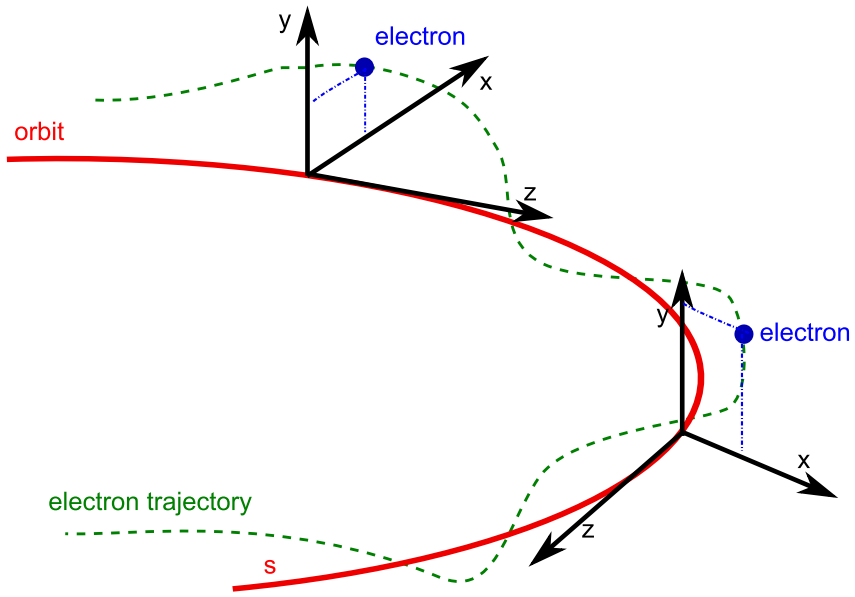

Figure 3: The co-moving coordinate system (black) moves along the orbit in order to describe the electron position (blue) relative to an ideal particle following the orbit (red). An individual electron trajectory is shown as dashed line (green).

The 6-element position vector is a function of the position s along the orbit. The longitudinal coordinate z is tangential to the orbit and points in the direction the beam is circulating. The horizontal coordinate x is perpendicular to z and points outside the ring. Assuming that the beam is rotating clockwise, the vertical coordinate y forms a right-handed orthogonal system with x and z. The coordinate system co-propagates with a ideal particle along the orbit and rotates in the laboratory frame (see Fig. 3).
In order to calculate the propagation of the electrons from a starting position s_0 to an arbitrary position s_1 in the ring, the following general transfer matrix is applied

$$\begin{pmatrix} x \\ x' \\ y \\ y' \\ s \\ \delta E \end{pmatrix}_{s_1} = \begin{pmatrix} r_{11} & r_{12} & 0 & 0 & 0 & r_{16} \\ r_{21} & r_{22} & 0 & 0 & 0 & r_{26} \\ 0 & 0 & r_{33} & r_{34} & 0 & 0 \\ 0 & 0 & r_{43} & r_{44} & 0 & 0 \\ r_{51} & r_{52} & 0 & 0 & 1 & r_{56} \\ 0 & 0 & 0 & 0 & 0 & 1 \end{pmatrix} \begin{pmatrix} x \\ x' \\ y \\ y' \\ s \\ \delta E \end{pmatrix}_{s_0} . \tag{2.2}$$

While the horizontal and longitudinal planes are coupled, the vertical plane is independent from the other planes. In the next section, the basic mechanisms of the transverse and longitudinal propagation of electrons in a storage ring are explained.

2.2 Transverse Beam Dynamics

2.2.1 Single Particle

In a first step, the transverse dynamics of all electrons can be considered as independent motion of single particles. The transverse equation of motion for each electron is given by [25, 26]

$$x''(s) + \left(\frac{1}{R(s)} - k(s) \right) x(s) = \frac{\delta_E}{R(s)} \tag{2.3}$$

and

$$y''(s) + k(s)y(s) = 0 \tag{2.4}$$

with the position-dependent bending radius of the dipole magnets $R(s)$, the focusing strength of the quadrupole magnets $k(s)$ and the relative energy deviation $\delta_E = \Delta E/E$. This results in a quasi-harmonic oscillation, called betatron oscillation (e.g. [25, 26]), of the single particle around the beam orbit given by

$$x(s) = \sqrt{\varepsilon_x \beta_x(s)} \cdot \cos\left(\mu_x(s)\right) + D_x(s)\delta_E \tag{2.5}$$

and

$$y(s) = \sqrt{\varepsilon_y \beta_y(s)} \cdot \cos\left(\mu_y(s)\right) .$$

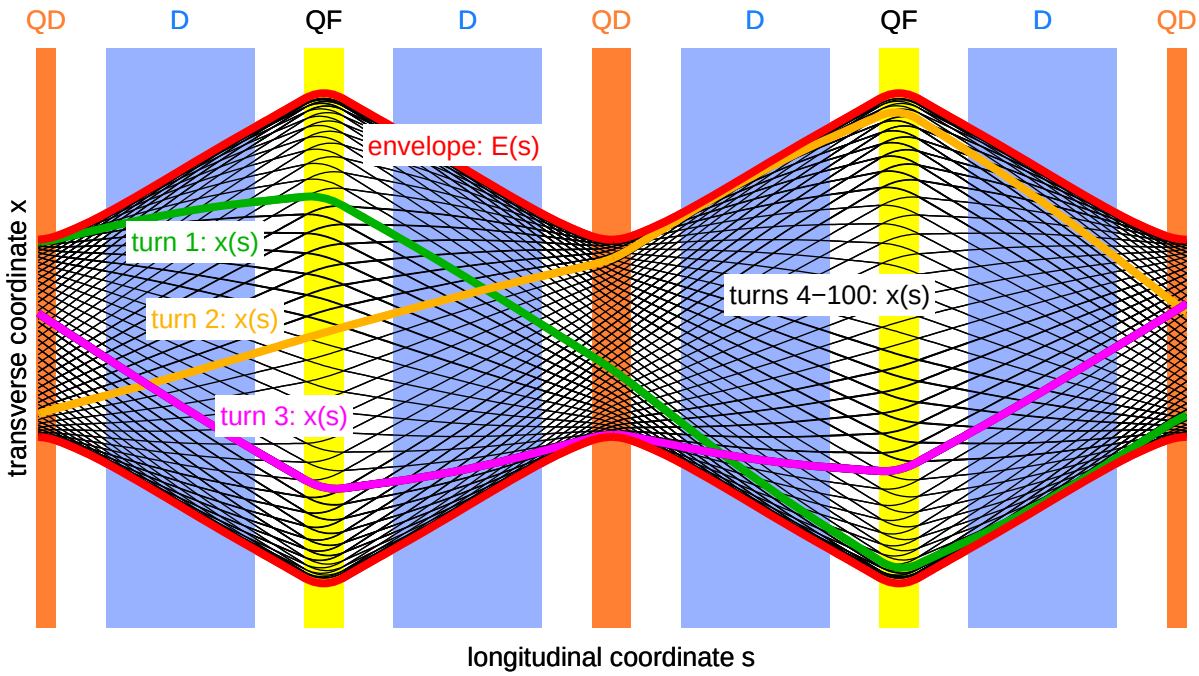

Figure 4: Electron propagation in a storage ring consisting of dipole magnets (D), focusing quadrupoles (QF) and defocusing quadrupoles (QD). The single-particle trajectory is shown for 100 turns. In this example, a particle without energy deviation was assumed. The particle envelope (red) is given by the maximum displacement of all turns.

The phase $\mu_{x,y}(s)$ is called betatron phase. The envelope $E_{x,y}(s) = \sqrt{\varepsilon_{x,y}\beta_{x,y}(s)}$ is given by the so-called Courant-Snyder invariant $\varepsilon_{x,y}$ [27] of the electron, and the position-dependent beta function $\beta_{x,y}(s)$. The dispersion function $D_x(s)$ is the particular solution of Eq. 2.3 divided by δ_E and accounts for the energy-dependent horizontal displacement in the dipole magnets.

In Fig. 4, the horizontal electron trajectory of one electron is plotted for a FODO lattice comprising two focusing and two defocusing quadrupoles with four dipole magnets in between. The electron propagates linearly between the magnets and is focused or defocused by the magnets. The beta-function $\beta(s)$ and the functions

$$\alpha(s) = -\frac{\beta'(2)}{2}, \tag{2.6}$$

$$\gamma(s) = \frac{1+\alpha^2}{\beta(s)} \tag{2.7}$$

are called optical function or Twiss parameters. These parameters can be calculated if the transfer matrix for one entire revolution is known (one-turn matrix) which is calculated as the matrix product of the transfer matrices of each individual magnet. The individual transfer matrices of each magnet are obtained by step-wise solving Eq. 2.3 for a constant parameter $k(s)$ and $R(s)$, respectively. For a fixed position s_0, optical functions can be derived from

the one-turn matrix by using the periodicity condition $\beta(s_0) = \beta(s_0 + L)$, which results, e.g. for the horizontal plane, in [26]

$$\beta_x(s_0) = \frac{2 \cdot |r_{12}|}{\sqrt{2 - r_{11}^2 - 2 \cdot r_{21} r_{11} - r_{22}^2}}, \tag{2.8}$$

$$\alpha_x(s_0) = \frac{r_{11} - r_{22}}{2 \cdot r_{12}} \cdot \beta_x(s_0). \tag{2.9}$$

Once the optical function at one position are known, the values of the optical functions around the ring can be calculated by 3x3 matrices using the matrix elements of the transfer matrix for a single electron according to

$$\begin{pmatrix} \beta_x \\ \alpha_x \\ \gamma_x \end{pmatrix}_{s_1} = \begin{pmatrix} r_{11}^2 & -2r_{11}r_{12} & r_{12}^2 \\ -r_{11}r_{21} & r_{11}r_{22} + r_{12}r_{21} & -r_{12}r_{21} \\ r_{21}^2 & -2r_{22}r_{21} & r_{22}^2 \end{pmatrix} \begin{pmatrix} \beta_x \\ \alpha_x \\ \gamma_x \end{pmatrix}_{s_0}. \tag{2.10}$$

The Courant-Snyder invariant or single-particle emittance $\varepsilon_{x,y}$ is a constant value for each particle. In the horizontal plane, as an example, it is given by

$$\varepsilon_x = \gamma_x(s)x^2(s) + 2\alpha_x(s)x(s)x'(s) + \beta_x(s)x'^2(s), \tag{2.11}$$

which is an equation of an ellipse in horizontal phase space. Therefore, for a fixed position in the ring, each particle follows an ellipse in x-x' phase space.
As an example, the beta function $\beta_{x,y}(s)$ and dispersion $D_x(s)$ of the DELTA storage ring are shown in Fig. 5.

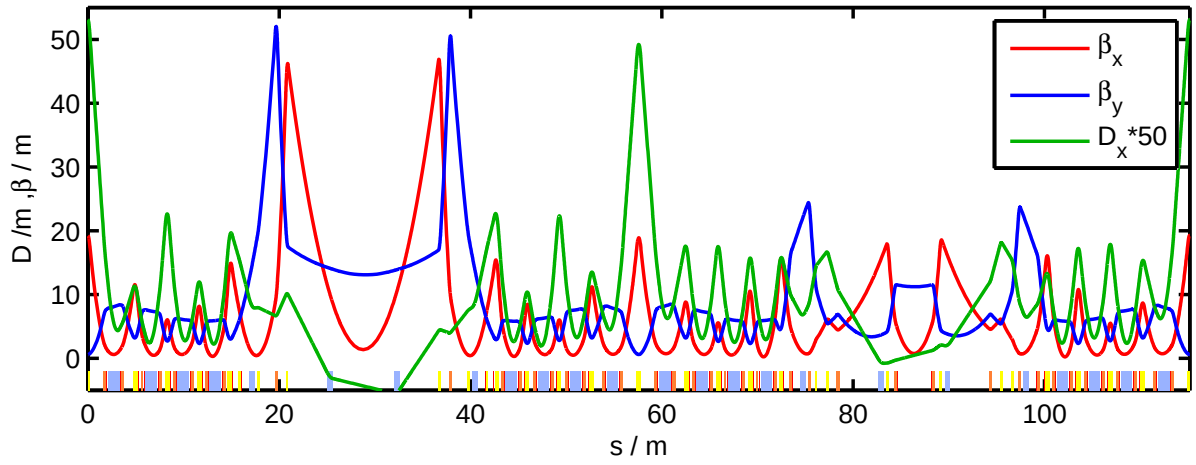

Figure 5: Horizontal (red) and vertical (blue) beta function $\beta_{x,y}(s)$ and the dispersion $D_x(s)$ (green) of the DELTA storage ring as a function of the position s. The symbols at the bottom indicate the position of dipole magnets (light blue), horizontally focusing quadrupoles (yellow) and horizontally defocusing quadrupoles (orange). For better visibility, the dispersion is scaled by a factor of fifty.

The betatron phase $\mu_x(s)$ can be expressed in terms of the beta function according to

$$\mu_x(s) = \int_0^s \frac{1}{\beta_x(\bar{s})} d\bar{s}. \tag{2.12}$$

Since a phase advance of 2π corresponds to one oscillation, dividing the phase advance by 2π yields the number of oscillations per turn

$$Q_x = \frac{1}{2\pi}\mu_x(s) = \frac{1}{2\pi}\int_0^s \frac{1}{\beta_x(\bar{s})} d\bar{s}, \tag{2.13}$$

which is called betatron tune. To avoid resonances, the betatron tunes Q_x and Q_y must be chosen in a way that the resonance condition

$$m \cdot Q_x + n \cdot Q_y = p \quad (m,n,p \in \mathbb{N})$$

is not fulfilled. Since the strength of a resonance decrease with the order of the resonance $|m| + |n|$, it is typically sufficient to take care about resonances of the 5th order [26]. In addition, the focusing strength of the quadrupole magnets depends on energy deviation of the electrons, which results in a deviation of the betatron tune. This energy dependence of the betatron tune is expressed by the chromaticity

$$\xi_{x,y} \quad = \frac{\Delta Q_{x,y}}{\Delta E/E} \quad . \tag{2.14}$$

Typically, the natural chromaticity is negative which gives rise to head-tail instabilities (see Sect. 3.4). The chromaticity can be increased to even positive values by placing sextupole magnets at locations with dispersion. In that case, the chromaticity is given by

$$\xi_{x,y} = \frac{1}{4\pi} \oint \left[m(s) D_x(s) - k(s)\right] \beta_{x,y}(s) ds \tag{2.15}$$

with the sextupole strength $m(s)$.

2.2.2 Particle Ensemble

In standard operation of a storage ring, several billion particles are stored simultaneously, which all have their individual Courant-Snyder invariant. The particles have different positions and energies with respect to the ideal particle and are typically Gaussian distributed in each coordinate. In the horizontal phase space, as an example, the electron distribution is given by

$$\rho(x,x') = \frac{N}{2\pi\sigma_x\sigma_{x'}} \cdot \exp\left(-\frac{x^2}{2\sigma_x^2}\right) \cdot \exp\left(-\frac{x'^2}{2\sigma_{x'}^2}\right) \tag{2.16}$$

with the number of electrons N and the standard deviation of the position σ_x and angle $\sigma_{x'}$. The Courant-Snyder invariant of a particle with an excursion $x(s_0) = \sigma_x(s_0)$ and

$x'(s_0) = \sigma_{x'}(s_0)$ defines the beam emittance ε_x, which is typically in the order of 10 nm · rad. The electrons in the storage ring are not distributed along the entire ring but are bunched (see Sect. 2.3). These bunches can perform center-of-mass oscillation corresponding to a single-particle trajectory. While the single-particle oscillation is not detectable, these collective oscillations of the entire bunch are observable at a beam position monitor (BPM). The BPM signal and especially the beam spectrum will be discussed in Sect. 3.2.1.

2.3 Longitudinal Beam Dynamics

Due to synchrotron radiation, the electrons lose energy while circulating in the storage ring according to [26]

$$eV_{\text{loss}} = \frac{e^2}{3\varepsilon_0 \left(E_0\right)^4} \cdot \frac{E^4}{R} \tag{2.17}$$

with the bending radius of the dipole magnets R, the beam energy E, the rest energy E_0, the vacuum permittivity ε_0 and the elementary charge e. This energy must be recovered by passing the electric field of the accelerating RF cavity which yields

$$eV_0 \cdot \sin\left(\Psi_S\right) = eV_S = E_S \tag{2.18}$$

with the cavity voltage V_0 and the so-called synchronous phase Ψ_s. Since the cavity has a higher maximum voltage than needed to compensate for energy losses, also particles which have a small energy deviation from the design energy can be stored, which leads to a longitudinal oscillation relative to the synchronous phase. The longitudinal phase space motion of the electron turn by turn is given by a system of non-linear differential equations [26]

$$\frac{d}{dt}\left(\frac{\Delta E}{E}\right) = \frac{eV_0}{T_0 E} \cdot \left[\sin\left(\Psi_S + \Delta\Psi\right) - \sin\left(\Psi_S\right)\right] - \frac{1}{T_0}\frac{dE_{\text{S}}}{dE}\frac{\Delta E}{E} \tag{2.19}$$

and

$$\frac{d}{dt}\Delta\Psi = \frac{2\pi h\alpha}{T_0} \cdot \frac{\Delta E}{E}. \tag{2.20}$$

There, h is the harmonic number of the storage ring, which is the RF frequency divided by the revolution frequency and $\alpha = (\Delta L/L)/(\Delta E/E)$ is the momentum-compaction factor, which is a measure for the longitudinal displacement of an off-energy particle. The momentum compaction factor is given by

$$\alpha = \frac{1}{L}\oint \frac{D_x(s)}{R(s)} ds \tag{2.21}$$

with the circumference of the storage ring L.
A simulation of the longitudinal phase-space motion of the particles, based on the DELTA parameters, is shown in Fig. 6.

In the range of the phases

$$\Psi_n = \Psi_S + n \cdot 2\pi \text{ with } n \in [0,h-1], \tag{2.22}$$

stable and closed trajectories (rainbow colors in the plot) are possible. Due to these so-called RF buckets, the electron beam is divided in up to h bunches. For small deviations from the design energy or phase, respectively, the trajectory in the longitudinal phase space is a ellipse, which corresponds to a harmonic oscillation. The oscillation frequency of this so-called synchrotron oscillation is given by [25]

$$\omega_s = \sqrt{-\frac{2\pi e V_0 h \alpha \cos(\Psi_S)}{E T_0^2}}. \tag{2.23}$$

Dividing the synchrotron frequency by the revolution frequency results in the synchrotron tune Q_S, which is far below one.
For larger oscillation amplitudes, the motion is anharmonic and the synchrotron frequency is decreased, which results in a tune spread of the ensemble of electrons. The area of closed trajectories in phase space is separated from the unstable trajectories by the so-called separatrix.

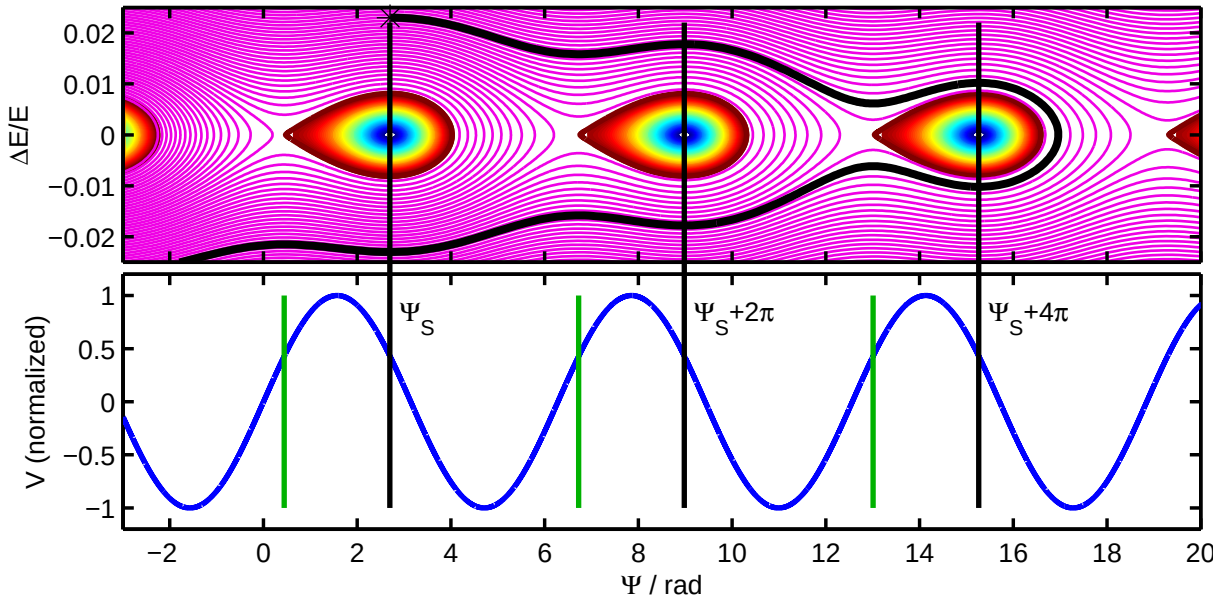

Figure 6: Longitudinal phase space of the DELTA storage ring (top).The stable regimes of the electrons are depicted in rainbow colors, while all unstable trajectories are plotted in magenta. The bold-black trajectory indicates a particle which starts at the synchronous phase, but has an energy deviation which is larger than the energy acceptance. In addition, the corresponding RF voltage is plotted (bottom). The synchronous phase indicating the center of the stable buckets is marked by vertical black lines. The phases which provide the correct RF voltage but no phase-focusing are marked with vertical green lines.

3 Instability Mechanisms

There are several different types of beam instabilities in an electron storage ring, which all lead either to an emittance growth of the electron beam or to beam loss, which usually based on the following mechanisms.

Electrons in the electron bunch create an electric field due to their charge. In the reference frame of the electron, the electric field-lines extend symmetrically in all directions. In case of highly-relativistic electrons, as it is the case in a storage ring, the field lines are longitudinally Lorentz-contracted in the laboratory frame. This and the boundary conditions of the vacuum chamber result in transverse field lines as depicted in Fig. 7a. Here, a perfectly conducting vacuum chamber is assumed, so that no electric fields are present at the position of the following particle.

In case of a non-zero resistance of the vacuum chamber, the wall current which co-propagates with the source particle, lags behind which produces delayed electromagnetic fields (wake fields). Depending on the geometry and conductivity of the chamber, the electromagnetic fields are still present when the next particle passes the chamber section, where the wake fields were created. This results in a net force on that particle (see Fig. 7b).

A similar effect occurs whenever the electron passes a part of the vacuum chamber, at which the chamber cross section suddenly changes. Since the wall current is not able to follow the electron immediately, again an electromagnetic field (wake field) is produced that can act back on subsequent particles. In case of a resonant structure, for example a cavity (see Fig. 7c), these wake fields have a large decay time. Also the source particle loses energy by creating these wake fields, which has to be compensated by the RF cavity.

The wakefields described above can lead to a transverse or longitudinal oscillation of the particles about their equilibrium position. In addition, beam instabilities can be categorized by the range on which different electrons interact with each other. On the one hand, there are instabilities, which result from a cross-talk of different bunches (long range), on the other hand there are instabilities which occur inside the electron bunch (short range).

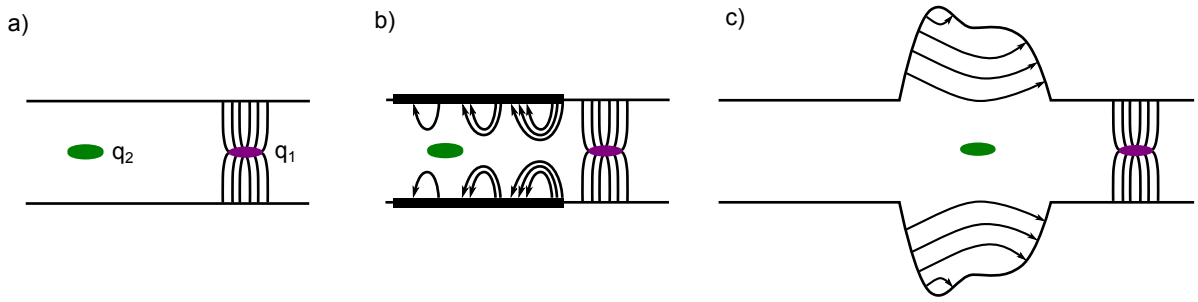

Figure 7: Source particle (purple) propagating in a perfectly conducting vacuum chamber (a) and in a resistive vacuum chamber (b). The subsequent particle (green) is influenced by the wake fields created by the finite resistivity of the vacuum chamber (b) or by cavity-like structures creating slow decaying wake fields (c).

3.1 Wake Function and Impedance

In order to quantify the net force of a source particle on subsequent particles, the formalism of wake functions and impedances is used. The following definitions are in compliance with the definitions given for example in Ref. [7, 28, 29, 30, 31, 32].

The wake function is defined as the integral of the force $\vec{F}_1$ of the source particle q_1 on the target particle q_2 over the structure length L which may be the length of a cavity but may also be the total accelerator circumference. This yields

$$\vec{W}(t) \;=\; -\frac{c}{q_1 q_2}\int_L \vec{F}_1(t)dt\,. \tag{3.1}$$

The longitudinal wake function $W_\parallel$ is given by

$$W_\parallel(t) = \frac{c}{q_1 q_2}\int_L q_1 E_z(t)dt = \frac{1}{q_2}\int_L E_z(t)dt \tag{3.2}$$

with the longitudinal electric field component $E_z(t)$ of the source particle. The longitudinal wake function can be interpreted as the energy gain ΔU per unit charge of the two particles

$$W_\parallel(t) = -\frac{\Delta U}{q_1 q_2}. \tag{3.3}$$

Analogously, the transverse wake function is given by

$$\vec{W}_\perp(t) = \frac{c}{q_1 q_2}\int_L q_1 \left[\vec{E}_1(t) + \vec{v}_1 \times \vec{B}_1(t)\right]_\perp dt. \tag{3.4}$$

Here, the magnetic field $\vec{B}$ must be taken into account. In the expression of the longitudinal wake function, the magnetic field was neglected due to the small transverse particle velocity relative to the longitudinal velocity. However, in an axis-symmetric structure, a source particle which is traveling on axis can not produce a net transverse force on a subsequent particle which is following on the same axis. To achieve a net transverse force, a breaking of the symmetry is necessary, which for example occurs if either the source particle or the subsequent particle is transversely displaced.

The wake function is very useful for macro-particle simulations in the time domain, where it can be used to describe the driving force of the equation of motion. However, analytical calculations are often based on the frequency-domain representation of the wake function, the impedance, which is given by the Fourier transform of the wake function

$$Z_\parallel(\omega) \;=\; \int_{-\infty}^{\infty} W_\parallel(t)\cdot\exp\left(-i\omega t\right)dt \tag{3.5}$$

and

$$Z_\perp(\omega) = i\int_{-\infty}^{\infty} W_\perp(t)\cdot\exp\left(-i\omega t\right)dt \tag{3.6}$$

with an additional phase factor i. As an example, the longitudinal and transverse impedance and wake function is depicted in Fig. 8 for the case of a weakly damped resonator.

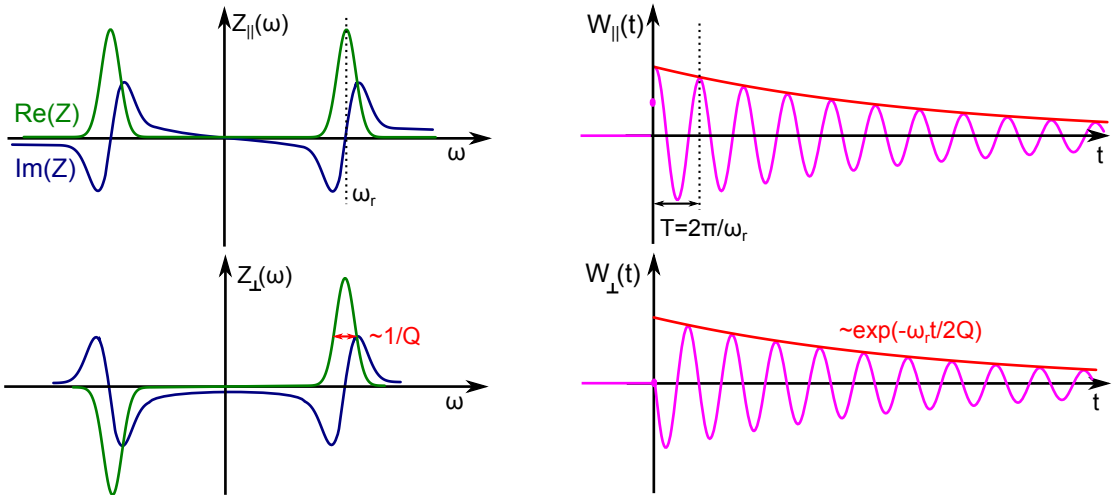

Figure 8: Sketch of transverse ($\perp$) and longitudinal ($\parallel$) impedance $Z(\omega)$ and wake function $W(t)$ of a weakly damped resonator. See list below for details.

From this example, several general properties of the impedance and the wake function can be derived, which are summarized in the following list ([8, 31, 32]):

- $W_\parallel(t) = 0$ and $W_\perp(t) = 0$ for $t < 0$. This results from the fact that for ultra-relativistic particles there is no wake field in front of the particle due to causality.
- The envelope of the wake functions depend on how quickly stored energy is dissipated, which is quantified by the quality factor Q of the corresponding structure.
- The oscillation period of the wake function depends on the resonant frequency ω_r of the corresponding structure.
- $W_\perp(0^+) < 0$, since subsequent particles are deflected in the same direction the source particle was deflected.
- $W_\perp(0) = 0$, since the source particle has only longitudinal momentum and can therefore not lose energy in the transverse plane.
- $W_\parallel(0^+) > 0$, since the subsequent particle is decelerated by the source particle.
- $W_\parallel(0)$ is related to the energy lost by the source particle itself when creating the wake. It is given by $\frac{1}{2} \cdot W_\parallel(0^+)$, which is known as the fundamental theorem of beam loading [33].
- $\mathrm{Re}\left\{Z_\parallel(\omega)\right\} = \mathrm{Re}\left\{Z_\parallel(-\omega)\right\}$ and $-\mathrm{Im}\left\{Z_\parallel(\omega)\right\} = \mathrm{Im}\left\{Z_\parallel(-\omega)\right\}$.
- $-\mathrm{Re}\left\{Z_\perp(\omega)\right\} = \mathrm{Re}\left\{Z_\perp(-\omega)\right\}$ and $\mathrm{Im}\left\{Z_\perp(\omega)\right\} = \mathrm{Im}\left\{Z_\perp(-\omega)\right\}$.

In the case of an extended charge distribution $j(t)$, the so-called wake potential $V(t)$ is obtained by a convolution of the wake function and the charge density

$$V_{\parallel}(t) \quad = \quad \int_{-\infty}^{\infty} W_{\parallel}(\tau) \cdot j(t-\tau) d\tau \tag{3.7}$$

and

$$V_{\perp}(t) = \int_{-\infty}^{\infty} W_{\perp}(\tau) \cdot j(t-\tau) d\tau \,. \tag{3.8}$$

Its Fourier transform is the product of the individual Fourier transform of the factors resulting in

$$\tilde{V}_{\parallel}(\omega) \quad = \quad Z_{\parallel}(\omega) \cdot J(\omega) \tag{3.9}$$

and

$$\tilde{V}_{\perp}(\omega) = i \cdot Z_{\perp}(\omega) \cdot J(\omega), \tag{3.10}$$

where $J(\omega)$ is the Fourier transform of the charge distribution. A knowledge of the impedance of the machine and the beam spectrum directly allows to calculate the frequency-dependent voltage that is induced by the wake fields. Therefore, the next section focuses on typical beam spectra which occur in an electron storage ring. In Sect. 3.3 and Sect. 3.4, the most relevant instability mechanisms for the DELTA storage ring are discussed.

3.2 Beam Spectra

The time-domain signal of the electron beam $j(t)$ at one beam-position monitor (BPM) and the corresponding beam spectrum $j(\omega)$ are connected by a Fourier transformation

$$J(\omega) = \int_{-\infty}^{\infty} j(t) e^{-i\omega t} dt \tag{3.11}$$

and

$$j(t) = \frac{1}{2\pi} \int_{-\infty}^{\infty} J(\omega) e^{i\omega t} d\omega, \tag{3.12}$$

respectively. The calculation of the Fourier transform in the following was derived in analogy to Ref. [8, 7, 34].

3.2.1 Stable Beam

A point-like electron bunch circulating in a storage ring provides one signal at a beam position monitor (BPM) every turn. Therefore, the measured beam current over time is

given by

$$j(t) = \sum_{n=-\infty}^{n=\infty} \delta(t - nT_0) \tag{3.13}$$

with the number of turns n and the revolution time T_0. The Fourier transform is given by

$$J(\omega) = \sum_{n=-\infty}^{n=\infty} \int_{-\infty}^{\infty} \delta(t - nT_0) e^{-i\omega t} dt = \sum_{n=-\infty}^{n=\infty} e^{-i\omega n T_0}. \tag{3.14}$$

This can be simplified by Poisson's sum rule (e.g. [35]) which implies that

$$\sum_{n=-\infty}^{n=\infty} f(\alpha n) = \frac{1}{\alpha} \sum_{n=-\infty}^{n=\infty} \mathcal{F}\left(\frac{2\pi n}{\alpha}\right), \tag{3.15}$$

if $\mathcal{F}$ is the Fourier transform of f. With $f(t) = e^{-i\bar{\omega}t}$, $\mathcal{F}(\omega) = 2\pi\delta(\omega - \bar{\omega})$ and $\alpha = T_0$. Therefore, Eq. 3.14 yields

$$J(\omega) = \omega_0 \sum_{n=-\infty}^{n=\infty} \delta(\omega - n\omega_0) \tag{3.16}$$

with the revolution frequency $\omega_0 = 2\pi/T_0$. Therefore, the beam spectrum is a comb of lines at the revolution frequency harmonics. In case of extended charge distribution (convolution in time domain), the beam spectrum is multiplied by the single-bunch distribution, which results in a suppression of the high frequency components (see Fig. 9).

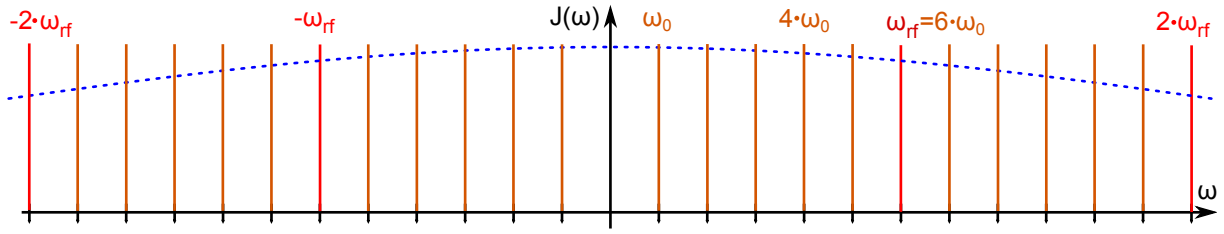

Figure 9: Spectrum of a single bunch. The dashed blue line indicates suppression of high-frequency components due to a finite bunch length.

In case of a complete fill of all h RF buckets, the corresponding beam current

$$j(t) = \sum_{p=-\infty}^{p=\infty} \delta(t - p\frac{T_0}{h}) \tag{3.17}$$

results in the beam spectrum

$$J(\omega) = h \cdot \omega_0 \sum_{p=-\infty}^{p=\infty} \delta(\omega - p \cdot h \cdot \omega_0). \tag{3.18}$$

For a real storage ring, in which the bunch current of each bucket is not identical, also the

revolution frequency harmonics show up in the beam spectrum as depicted in Fig. 10.

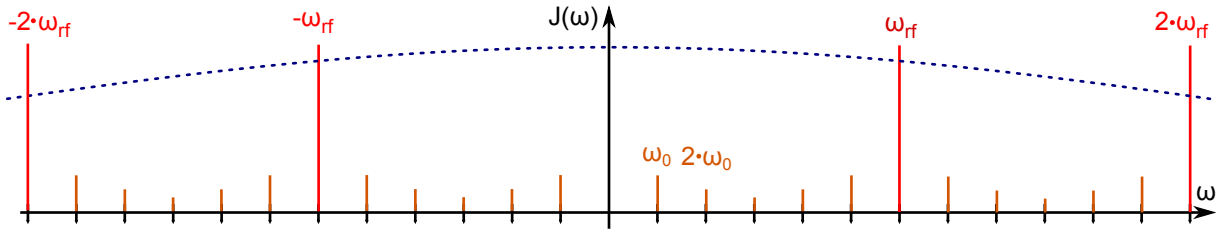

Figure 10: Spectrum of six bunches. The dashed blue line indicates suppression of high-frequency components due to a finite bunch length. The revolution harmonics are strongly reduced.

3.2.2 Longitudinal Oscillation

In case of a collective longitudinal oscillation of a single bunch, which might be driven by wake fields, the beam current can be expressed as

$$j(t) = \sum_{n=-\infty}^{n=\infty} \delta\left(t - nT_0 - t_S \cdot \cos\left(\omega_S n T_0 + \phi\right)\right) \tag{3.19}$$

with the synchrotron frequency ω_s, the oscillation amplitude t_S and the arbitrary phase ϕ. The resulting beam spectrum shows sidebands with the modulation frequency ω_S around the revolution harmonics. The amplitude of the sideband components depends on the oscillation amplitude t_s. Therefore, the beam spectrum is given by

$$J(\omega) = \omega_0 \sum_{k=-\infty}^{k=\infty} \sum_{n=-\infty}^{n=\infty} A_k(\omega) \cdot \delta(\omega - n\omega_0 - k\omega_S). \tag{3.20}$$

Here, the form-factor

$$A_k = (-i)^k \cdot J_k(\omega t_s) \cdot e^{-ik\phi} \tag{3.21}$$

was extracted by using the Bessel function J_k and the relation [36]

$$e^{iz\cos(\alpha)} = \sum_{k=-\infty}^{k=\infty} (i)^k \cdot J_k(z) \cdot e^{ik\alpha} \tag{3.22}$$

together with Poisson's sum rule. In case of small oscillations, Eq. 3.20 can be reduced to the first sidebands resulting in

$$J(\omega) = \sum_{n=-\infty}^{n=\infty} \delta(\omega - n\omega_0) - i\frac{\omega t_s}{2}\delta(\omega - n\omega_0 \pm \omega_s). \tag{3.23}$$

The spectrum is shown in Fig. 11.

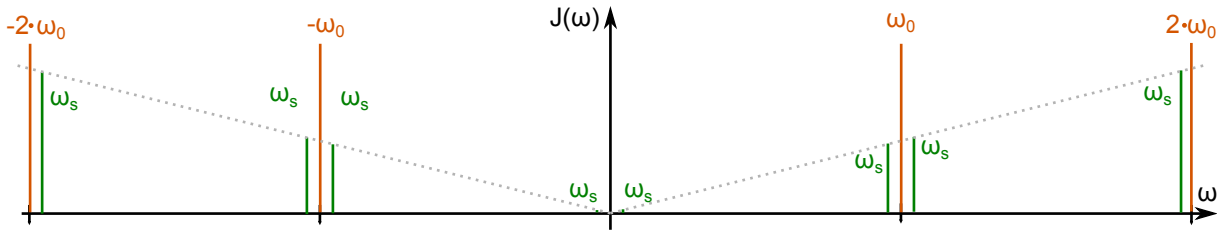

Figure 11: Spectrum of a single bunch which is oscillating longitudinally. The synchrotron sidebands increase linearly with frequency.

At a fill with multiple bunches, the bunches pass the BPM with a smaller time delay $T_{RF} = T_0/h$. While each individual bunch oscillates with the synchrotron frequency, the entire beam oscillates in a multibunch eigenmode or a superposition of multibunch eigenmodes. Since the system has h bunches, there are h eigenmodes of the system. Each mode is characterized by the phase advance between two subsequent oscillators

$$\Delta\phi = \frac{2\pi}{h}\mu. \tag{3.24}$$

In analogy to Eq. 3.19, the beam signal is given by

$$j(t) = \sum_{p=-\infty}^{p=\infty} \delta\left(t - pT_{\mathrm{RF}} - t_S \cdot \cos\left(\omega_S p T_{\mathrm{RF}} + \frac{2\pi\mu}{h}p + \phi\right)\right). \tag{3.25}$$

The phase advance per RF period T_{RF} can be expressed as

$$\frac{\Delta\phi}{\Delta T_{\mathrm{RF}}} = \frac{2\pi\mu}{h} / \frac{T_0}{h} = \mu \cdot \omega_0. \tag{3.26}$$

Therefore, the sideband frequencies in the beam spectrum are shifted by the respective value, which yields for small oscillation amplitudes

$$J(\omega) = \sum_{p=-\infty}^{p=\infty} \delta(\omega - p\omega_{\mathrm{RF}}) - i\frac{\omega t_s}{2}\delta(\omega - p\omega_{\mathrm{RF}} + \mu\omega_0 + \omega_s). \tag{3.27}$$

Only the right sidebands are present, which results in a beam spectrum shown in Fig. 12.

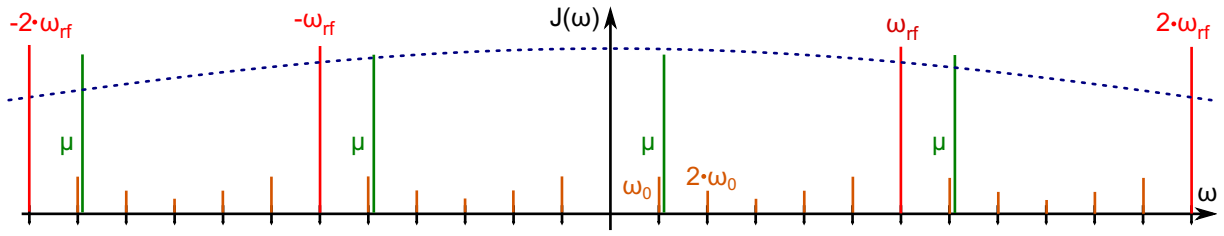

Figure 12: Spectrum of six bunches oscillating in multibunch mode $\mu = 1$, which creates additional sidebands next to the RF harmonics at a distance of $\mu \cdot \omega_0 + \omega_S$. The dashed blue line indicates the suppression of high frequency components due to the finite bunch length.

3.2.3 Transverse Oscillation

A detector to determine the transverse position of the electrons measures the dipole moment of the electrons

$$m(t) = j(t) \cdot x(t) \tag{3.28}$$

with the transverse excursion $x(t)$. In contrast to the longitudinal detector which is not sensitive to the transverse motion, the signal at the transverse detector is influenced by the longitudinal motion due to dispersion, the variation of the arrival time and in case of a non-zero chromaticity by the change of the betatron tune.
The detected momentum for a single bunch is given by [34]

$$m(t) = \left[\underbrace{x_c}_{I} - \underbrace{D_x \frac{\omega_s}{\alpha} t_s \sin(\omega_s t + \phi)}_{II} + \underbrace{A_\beta e^{i\psi_\beta(t)}}_{III} \right] \sum_{n=-\infty}^{n=\infty} \delta\left(t - nT_0 - \underbrace{t_S \cos(\omega_s n T_0 + \phi)}_{IV} \right). \tag{3.29}$$

The first term (I) accounts for a time-independent closed-orbit error x_c, the second term (II) includes the transverse excursion due to dispersion D_x, the third term (III) is the actual betatron oscillation with amplitude A_β and betatron phase ψ_β, which again depends on the longitudinal motion due to chromaticity

$$\psi_\beta(t) = \psi_{\beta,0} + \omega_\beta t + \omega_\xi t_S \cos(\omega_s t + \phi) \tag{3.30}$$

with the chromaticity-dependent frequency $\omega_\xi = \xi\omega_\beta/\alpha$. Finally, the fourth expression (IV) accounts for the different arrival times of the bunch at the detector due to a longitudinal oscillation.

In analogy to the longitudinal motion, the beam spectrum is given by [34]

$$M(\omega) \;=\; \omega_0 A_\beta e^{i\psi_{\beta,0}} \sum_{k=-\infty}^{k=\infty} \sum_{n=-\infty}^{n=\infty} i^k e^{ik\phi} J_k\left(t_s \cdot [\omega_\beta - \omega + \omega_\xi]\right) \delta\left(\omega - [n\omega_0 + \omega_\beta - k\omega_s]\right). \tag{3.31}$$

First of all, the revolution harmonics are accompanied by betatron sidebands. Due to the longitudinal motion, these betatron sidebands are surrounded by synchrotron sidebands, which have different amplitudes due to the chromatic frequency shift ω_ξ (see Fig. 13).

In case of multiple bunches, the formation of a transverse mode μ creates a frequency shift of the betatron sidebands of $\mu\omega_0$ which yields the following position of the spectral lines in the beam spectrum

$$M(\omega) \sim \sum_{p=-\infty}^{p=\infty} \delta\left(\omega - [p\omega_0 + \mu\omega_0 + \omega_\beta - \omega_s]\right). \tag{3.32}$$

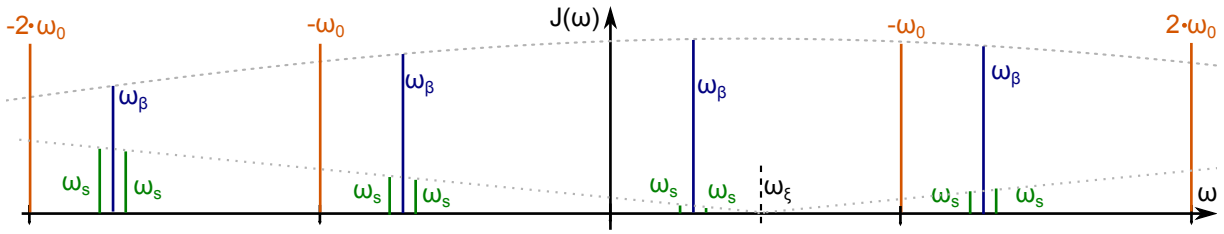

Figure 13: Spectrum of a single bunch oscillating transversely and longitudinally, which creates betatron sidebands surrounded by synchrotron sidebands.

3.3 Coupled-Bunch Instabilities

In case of a coupled-bunch instability, the bunches are coupled to each other by a long-range wake field or narrow-band impedance, respectively. Also single bunch can couple to its own wake field from the previous turn. The corresponding force on that bunch is given by a summation over the wake functions of all previous turns which yields in case of longitudinal oscillation the following equation of motion for turn m [7, 31]

$$\ddot{z}(t) + \omega_s^2 z(t) = \frac{Ne^2\eta}{Lm_0\gamma} \sum_{k=-\infty}^{\infty} W_{\parallel}\left(z(t) - z(t - kT_0) - kC\right) . \tag{3.33}$$

If the wake function decays much slower than the synchrotron period, it can be expanded to the linear order

$$W_{\parallel}\left(z(t) - z(t - kT_0) - kC\right) \approx W_{\parallel}\left(kC\right) + W'_{\parallel}\left(kC\right) \cdot \left[z(t) - z(t - kT_0)\right] . \tag{3.34}$$

The constant term $W_{\parallel}\left(kC\right)$ is not important for the dynamics of the beam but is responsible for a constant phase shift. The second term is proportional to $z(t) - z(t - kT_0) \approx kT_0 dz/dt$, which adds a friction term to the equation, which can either damp the oscillation or give rise to an instability.

By this assumption, Eq. 3.33 is reduced to a linear differential equation, which can be solved by the ansatz

$$z(t) = z_0 \cdot \exp\left(-i\Omega t\right) . \tag{3.35}$$

By inserting the ansatz, an equation for the mode frequency Ω is obtained

$$\Omega^2 - \omega_s^2 = \frac{Ne^2\eta}{Lm_0\gamma} \sum_{k=-\infty}^{\infty} \left[1 - \exp\left(-ik\Omega T_0\right)\right] \cdot W'_{\parallel}\left(kC\right) . \tag{3.36}$$

With the definition of the impedance (Eq. 3.5) and Poisson's sum rule (Eq. 3.15), this yields [7, 31]

$$\Omega^2 - \omega_s^2 = i\frac{Ne^2\eta}{L^2m_0\gamma} \sum_{p=-\infty}^{\infty} p\omega_0 Z_{\parallel}(p\omega_0) - \left[p\omega_0 + \Omega\right] \cdot Z_{\parallel}\left(p\omega_0 + \Omega\right) . \tag{3.37}$$

In the assumption of a small deviation of the mode frequency Ω from the non disturbed synchrotron frequency ω_s, Ω can be replaced by ω_s on the right hand side of Eq. 3.37 and

$$\Omega^2 - \omega_s^2 = (\Omega + \omega_s)(\Omega - \omega_s) \approx 2\omega_s \Delta\Omega, \tag{3.38}$$

which results in

$$\Delta\Omega = i\frac{Ne^2\eta}{L^2 m_0 \gamma 2\omega_s} \cdot \sum_{p=-\infty}^{\infty} p\omega_0 Z_\parallel(p\omega_0) - [p\omega_0 + \omega_s] \cdot Z_\parallel(p\omega_0 + \omega_s). \tag{3.39}$$

In general, $\Delta\Omega$ is a complex number. Its real part corresponds to the perturbed synchrotron frequency, while its imaginary part is responsible for a exponential growth or damping of the electron-bunch motion. The real frequency shift is given by

$$\mathrm{Re}(\Delta\Omega) = \frac{Ne^2\eta}{L^2 m_0 \gamma 2\omega_s} \cdot \sum_{p=-\infty}^{\infty} p\omega_0 \mathrm{Im}\left(Z_\parallel(p\omega_0)\right) - [p\omega_0 + \omega_s] \cdot \mathrm{Im}\left(Z_\parallel(p\omega_0 + \omega_s)\right), \tag{3.40}$$

and the instability growth rate is obtained by

$$\mathrm{Im}(\Delta\Omega) = \frac{1}{\tau} = \frac{Ne^2\eta}{L^2 m_0 \gamma 2\omega_s} \cdot \sum_{p=-\infty}^{\infty} [p\omega_0 + \omega_s] \cdot \mathrm{Re}\left(Z_\parallel(p\omega_0 + \omega_s)\right). \tag{3.41}$$

It is important to notice that the imaginary part of the impedance is responsible for the frequency shift, while the real part causes an increase of the oscillation amplitude.

If h equally spaced bunches are filled to the ring, the equation of motion for one bunch (Eq. 3.33) is extended by the wake fields of all other bunches. Hence, the equation of motion for bunch $n \in [0, h-1]$ is given by [7]

$$\ddot{z}_n(t) + \omega_s^2 z_n(t) = \frac{Ne^2\eta}{Lm_0\gamma} \sum_{k=-\infty}^{\infty} \sum_{m=0}^{h-1} W_\parallel\left(z_n(t) - z(t - kT_0 - \frac{m-n}{h}T_0) - kL - \frac{m-n}{h}L\right). \tag{3.42}$$

In analogy to the previous derivation for one bunch, the equation for multiple bunches results in the complex frequency deviation

$$\Delta\Omega^{(\mu)} = i\frac{hNe^2\eta}{L^2 m_0 \gamma 2\omega_s} \cdot \sum_{p=-\infty}^{\infty} [ph\omega_0 + \mu\omega_0 + \omega_s] \cdot Z_\parallel(ph\omega_0 + \mu\omega_0 + \omega_s), \tag{3.43}$$

which depends on the multibunch mode number μ. Therefore, the respective growth rate for multibunch mode μ is given by

$$\frac{1}{\tau_\mu} = \mathrm{Im}\left(\Delta\Omega^{(\mu)}\right) = \frac{hNe^2\eta}{L^2 m_0 \gamma 2\omega_s} \cdot \sum_{p=-\infty}^{\infty} [ph\omega_0 + \mu\omega_0 + \omega_s] \cdot \mathrm{Re}\left(Z_\parallel(ph\omega_0 + \mu\omega_0 + \omega_s)\right). \tag{3.44}$$

3.4 Head-Tail Instabilities

So far, only the interaction between a complete bunch on other bunches or on a single bunch with itself was discussed. Now, the interaction between particles inside one bunch should be discussed, which can lead to a head-tail instability. The head-tail mode m denotes the number of nodes of the transverse oscillation of the bunch. Since mode zero has no nodes, it corresponds to a transverse rigid-bunch oscillation. Mode one corresponds to a oscillation between the head of the bunch against its tail. In Fig. 14, the first three head-tail modes are shown.

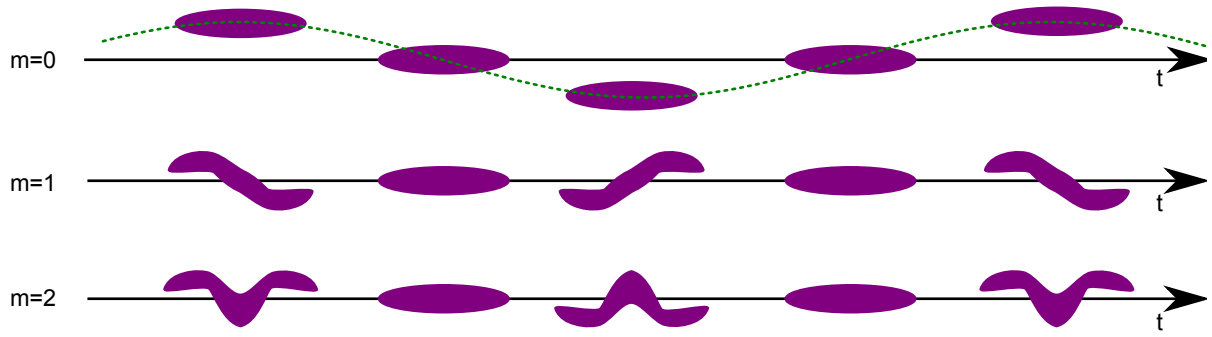

Figure 14: First three head-tail modes for 5 different phases of the oscillation.

For a motivation of the head-tail mechanism, the bunch is modeled as two macro-particles that interact with each other. However, this model can only explain mode zero and one. Both macro-particles perform a longitudinal synchrotron oscillation, which leads to a position change between them after half a synchrotron period. Therefore, both particles interact with the transverse wake field of the other. This results in transverse oscillation of the beam, with can be either stable or unstable depending on the storage ring (see below). The equations of motion for the two macro particles are given by (e.g. [8, 29])

$$\ddot{y}_1(t) + \omega_\beta^2(\delta_E) y_1(t) \quad = \quad 0 \tag{3.45}$$

and

$$\ddot{y}_2(t) + \omega_\beta^2(\delta_E) y_2(t) = \frac{Ne^2}{2\gamma c T_0 m_e} y_1 W_\perp, \tag{3.46}$$

where $W_\perp$ is the mean wake function. After half a synchrotron period the particle interchange their position and the equations are valid with swapped indices. In a machine with non-zero chromaticity, the betatron frequency depends on the energy deviation and therefore, due to the synchrotron oscillation, on the time as well. The explicit time-dependent expression for the betatron frequency is

$$\omega_\beta(\delta_E) = \omega_\beta(0) + \omega_0 \xi \frac{\Delta E}{E} = \omega_\beta(0) + \omega_0 \xi \frac{\omega_S \hat{z}}{c\eta} \cos(\omega_s t), \tag{3.47}$$

which results in the following solution of the equation of motion describing the motion of both macro-particles over one full synchrotron period

$$\begin{pmatrix} \tilde{y}_1 \\ \tilde{y}_2 \end{pmatrix}_{t=T_S} = \exp\left(-i\omega_\beta T_S\right) \begin{pmatrix} 1-\Upsilon^2 & i\Upsilon \\ i\Upsilon & 1 \end{pmatrix} \begin{pmatrix} \tilde{y}_1 \\ \tilde{y}_2 \end{pmatrix}_{t=0} \tag{3.48}$$

with

$$\tilde{y}_1(t) = \left[y_1(0) + i\dot{y}_1(0)/\omega_\beta\right] \exp\left(-i\omega_\beta t\right) \tag{3.49}$$

and

$$\Upsilon = \frac{\pi N e^2 W_\perp}{4\gamma c T_0 m_e \omega_\beta \omega_s} \left(1 + i\frac{4\xi\omega_0\hat{z}}{\pi c\eta}\right). \tag{3.50}$$

The growth per synchrotron oscillation of the two possible modes is given by $\mp\mathrm{Im}\left(\Upsilon\right)$, which corresponds to the following growth rates

$$\frac{1}{\tau_\pm} = \frac{\omega_s}{2\pi} \cdot \mp\mathrm{Im}\left(\Upsilon\right) = \frac{\omega_s}{2\pi} \cdot \mp\frac{N e^2 \xi \omega_0 \hat{z}}{\gamma c^2 T_0 m_e \omega_\beta \omega_s \eta} W_\perp. \tag{3.51}$$

For non-zero chromaticity, one mode has always a positive growth rate, while the other has a negative one. The sum of the growth rates is zero. This sum rule remains true even in bunches with more than two particles, and therefore, more than two head-tail modes. In general, the rigid-bunch mode, in which all particles oscillate in phase, has the largest growth rate and must be suppressed by a slightly positive chromaticity. From a calculation based on a continuous charge distribution, the growth rate of head-tail mode m can be determined, which deviates from the simple two particle model by a mode-dependent correction factor [28]

$$\frac{1}{\tau_m} = \frac{N e^2 \xi \omega_0 \hat{z}}{\gamma c^2 T_0 m_e \omega_\beta \omega_s \eta} \cdot \frac{\omega_s}{4\pi^2 \varepsilon_0} \int_0^\omega \mathrm{Re}Z_\perp(\omega) J_m\left(\frac{\omega\hat{z}}{c}\right) J'_m\left(\frac{\omega\hat{z}}{c}\right) d\omega \tag{3.52}$$

with the Bessel-function J_m. In case of a resistive wall instability, the growth rate can be calculated as [28]

$$\frac{1}{\tau_m} = -\frac{\sqrt{2} C_m}{\pi^{\frac{5}{2}}} \frac{r_0 c}{\sqrt{\mu\sigma_c}} \frac{N_B \xi \sqrt{\hat{z}}}{\eta\gamma b^3 \nu_\beta} \tag{3.53}$$

with the mode-dependent correction factor C_m, which is given by

$$C_m = \left(\int_0^{\frac{\pi}{2}} \sqrt{\sin\left(x\right)} dx\right) \cdot \left(\int_0^\pi \cos\left(m\psi\right) \sqrt{\sin\left(\frac{\psi}{2}\right)} d\psi\right). \tag{3.54}$$

4 Feedback Systems

If only a small number of coupled-bunch modes are excited, a mode-by-mode feedback, suppressing the desired multibunch modes, is sufficient. First implementations of such feedback systems were made in 1977 in the CERN PS booster [37]. However, if the number of unstable modes is large or the modes change due to temperature variations of resonant structures, a mode-by-mode system requires a high complexity and a better choice is a bunch-by-bunch feedback system.

A bunch-by-bunch feedback system detects the position of every bunch over several turns and creates a correction signal, which acts back on the bunch in order to damp any oscillation of the bunch. By damping each bunch individually, every coupled-bunch mode is damped [38, 39]. First bunch-by-bunch feedback systems were installed in the 1990s and operated as completely analog devices (e.g. [40, 41]). Later, due to the availability of fast analog-to-digital converters (ADC) and digital-to-analog converters (DAC), it was possible to use fast digital signal processors (DSP) with their higher flexibility and better adjustability of the phase of the correction signal relative to the input signal (e.g. [42]). More recently, FPGA-based signal processing units are available (e.g. [24]).

In the following, the basic principles and requirements of bunch-by-bunch feedback systems are explained.

4.1 Feedback Control

As shown in previous sections, the motion of a single bunch in a storage ring can be described by a harmonic-oscillator model. With the oscillation coordinate u, which can be either a longitudinal or a transverse coordinate, and the natural damping component α, the equation of motion is given by

$$\ddot{u} + 2D\dot{u} + \omega^2 u = 0. \tag{4.1}$$

The oscillation frequency ω is either given by the longitudinal synchrotron frequency ω_S or by the transverse betatron frequency ω_β. A solution of this equation is a damped harmonic oscillation, given by

$$u(t) = e^{-\frac{t}{t_D}} \sin(\omega t + \phi) \tag{4.2}$$

with the damping time constant $t_D = 1/D$. Neglecting all other effects, D is the natural damping rate, which is given by synchrotron radiation damping.

Large impedance components of the accelerator cause coupled-bunch instabilities (cf. Sect. 3), which add a driving term to the equation of motion

$$\ddot{u} + 2D\dot{u} + \omega^2 u = \frac{F(t)}{m}. \tag{4.3}$$

Although the beam motion of the bunches is coupled, it is sufficient to damp every bunch individually in order to counteract coupled-bunch instabilities.

In a simplified treatment, the external driving force can be interpreted as adding an additional growth rate G in the equation of motion (cf. 3.34)

$$u + 2(D - G)\dot{u} + \omega^2 u = 0. \tag{4.4}$$

If the growth rate of the instability exceeds the damping rate, the oscillation amplitude increases exponentially according to

$$u(t) = e^{-\frac{t}{\tau}} \sin(\omega t + \phi) \tag{4.5}$$

with the total damping rate

$$\frac{1}{\tau} = \frac{1}{\tau_D} - \frac{1}{\tau_G}. \tag{4.6}$$

Since the growth rate of the coupled-bunch instability depends on the beam current, there is a certain current threshold, at which the growth rate will exceed the damping rate. In order to suppress these instabilities above the instability threshold, additional damping mechanisms are needed like an external feedback system.

The feedback system must provide an additional damping constant proportional to the derivative of the beam position in order to increase the total damping rate. This scheme is called resistive feedback.

If the feedback system would directly feed back an output signal proportional to the beam excursion $u(t)$, the damping term would not change, but the oscillation frequency. This is called reactive feedback and does not damp any coupled-bunch instabilities. However, due to the change of the oscillation frequency, it helps to suppress single bunch instabilities, like for example, head-tail instabilities, since they depend on the oscillation frequency.

In the case of a resistive feedback, the equation of motion is given by

$$u + 2(D - G + D_{\mathrm{FB}})\dot{u} + \omega^2 u = 0 \tag{4.7}$$

with the damping rate of the feedback system D_{FB}.

4.2 Feedback Loop

A general diagram of a feedback system damping coupled-bunch instabilities is given in Fig. 15. A deviation from a reference signal is processed by the feedback system with the transfer function $A(\omega)$. The output signal of the feedback system and any external disturbance $F(\omega)$ is the input for the beam transfer function $H(\omega)$. The beam response finally closes the feedback loop creating a new error signal as an input for the feedback controller. The

external disturbance $F(\omega)$ is suppressed by the factor [43]

$$\frac{H(\omega)}{1 + A(\omega)H(\omega)}, \tag{4.8}$$

so that it is beneficial to have a large loop gain $A(\omega)H(\omega)$. However, the feedback gain can not be arbitrary high due to stability .
This general model can be transferred to a real bunch-by-bunch feedback loop. The external disturbances $F(\omega)$ may be coupling from other bunches, injection transients or general orbit fluctuations. The beam transfer function $H(\omega)$ is given by the design of the storage ring, while the feedback transfer function $A(\omega)$ must be designed in a way that all external disturbance is suppressed.

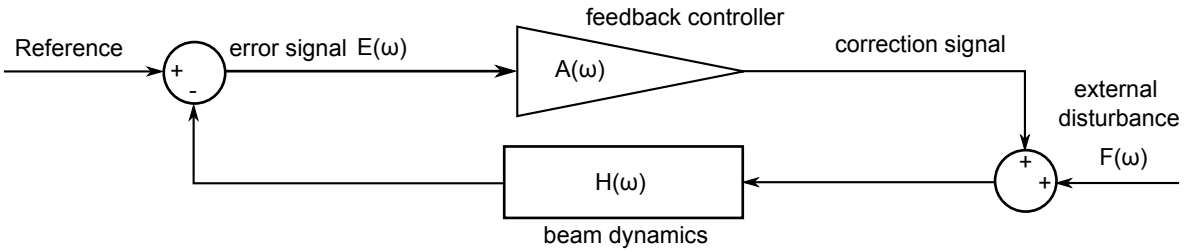

Figure 15: System diagram of a typical feedback loop. The feedback system applies a correction signal to the beam, depending on the displacement of the beam from the reference position. The correction signal and any external disturbance influence the beam dynamics. (following Ref. [43])

In order to create a resistive feedback system, the feedback response must be proportional to the derivative of the beam position signal. In the longitudinal plane, the position is measured relative to a reference phase, while in the transverse plane the displacement from the mean orbit position is used. Therefore, the feedback system must either directly measure the derivative of the beam position to apply a correction signal, or it must continuously measure the beam motion in order to calculate its derivative. Since a typical bunch-by-bunch feedback system measures the bunch position only at one beam-position monitor (BPM) in the ring, a direct measurement of the derivative of the signal is not possible. Therefore, a possible solution is to create a $\pi/2$ phase-shift of the sinusoidal beam-position signal by adding an appropriate delay $\omega \cdot \Delta t = \pi/2$ to the signal. To do so, the oscillation frequency ω of the bunches and the betatron phase advance between BPM and kicker magnet must be known. Alternatively, the derivative can be approximated by two subsequent measurements of the beam position with well known time difference. However, both approaches have a strong drawback. A simple delay line creates an output signal, whenever the input signal is not zero. In case of a static deviation of the beam orbit from the center of the BPM, the feedback system would unnecessarily try to compensate this displacement instead of only compensating for displacements relative to the mean orbit position. Therefore, a so-called

DC rejection must be taken into account when designing the feedback transfer function $A(\omega)$, which makes a simple delay line not suitable for a feedback system.
The simple delay line must be replaced by a digital FIR-filter, which will be explained in the next section. In addition to the desired phase shift of $\pi/2$ at the oscillation frequency, a high loop gain at the oscillation frequency is necessary while simultaneously suppressing all other frequency components.

4.3 FIR-Filter Design

The basic operation principle of digital systems is the same as of analog systems. The analog beam position signal is converted by an ADC and is processed by a signal processing unit which applies an appropriate digital filter to the input data in order to calculate an output signal. The output signal is then converted by a DAC to a voltage which is applied to a kicker structure.
A finite-impulse-response filter (FIR filter) creates an output signal $y[n]$ depending on the last M input samples $x[k]$, which are weighted by a coefficient value b_k [44]

$$y[n] = \sum_{k=0}^{M-1} b_k \cdot x[n-k]. \tag{4.9}$$

The input samples $x[k]$ are also referred to as taps. Thus, the FIR filter can be interpreted as a convolution of the filter coefficient set with the sampled input signal. Although an analog realization of a FIR filter is possible to a certain level, FIR filters are typically implemented digitally. In case of the bunch-by-bunch feedback system, this requires a discrete sampling of the continuous bunch oscillation by a fast ADC with high resolution (at least 12 bit). In Fig. 16, a signal flow diagram of a FIR filter with M taps is shown.

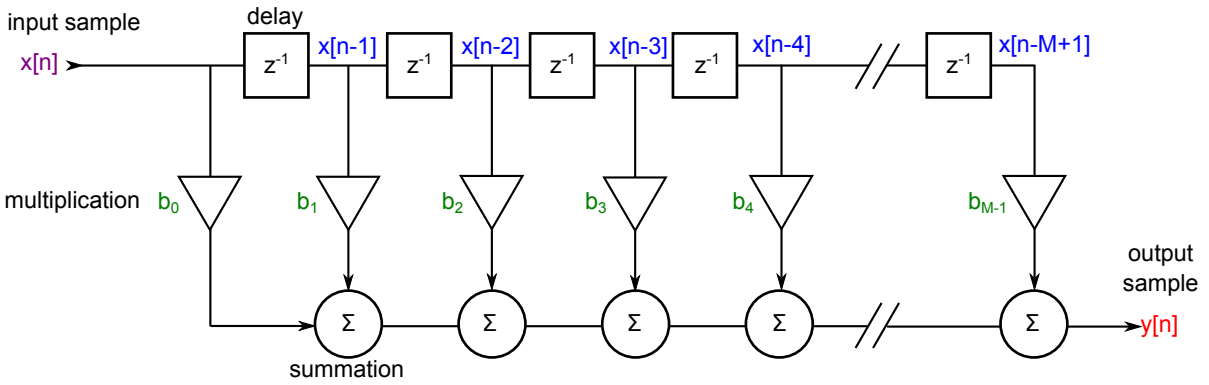

Figure 16: FIR filter with M taps. The output signal $y[n]$ is created by a multiplication of the M previous input samples $x[k]$ with a constant filter coefficient b_k. The z^{-1} blocks correspond to a delay of one sampling period.

Since the output signal of the filter depends only on the last M input signals, the output signal is limited to the sum of the filter coefficients times the largest input signal, which

makes the FIR filter inherently stable. This is a main advantage of an FIR filter over an infinite-impulse-response filter (IIR filter), which depends also on the previous output signals $y[l]$

$$y[n] = \sum_{k=0}^{M-1} c_k x[n-k] + \sum_{l=1}^{N} d_k y[n-l]. \tag{4.10}$$

While a FIR filter creates a limited output for limited input, an IIR filter is not necessarily stable, since it depends on all previous input signals and needs additional feedback to correct for deviations from the desired filter response.

In order to calculate the filter response of a digital filter, the transfer function $A_F(z)$ of the filter must be evaluated for the desired frequency range. The transfer function of filters connects the input signal $X(z)$ of the filter to the output signal $Y(z)$ and is typically defined in z-domain, which is a frequency domain representation of a discrete time signal. Any time discrete sequence is transformed into z-domain by a z-transform given by (e.g. [44])

$$X(z) = \sum_{n=-\infty}^{\infty} x[n] z^{-n}. \tag{4.11}$$

The filter transfer function $A_F(z)$ is defined as the z-transform of the impulse response $h[n]$ of the filter

$$A_F(z) = \sum_{n=-\infty}^{\infty} h[n] z^{-n}. \tag{4.12}$$

In case of a FIR filter, the impulse response $h[n]$ has a finite length and corresponds to the filter coefficients b_k. For given filter coefficients, the magnitude of the frequency response is given by

$$M(\omega) = \left| A_F(e^{i\omega}) \right|, \tag{4.13}$$

while the phase is given by

$$\phi(\omega) = \arg\left(A_F(e^{i\omega}) \right). \tag{4.14}$$

Here, the transfer function $A_F(z)$ was evaluated for $z = e^{i\omega}$.

A typical FIR filter to damp multibunch instabilities is given by the coefficients (e.g.[45])

$$c'_k = \sin\left(2\pi k \cdot \frac{f}{f_0} \cdot D_S + \delta \right) \tag{4.15}$$

with the oscillation frequency of the bunch f and the sampling frequency $f_s = f_0/D_S$. The downsampling factor D_S takes into account that a typical synchrotron oscillation period is much longer than the number of available filter coefficients. Therefore, the feedback system is not taking data at every revolution with frequency f_0, but holds the last sample for D_S turns. The additional phase offset δ allows to create an overall phase shift $\pi/2$ between the correction signal and the input signal.

A filter with coefficients according to Eq. 4.15 shows the maximum gain at the oscillation frequency f but has a non-zero output signal for constant input. In order to suppress any DC output from the filter, it is useful to subtract the overall sum of the filter coefficients, which yields the following corrected coefficients

$$c_k = c'_k - \sum_{m=0}^{M-1} c'_m. \tag{4.16}$$

In Fig. 17, the frequency and phase response of four different coefficient sets are shown. The first two coefficient sets correspond to a full sampling of the oscillation period with and without DC rejection. The second two coefficient sets oversample the oscillation frequency by more than a factor of two, which creates a higher gain at the oscillation frequency but decreases the bandwidth and increases the slope of the phase response.
The frequency and phase response of the FIR filter used at DELTA are shown in Fig. 18. Since the storage ring is operated with varying tunes a small slope and a high bandwidth are desirable in order to operate the feedback system for all machine configurations. Therefore, no oversampling was used . The filter coefficients were calculated according to Eq. 4.15 and Eq. 4.16. In all three planes, the optimum filter phase δ was determined by a calibration measurement. In the longitudinal plane, the downsampling factor D_S was set to seven, while in the transverse planes no downsampling is necessary.

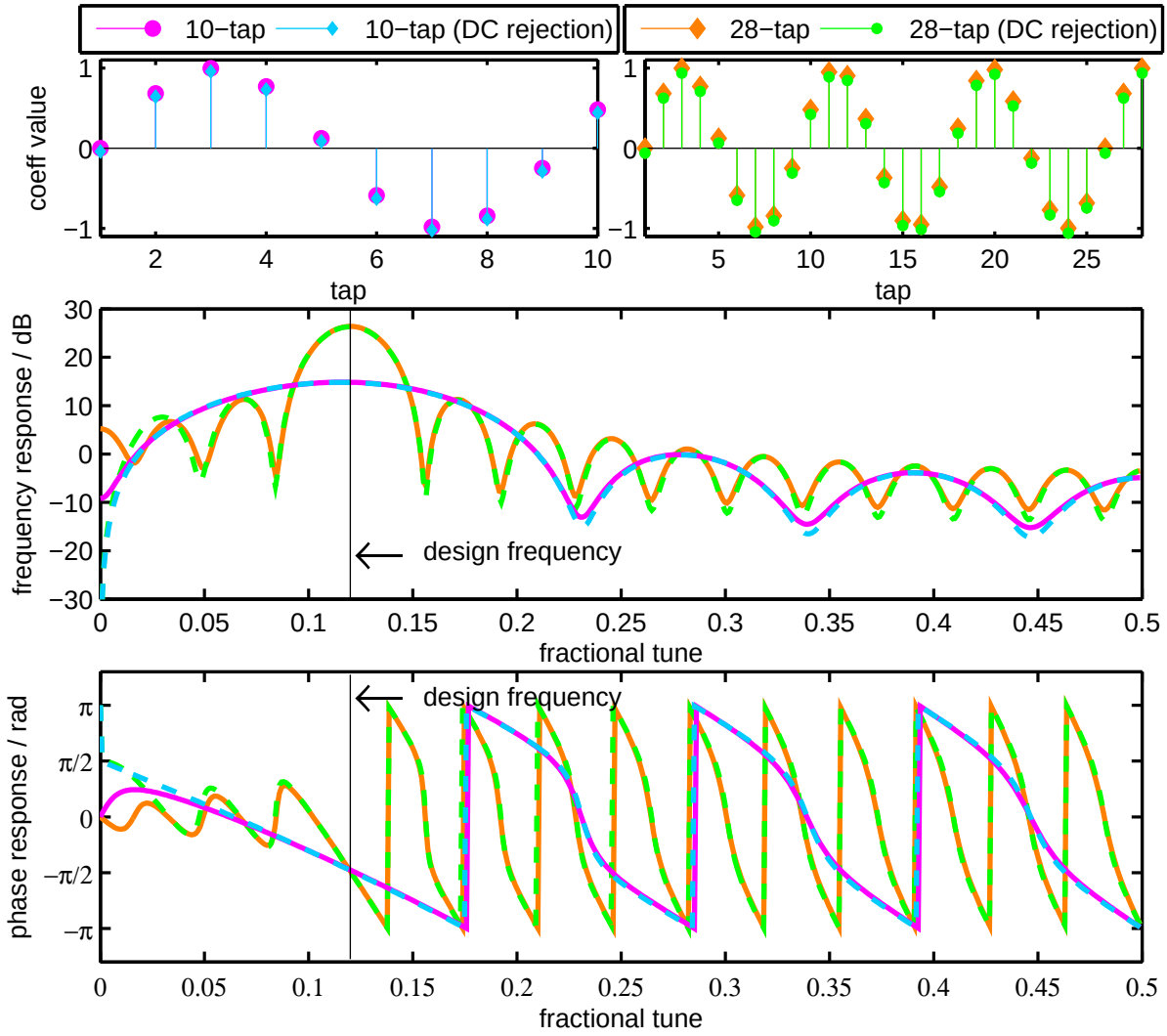

Figure 17: Frequency- (center) and phase- (bottom) response of four different FIR filter coefficient sets (top) for a fixed design frequency of $0.12 \cdot f_0$ with the sampling frequency f_0, which corresponds to the revolution frequency of the electron beam. Shown is a 10-tap filter (magenta) and a 28-tap filter (orange) with filter coefficients according to Eq. 4.15 using $D = 1$ and $\delta = 0$. A second 10-tap filter (blue-dashed) and a second 28-tap filter (green-dashed) is shown with slightly corrected filter coefficients according to Eq. 4.16 in order to reject any DC signal. In this example, the DC rejection is more than 20 dB compared to the initial filter, which can be seen in the frequency response plot (center). The high-frequency response shows only small deviations. The 28-tap filters show a higher gain at the design frequency compared to the 10-tap filters. However, the phase slope is much larger at the design frequency, which can be seen in the phase response plot (bottom).

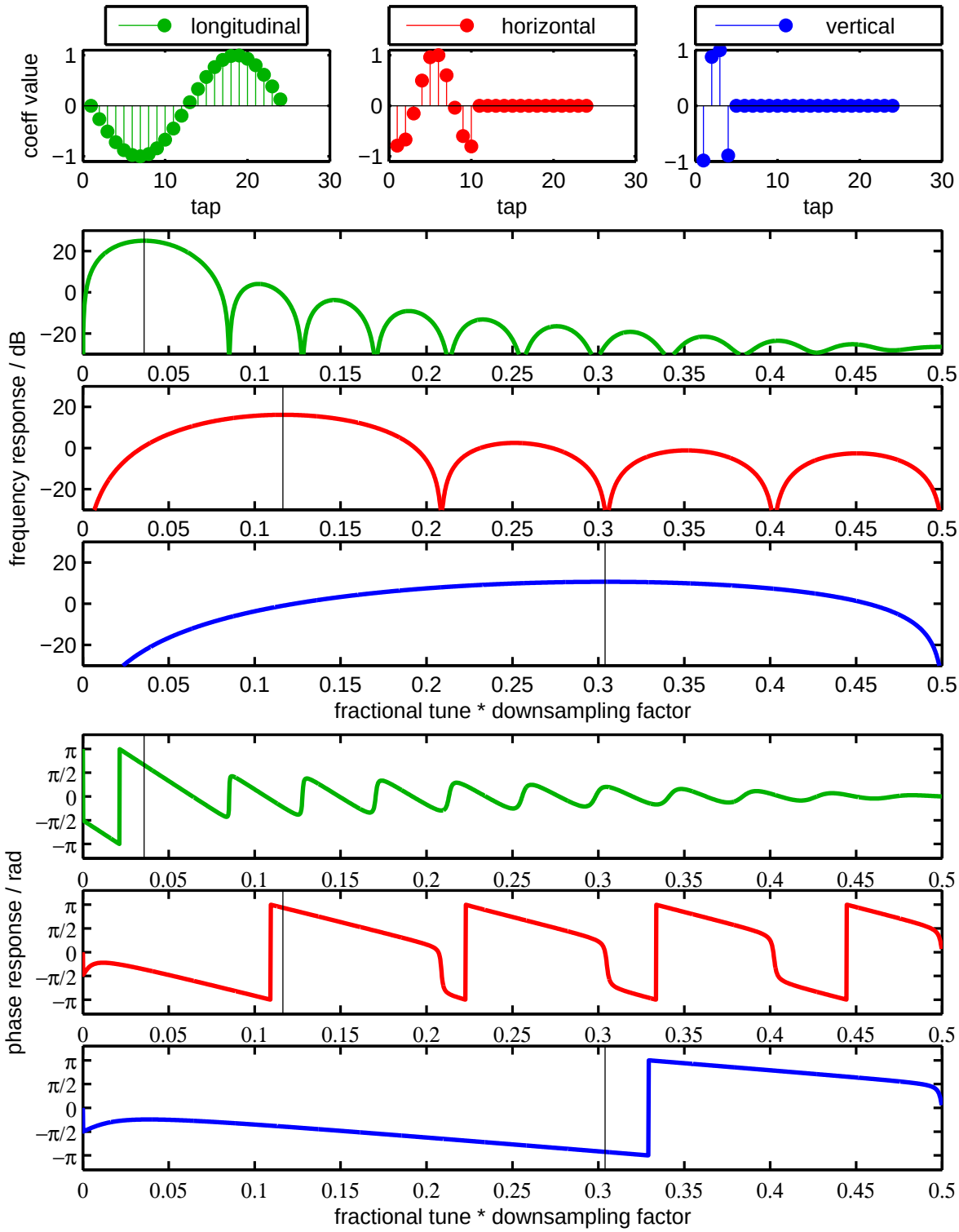

Figure 18: FIR-filter response for the longitudinal (green), horizontal (red) and vertical (blue) bunch-by-bunch feedback system at DELTA. The filters show maximum gain at the fractional tunes indicated by the solid black lines and a large bandwidth. In the case of the longitudinal filter, a downsampling of seven is applied to the input data. All filters show a high DC rejection of more than 30 dB.

5 Simulation of Beam-Cavity Interaction

As discussed in Sect. 3, a bunch passing a resonant structure creates a wake field, which can act back on subsequent bunches. This coupling gives rise to coupled-bunch instabilities, which decrease the brilliance of the radiation or even lead to beam loss. In this section, first of all, the basic relations for the beam-cavity interaction are explained (following [33, 46]). As part of this thesis, a tool was created in MATLAB [47]), which is capable of simulating the beam-cavity interaction. The implementation of the simulation tool (see appendix A.1 for graphical user interface) is based on similar simulations given in [48, 49, 50].

5.1 Basic Principles

5.1.1 Phasor Representation

In order to describe the cavity voltage, it is useful to introduce a phasor

$$\tilde{V}_C = V_C \cdot e^{i\omega t} \tag{5.1}$$

with the amplitude V_C and the time-dependent factor $e^{i\omega t}$. In the following, the phasors are shown in a reference frame, which rotates with the driving frequency ω_{RF} of the generator (i.e. a klystron). The total cavity voltage phasor is given by the superposition of the incoupled generator voltage and the voltage induced by the beam itself when passing the cavity

$$\tilde{V}_C = \tilde{V}_B + \tilde{V}_G. \tag{5.2}$$

The power dissipated in the cavity walls P_C is given by the cavity voltage and the shunt impedance R_S through

$$P_C = \frac{V_C^2}{2 \cdot R_S}. \tag{5.3}$$

5.1.2 Beam loading

The power stored in the beam is

$$P_B = I \cdot V_C \cdot \cos(\phi) \tag{5.4}$$

with the beam current I and the beam phase ϕ.
While the beam is circulating in the storage ring, it induces a voltage $V_{B,0}$ inside the cavity at each passage, which is determined by the loss factor

$$k = \frac{\omega_{\text{res}}}{2} \frac{R_S}{Q} \tag{5.5}$$

with the quality factor Q and the resonant frequency of the cavity ω_{res}. The induced voltage $V_{B,0}$ is given by

$$V_{B,0} = 2k_l q = \omega_{\mathrm{res}} \frac{R_S}{Q} \cdot I_0 \Delta T_b = \frac{2 \cdot I_0 R_S}{1+\beta} \cdot \tau, \tag{5.6}$$

where τ is defined as

$$\tau = \frac{\Delta T_B}{T_F} \tag{5.7}$$

with the cavity filling time

$$T_F = \frac{2Q}{\omega_{res}(1+\beta)}$$

and the bunch period ΔT_B. The coupling coefficient β takes the reflected power from the cavity into account. Since bunches pass the cavity periodically, it induces a voltage in each passage. Due to a deviation (detuning) of the resonant frequency from the RF frequency ω_{RF},which corresponds to the bunch rate, the beam phasor slips in phase after each passage. The phase slippage δ is given by

$$\delta = (\omega_{\mathrm{res}} - \omega_{\mathrm{RF}}) \cdot \Delta T_B = \Delta\omega \cdot \Delta T_B. \tag{5.8}$$

In addition, the beam phasor shrinks by a factor of $e^{-\tau}$, due to the resistivity of the cavity walls. The total voltage induced by the beam is given by a geometric series

$$\tilde{V}_B = -V_{B,0}(1+\exp(i\delta-\tau)+\exp(i2\delta-2\tau)+\exp(i3\delta-3\tau)+\cdots+\cdots) = \frac{-V_{B,0}}{1-e^{-\tau}e^{i\delta}}. \tag{5.9}$$

The build up process of the steady-state beam loading phasor is shown in Fig. 19. For a small bunch spacing period ΔT_B, $|\tau|$ and $|\delta|$ are $\ll 1$ and the previous expression can be approximated by

$$\tilde{V}_B = \frac{-V_{B,0}}{1-(1-\tau+i\cdot\delta)} = \frac{-V_{B,0}}{\tau - i\cdot\delta} = -V_{B,0}\frac{\tau+i\cdot\delta}{\tau^2+\delta^2}. \tag{5.10}$$

This can be expressed in terms of the tuning angle $\psi = \arctan(\delta/\tau)$ as

$$\tilde{V}_B = -V_{B,0}\frac{\tau+i\cdot\delta}{\tau^2+\delta^2} = -\frac{2\cdot I_0\cdot R_S}{1+\beta}\cdot\frac{\tau^2+i\cdot\delta\tau}{\tau^2+\delta^2} = -\frac{2\cdot I_0\cdot R_S}{1+\beta}\cdot\cos(\psi)\, e^{i\psi}. \tag{5.11}$$

The last identity follows using $\sin(\arctan(x)) = x/\sqrt{1+x^2}$ and $\cos(\arctan(x)) = 1/\sqrt{1+x^2}$. With the cavity voltage at resonance ($\psi = 0$) $V_{B,R} = 2I_0R_S/(1+\beta)$, the steady-state limit of the beam-induced voltage is

$$\tilde{V}_B = -V_{B,R}\cdot\cos(\psi)\cdot e^{i\psi}. \tag{5.12}$$

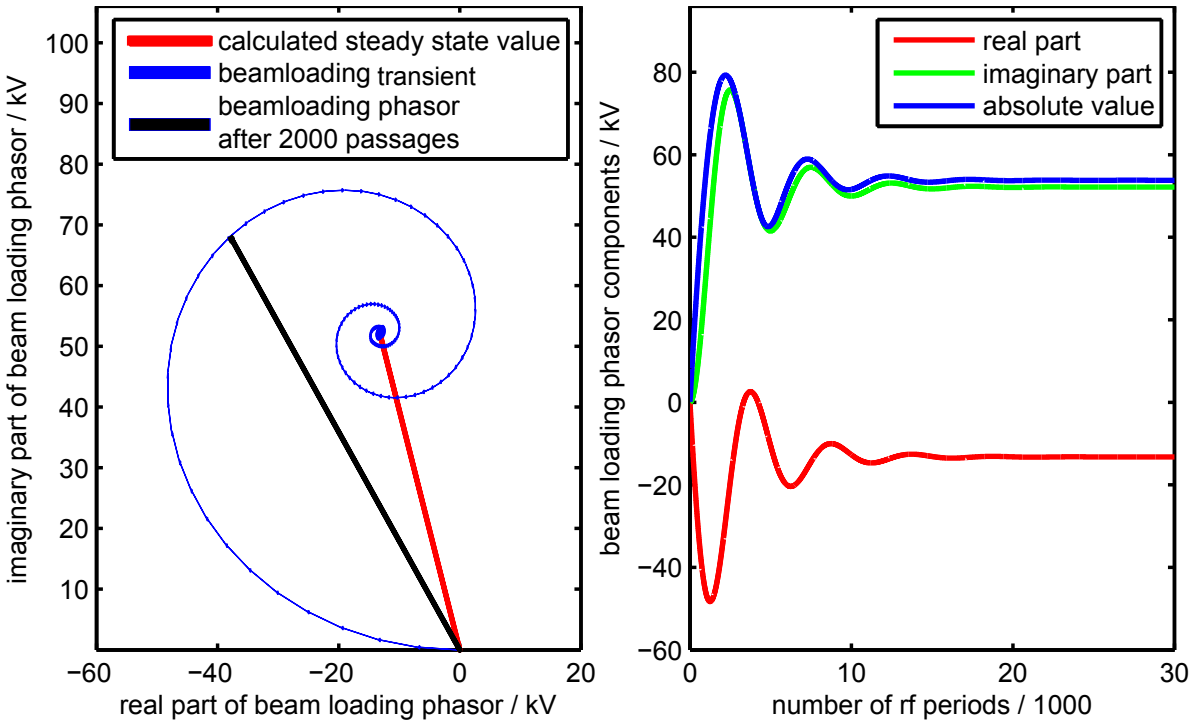

Figure 19: Simulated build-up process of the beam loading phasor. At the beginning of the simulation the beamloading phasor is zero. The blue arrows (left) connect the tip of the beam loading phasor for every 100 passages of the bunch.The black line (left) represents the beamloading phasor after 2000 passage of the bunch. The red line (left) represents the final beam loading phasor which was calculated analytically and matches the end value of the simulated beam loading transient. In addition, the imaginary and real part of the beam loading phasor over time are shown (right). The oscillating behavior of the beam loading phasor depends on the cavity fill time and the resonance frequency of the cavity.

For different detuning frequencies of the cavity, the equilibrium beam loading phasor follows a circle in the complex plane, which is shown in Fig. 20. The maximum beam loading occurs, if the cavity is not detuned from the generator frequency. In order to reduce the necessary generator power to drive the cavity in standard operation, the cavity is slightly detuned from the generator frequency. The optimum detuning will be derived in the next section.In analogy to the voltage induced by the beam, the voltage due to the generator (i.e. the klystron) is given by

$$\tilde{V}_G = V_{G,R} \cdot \cos(\psi) \cdot e^{i\psi} \tag{5.13}$$

with the magnitude at cavity resonance ($\psi = 0$)

$$V_{G,R} = 2 \cdot \frac{\sqrt{\beta}}{1+\beta} \cdot \sqrt{2 \cdot R_S \cdot P_G} \tag{5.14}$$

and the generator power P_G.

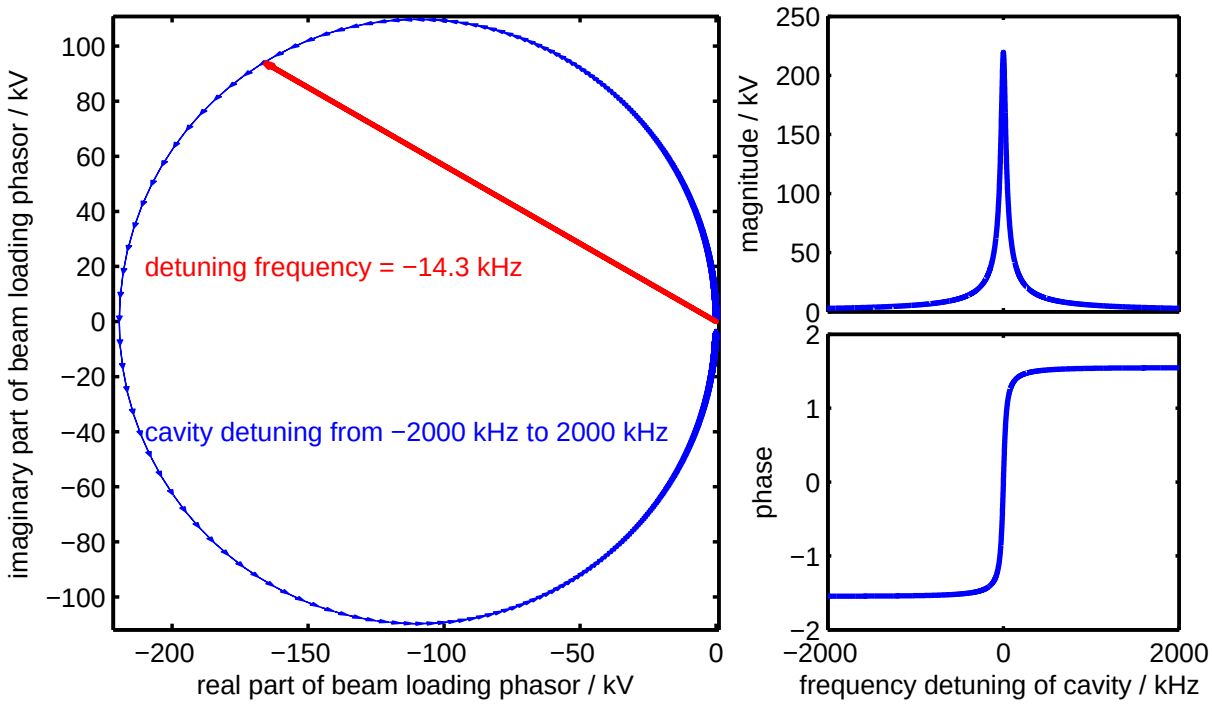

Figure 20: The tips of the equilibrium beam loading phasors for different detuning frequencies form a circle in the complex plane (blue) here shown in steps of 1 kHz. As a reference, a beam loading phasor for a cavity detuning of −14.3 kHz is shown (red). The magnitude of the beam loading phasor (top, right) and its phase (bottom, right) are shown as function of the detuning frequency of the cavity.

To take the phase difference between the generator phasor and the bunch phasor into account, an additional phase θ is added to the voltage phasor of the generator $\tilde{V}_G$, resulting in

$$\tilde{V}_G = V_{G,R} \cdot \cos(\psi) \cdot e^{i(\psi+\theta)}. \tag{5.15}$$

The energy loss due to synchrotron radiation will by compensated by the cavity voltage

$$V_S = \mathrm{Re}\left\{\tilde{V}_C\right\} = V_C \cdot \cos\left(\phi_S\right). \tag{5.16}$$

Since phase focusing is necessary for stable beam operation, the maximum cavity voltage V_C must be larger than V_S, which results to the synchronous phase

$$\phi_S = \cos^{-1}\left(\frac{V_S}{V_C}\right). \tag{5.17}$$

The phasor diagram including the beam loading phasor, the generator phasor and the total cavity phasor is shown in Fig. 21. From Eq. 5.2 directly follows the necessary generator

power for a given cavity tuning ψ and coupling β

$$P_G = \frac{V_C^2}{2R_S} \cdot \frac{(1+\beta)^2}{4\beta} \cdot \frac{1}{\cos^2(\psi)} \left[\left(\cos(\phi) + \frac{2I_0 R_S}{V_C(1+\beta)} \cos^2(\psi) \right)^2 + \right.$$
$$\left. + \left(\sin(\phi) + \frac{2I_0 R}{V_C(1+\beta)} \cos(\psi) \sin(\psi) \right)^2 \right]. \tag{5.18}$$

A derivation of this equation is given in the appendix. The explicit phase difference θ between the generator phasor and the beam loading phasor can be extracted from $\mathrm{Re}\left\{\tilde{V}_C\right\}$ resulting in

$$\theta = \arccos\left(\frac{(V_C \cdot \cos(\phi_S) + V_{B,R} \cdot \cos^2(\psi))}{(V_{G,R} \cdot \cos(\psi))} \right) - \psi. \tag{5.19}$$

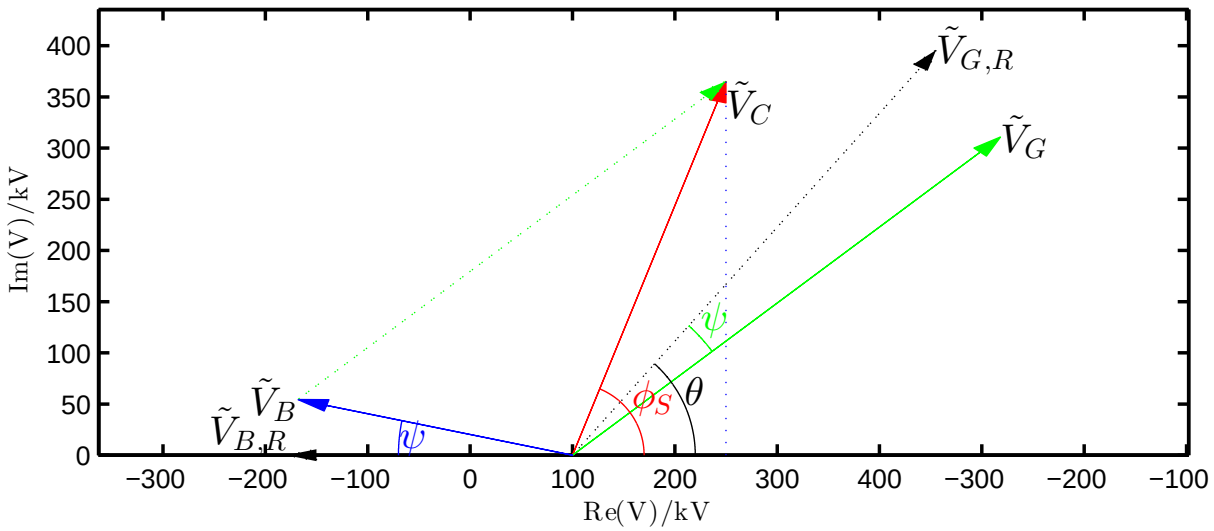

Figure 21: Phasor diagram including the generator voltage $\tilde{V}_G$ (green), the beam-induced voltage $\tilde{V}_B$ (blue), and the net cavity voltage $\tilde{V}_C$. As reference, the generator voltage $\tilde{V}_{\mathrm{G,R}}$ and the beam loading voltage $\tilde{V}_{B,R}$ are shown in black (dashed). In this general case, $\phi_S \neq \theta$.

5.1.3 Optimum Cavity Detuning

The cavity detuning angle ψ depends on the cavity resonance frequency f_{res}, the quality factor of the cavity Q and RF-generator frequency f_{RF} via

$$\tan(\psi) = \frac{\delta}{\tau} = 2 \cdot \frac{Q}{1+\beta} \cdot \frac{\Delta f}{f_{\mathrm{res}}} \tag{5.20}$$

with $\Delta f = f_{\mathrm{RF}} - f_{\mathrm{res}}$. In order to reduce the generator power and reflected power, the cavity has to be tuned accordingly. By calculating the minimum of the generator power P_G (Eq.

5.18) with respect to the tuning angle ψ, the optimum tuning angle ψ_0 is given by

$$\tan\psi_0 = -\frac{V_{B,r}}{V_C}\sin(\phi_S), \tag{5.21}$$

while the minimum generator voltage

$$V_{G,R,0} = V_C + V_{B,R}\cdot\cos(\phi_S) \tag{5.22}$$

and generator power

$$P_{G,0} = \frac{(1+\beta)^2}{4\beta}\cdot\frac{V_{G,R,0}^2}{2R_S} \tag{5.23}$$

follow from Eq. 5.18 for the optimum tuning angle. For a given bunch current, the optimum frequency detuning of the cavity can be derived by comparing Eq. 5.20 and Eq. 5.21

$$\Delta f = -f_{\text{res}}\cdot\frac{I_0\sin\phi}{V_C}\cdot\frac{R_S}{Q} \approx -f_{\text{RF}}\cdot\frac{I_0\sin\phi}{V_C}\cdot\frac{R_S}{Q}. \tag{5.24}$$

The error made by the assumption is of the order of 0.5 Hz.
To verify the above expressions, the calculated generator power (from Eq. 5.18) is plotted for different detuning angles ψ in Fig. 22. In addition, the optimum detuning angle calculated using Eq. 5.21 and the minimum generator power (from Eq. 5.23) is plotted.

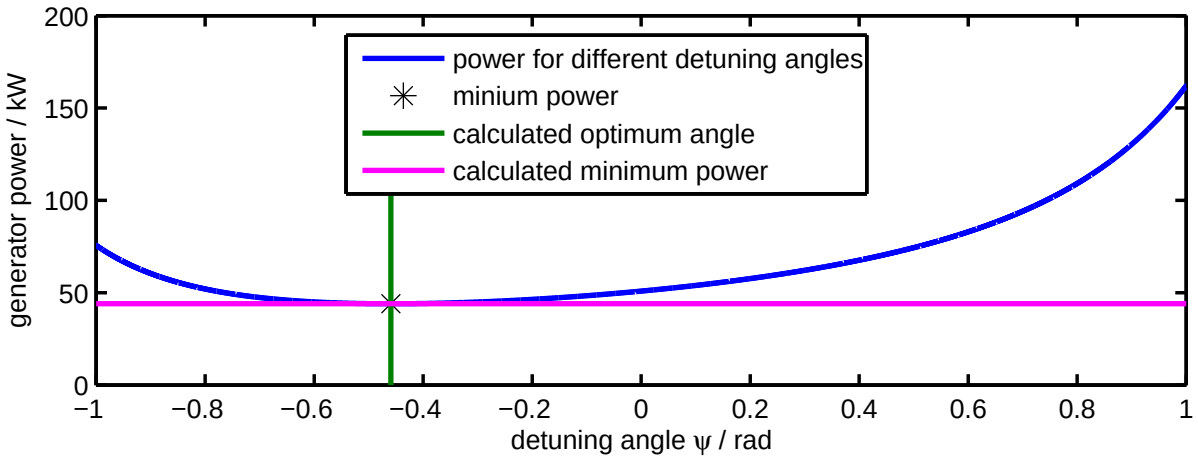

Figure 22: Generator power for different detuning angles according to Eq. 5.18 (blue) and the minimum power of that curve (black star). The calculated optimum detuning angle according to Eq. 5.21 (green) and the calculated minimum power (Eq. 5.23) (magenta) show the same value.

For optimum tuning angle ψ, the phase difference between generator voltage in resonance and the beam loading voltage in resonance is equal to the synchronous phase angle, i.e.

$$\phi_S = \theta. \tag{5.25}$$

In Fig. 23, the phasor diagram for an optimally detuned cavity is shown. Depending on the cavity detuning angle, a different beam loading phase and magnitude is reached. In Fig. 24, a multibunch beam with 100 mA beam current passing a cavity is simulated for an optimum detuning angle of $\approx 30°$ (≈ 14 kHz according to Eq. 5.20). Compared to a larger detuning angle of $\approx 83°$ (≈ 21 kHz), which was previously shown in Fig. 19, the beam loading phasor reaches its equilibrium earlier with no overshooting.For optimum cavity detuning, the optimum coupling coefficient can be calculated by minimizing the generator power with respect to the coupling coefficient β

$$\frac{dP_{G,0}}{d\beta} = 0, \tag{5.26}$$

which results to the following expression of the optimum coupling coefficient:

$$\beta_0 = 1 + \left(\frac{2 \cdot I \cdot R_S \cdot \cos(\phi_S)}{V_C} \right) = 1 + \frac{P_B}{P_C}. \tag{5.27}$$

The coupling coefficient is usually matched for the typical or maximum beam current of the machine and is not changed during decay of the beam current. In contrast to the coupling coefficient β, the cavity tuning angle ψ and the generator voltage $V_{G,R}$ are changed by slow feedback loops, which hold the cavity voltage phasor $\tilde{V}_C$ on a fixed value. The detuning angle was set to the respective optimum value. In Fig. 25, the beam loading power, the generator power, the reflected power and the total power stored in the cavity is plotted versus the beam current. Since the coupling coefficient is optimized for a beam current of 100 mA, the reflected power has a minimum at this value. In Fig. 26, the phasor diagram for different beam currents is shown.

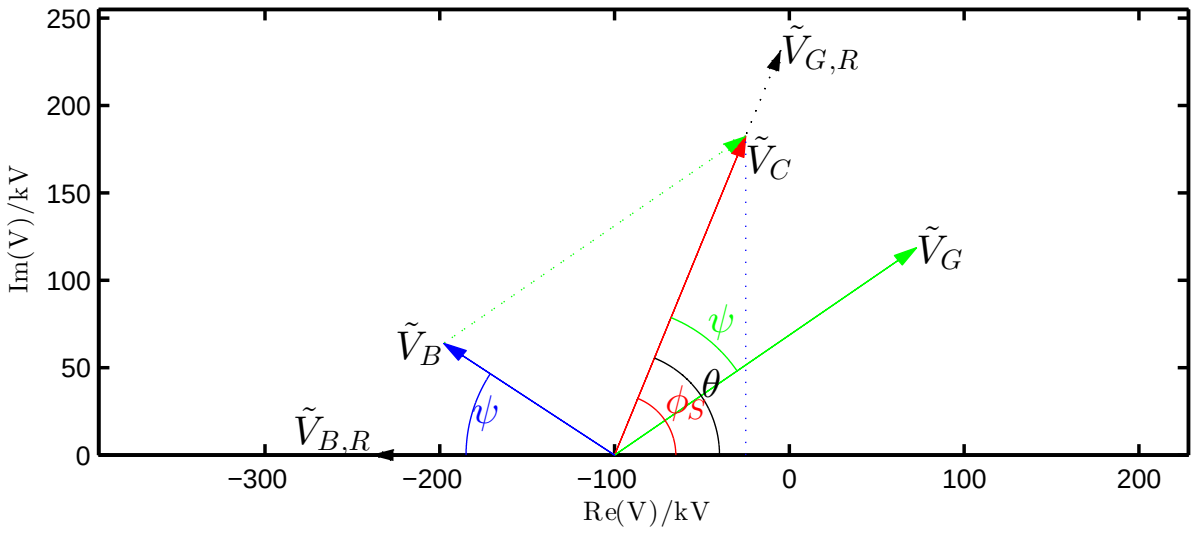

Figure 23: Phasor diagram including the generator voltage $\tilde{V}_G$ (green), the beam-induced voltage $\tilde{V}_B$ (blue), and the net cavity voltage $\tilde{V}_C$. As reference, the generator voltage $\tilde{V}_{\mathrm{G,R}}$ and the beam loading voltage $\tilde{V}_{B,R}$ are shown in black (dashed). Since the cavity is tuned to the optimum value, $\phi_S = \theta$.

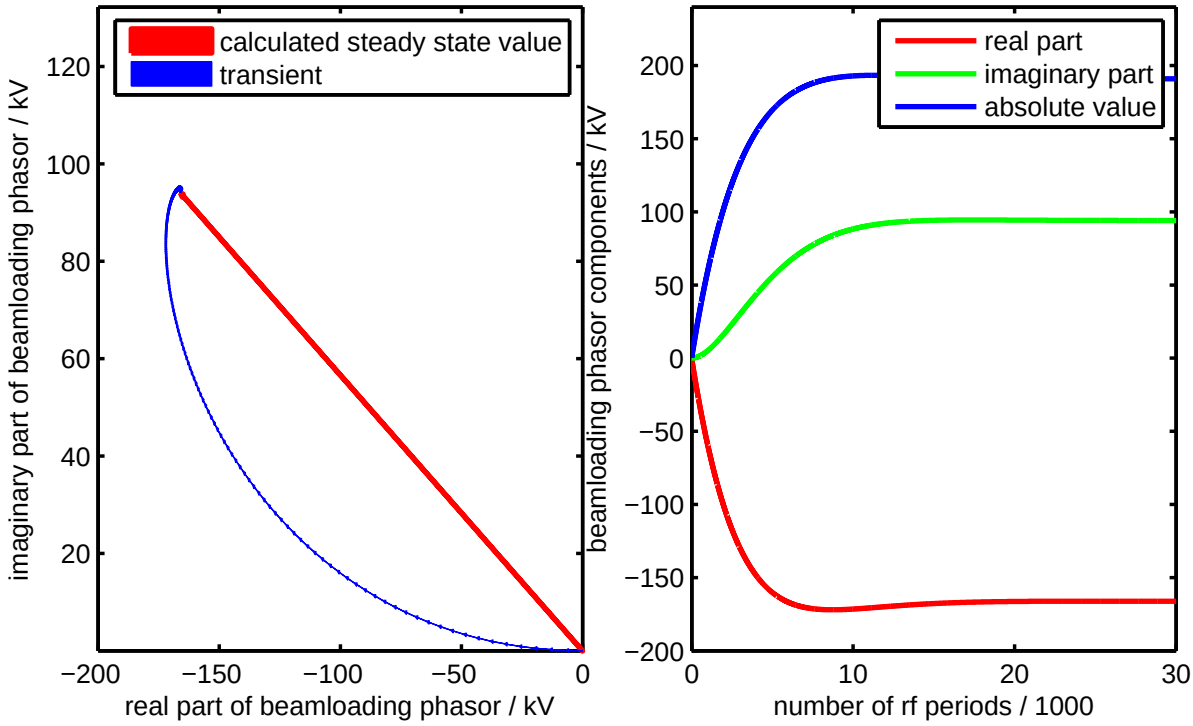

Figure 24: Simulated build-up process of the beam loading phasor for a cavity with optimum detuning. The beamloading phasor is zero at the beginning of the simulation. The blue arrows (left) connect the tip of the beam loading phasor for every 100 passages of the bunch. The red line (left) represents the final beam loading phasor which was calculated analytically and matches the end value of the beam loading transient. In addition, the imaginary and real part of the beam loading phasor over time are shown (right).

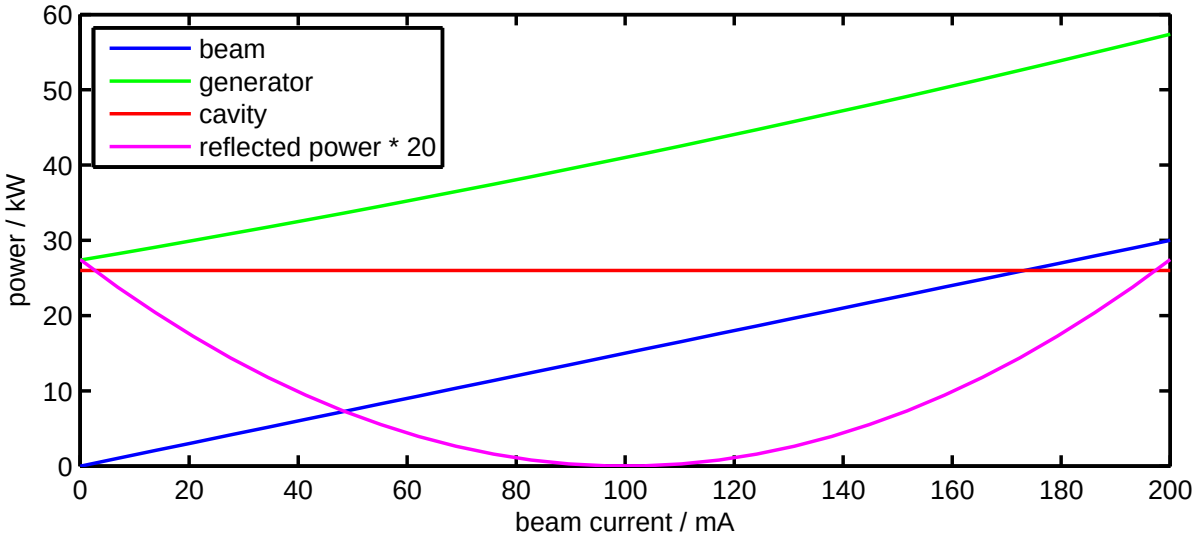

Figure 25: Beam loading power (blue), generator power (green), reflected power (magenta) and the total power stored in the cavity (red) is plotted as a function of the beam current. The reflected power is scaled by a factor of 20. The coupling factor β was optimized for a beam current of 100 mA, which results in the minimum reflected power at that value.

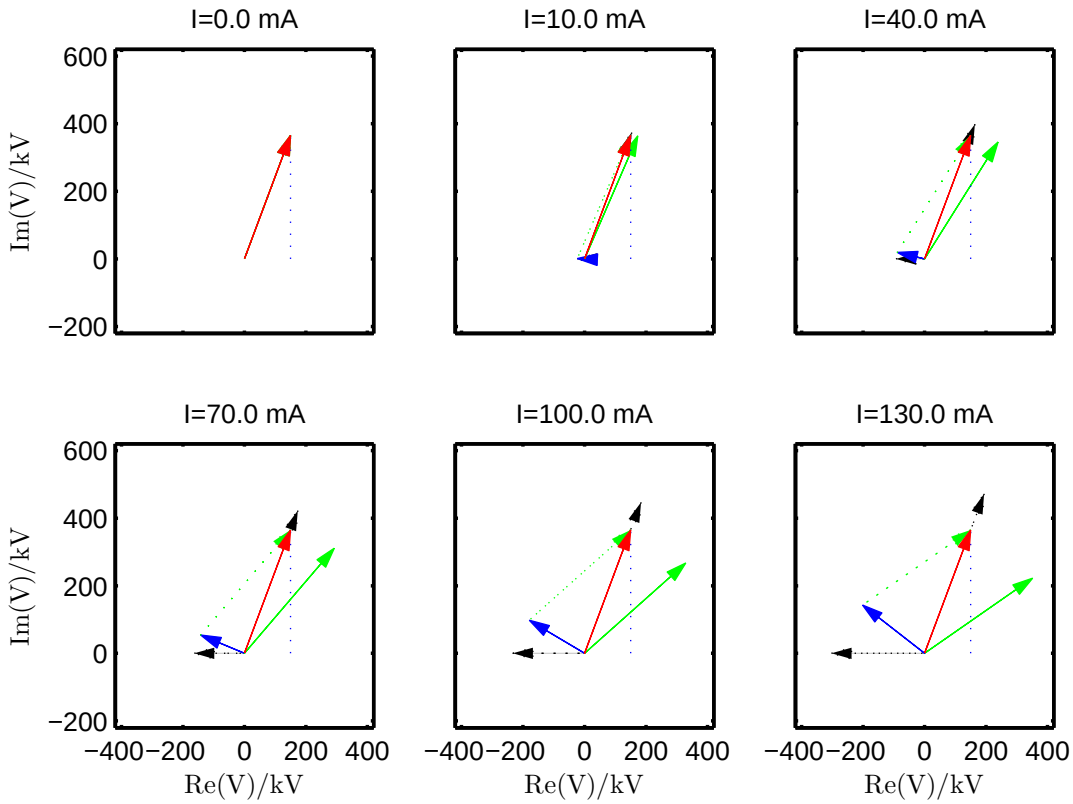

Figure 26: Phasor plots for different beam currents. Since the absolute value of the beam loading phasor (blue) increases with current, the cavity is detuned from resonance with increasing beam current to keep the phase and absolute value of the total cavity voltage (red) constant. In addition, the generator voltage (green) is increased, which can be seen by the increase of the generator voltage at resonance (black, right)

5.2 Implementation

The simulation is based on the principles described in the previous section in which, however, the bunch arrival time was assumed to be equidistant. If this is not the case, for example due to synchrotron oscillation of the bunches, the varying arrival time has to be taken into account. Therefore, the beam loading phasor after each bunch is calculated in analogy to Eq. 5.9 in an iterative procedure

$$\tilde{U}_{B,i+1} = \tilde{V}_B(\phi_i) \cdot \exp\left(\left(i \cdot \Delta\omega - \frac{1}{T_F}\right) \cdot \Delta T_B\right) + \frac{V_{B,0}}{2} \tag{5.28}$$

$$\tilde{V}_B(\phi_i) = \tilde{U}_{B,i+1} + \frac{V_{B,0}}{2} \tag{5.29}$$

with the time between two consecutive bunches

$$T_B = \frac{1}{f_{\mathrm{rf}}}\left(1 + \frac{\Delta\phi}{2\pi}\right), \tag{5.30}$$

the phase difference between these two bunches $\Delta\phi$ and the cavity filling time T_F. For higher-order modes of the cavity analogous formulas are used. The generator voltage, by which the bunches are accelerated, depends on the phase of the electron bunch and can be calculated from the steady-state generator voltage as

$$\tilde{V}_G(\phi_i) = \tilde{V}_G \cdot e^{-i(\theta-\phi_i)}. \tag{5.31}$$

The total cavity voltage at the time, at which the bunches are passing the cavity is finally given by the vector sum of the beam induced voltage and the generator voltage

$$\tilde{V}_C(\phi_i) = \tilde{V}_G(\phi_i) + \tilde{V}_B(\phi_i). \tag{5.32}$$

The longitudinal dynamics of the bunches is calculated in analogy to Eq. 2.19 and Eq. 2.20. Therefore, the energy change of the bunches for each passage of the cavity after a single turn is given by

$$\Delta E = e\mathrm{Re}\left\{\tilde{V}_{C,\mathrm{beam}}(\phi)\right\} - eV_S - 2 \cdot eV_S \cdot \frac{\Delta E}{E} + eV_{FB}, \tag{5.33}$$

while the phase variation after one turn yields

$$\Delta\phi = 2\pi\alpha h\frac{\Delta E}{E}. \tag{5.34}$$

The cavity phasor$\tilde{V}_{C,\mathrm{beam}}(\phi)$ includes the phase focusing of the cavity and all HOMs, while the term $-eV_S - 2 \cdot eV_S \cdot \Delta E/E$ accounts for the radiation losses of the particles due to synchrotron

radiation. Finally, the term eV_{FB} accounts for the voltage applied by the simulated bunch-by-bunch feedback system.
In order to keep the cavity at a minimum generator power level, two slow cavity loops are implemented in the simulation, which keep the synchronous phase of the particles and the average cavity voltage $\left|\tilde{V}_C\right|$ at fixed values. This is achieved by a small variation of the detuning angle and frequency, respectively, and by a change of the generator voltage $V_{G,R}$. The cavity detuning and generator voltage is adjusted after each turn.

5.3 Program Capabilities

In this section, an simulation is shown in order to demonstrate the program capabilities. In addition, the post-processing of the position data is discussed, since the same routines are used later on in Sect. 8 and Sect. 9 to analyze the measured data. The simulation can be divided into the following parts:

1. At the beginning of the simulation, the cavity is not filled by the generator and no beam is circulating in the ring.

2. The generator is switched on in order to fill the cavity. Here, the cavity is already detuned by the optimum detuning angle for a beam current of 60 mA.

3. Then, the entire beam is injected. This creates a transient beam loading of the cavity, due to the previous detuning. The total cavity phasor reaches the desired cavity voltage and phase.

4. Besides the fundamental cavity mode, this simulation includes a higher-order mode influencing the 12th multibunch mode of the beam as an example. Due to this cavity mode and the high beam current, the beam is unstable without external bunch-by-bunch feedback. Therefore, the feedback system is switched on, in order to damp the coupled-bunch instabilities.

5. After the beam is stabilized, the feedback filter coefficients are phase-shifted by 180° for 5000 turns in order to excite the beam by positive feedback. This gives rise to a coupled-bunch instability.

6. Finally, the beam is stabilized again by switching the filter coefficient back.

The results of this simulation are given in the next subsections. The method to temporarily excite the beam by positive feedback is a common technique in order to determine the couple-bunch mode of the beam and will be used in Sect. 8 to study coupled-bunch instabilities at DELTA. The simulation tool is used later on to compare the results of measurements with simulations.

5.3.1 Cavity Filling and Cavity Phasor

In Fig. 27, the phasor diagram of the simulation of the cavity filling process is shown. When the generator is switched on, the total cavity voltage is given by the generator voltage. The transient evolution of the generator phasor is indicated by the green curve. Since the cavity is frequency-detuned to match to a beam current of 60 mA, the cavity voltage does not show the correct angle (depicted by the magenta line in Fig. 27). Then, the beam is injected. Due to the detuning of the cavity, the transient beam loading and the generator voltage sum up to a total cavity voltage with the desired phase angle.

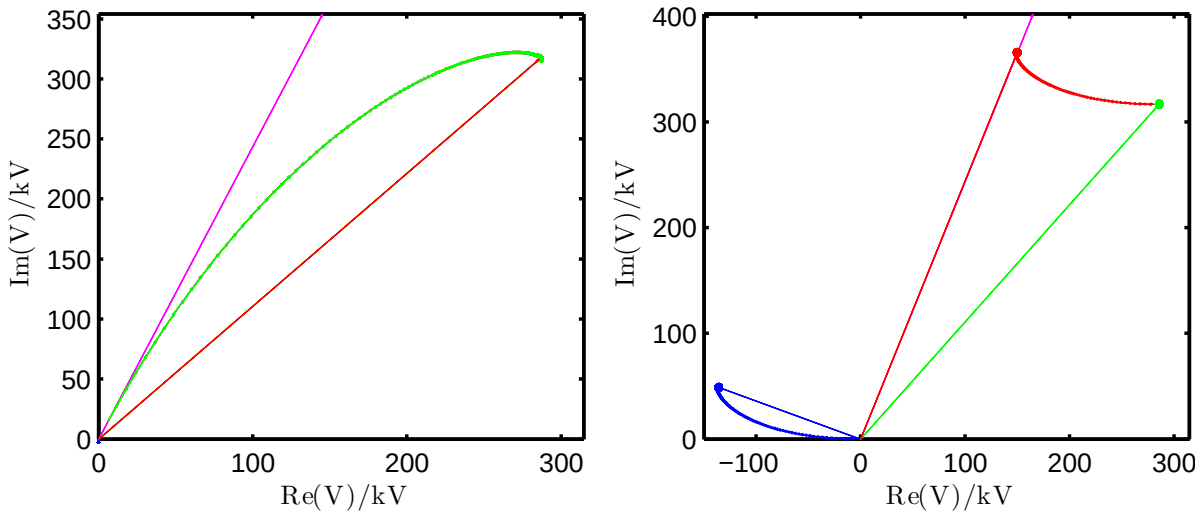

Figure 27: Cavity filling process when switching on the generator (left) and after injection of the beam (right). The beam loading phasor (blue), the generator phasor (green) and the resulting cavity phasor (red) are plotted at the end of the simulation. In addition, the temporal evolution of the respective phasors is depicted by the curves, which represent the tips of the previous beam loading phasors. The optimum phase of the cavity phasor is depicted by the magenta line.

5.3.2 Phase Space Coordinates

In Fig. 28, the phase space coordinates of the simulation are shown. The increase of the oscillation amplitude results from the temporary excitation by the positive feedback. In order to calculate the growth or damping rate of the oscillation amplitude, it is useful to determine the envelope of the bunch signal beforehand. The calculation procedure is given in the next section. However, the envelope is already used in Fig. 28 to define the color-coded oscillation amplitude of all bunches.

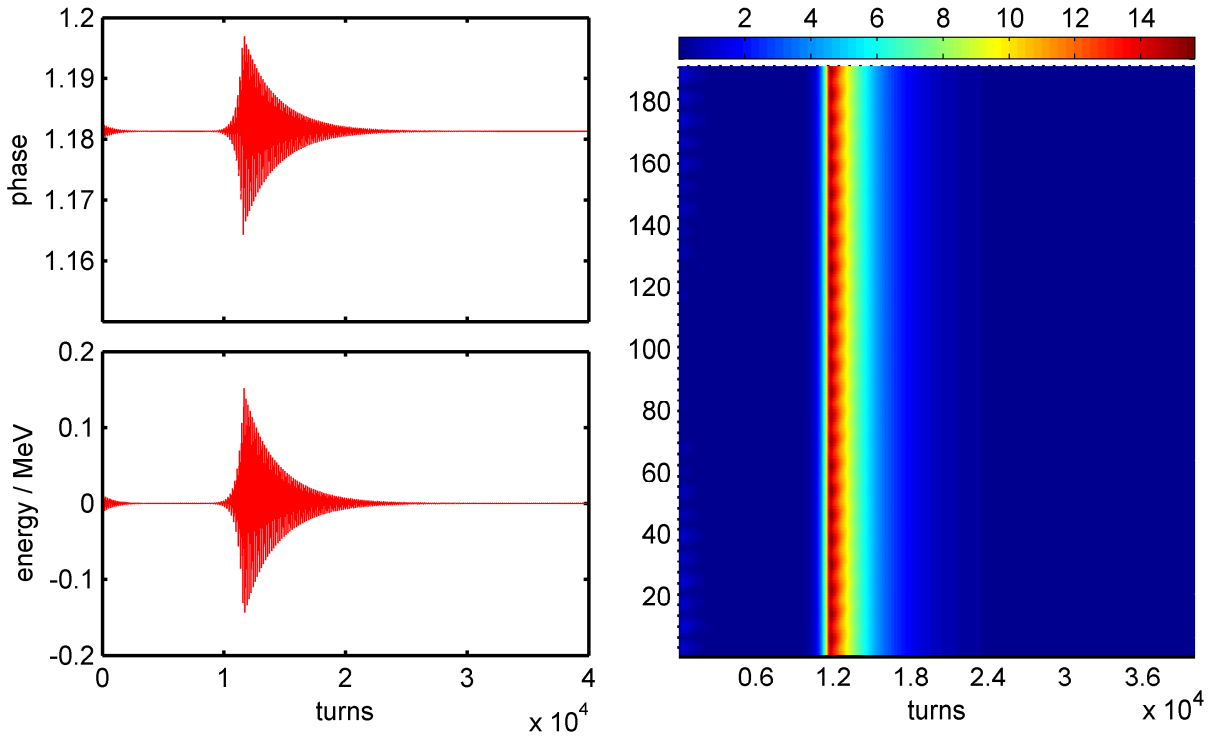

Figure 28: Simulated phase (left,top) and energy (left,bottom) of one bunch as an example for each turn. In addition, the envelope of the phase oscillation of every bunch with color-coded amplitude is shown (right). Since all buckets are filled, the oscillation amplitude of all bunches increases for a short period of time before the oscillation is damped again by negative feedback.

5.3.3 Bunch Envelope

The envelope of the longitudinal oscillation is derived by a Hilbert transform as explained in the following. The Hilbert transform $\mathcal{H}$ of an input signal $x(t)$ is defined as [44]

$$\mathcal{H}\{x(t)\}(t) = \frac{1}{\pi} \int_{-\infty}^{\infty} \frac{x(\tau)}{t-\tau} d\tau, \tag{5.35}$$

which can be expressed in terms of the Fourier transform $\mathcal{F}$ as

$$\mathcal{H}\{x(t)\}(t) = \mathcal{F}^{-1}\left\{(-i \cdot \mathrm{sgn}(f))\, \mathcal{F}\{x(t)\}(f)\right\}(t). \tag{5.36}$$

By definition, the analytical signal $u(t)$ is given by

$$u(t) = x(t) + i\mathcal{H}\{x(t)\}(t). \tag{5.37}$$

In contrast to a Fourier spectrum of a real input signal $x(t)$, the analytical signal consists only of positive frequency components, since

$$\mathcal{F}\{u(t)\}(f) = \begin{cases} 2 \cdot \mathcal{F}\{x(t)\}(f) & \text{for } f > 0 \\ \mathcal{F}\{x(t)\}(f) & \text{for } f = 0 \\ 0 & \text{for } f < 0 \end{cases} \tag{5.38}$$

Due to the definition given in Eq. 5.37, the analytical signal is a complex number, which can be expressed as

$$u(t) = a(t) \cdot e^{i\varphi(t)} \tag{5.39}$$

with the amplitude $a(t)$ and the phase $\varphi(t)$. In case of an input signal $x(t)$ with zero mean value, the amplitude of the analytical signal $a(t)$ corresponds to the envelope of the input signal, which is shown in Fig. 29. Therefore, the mean bunch phase is usually subtracted from the phase oscillation before calculating the envelope in terms of the Hilbert transform.

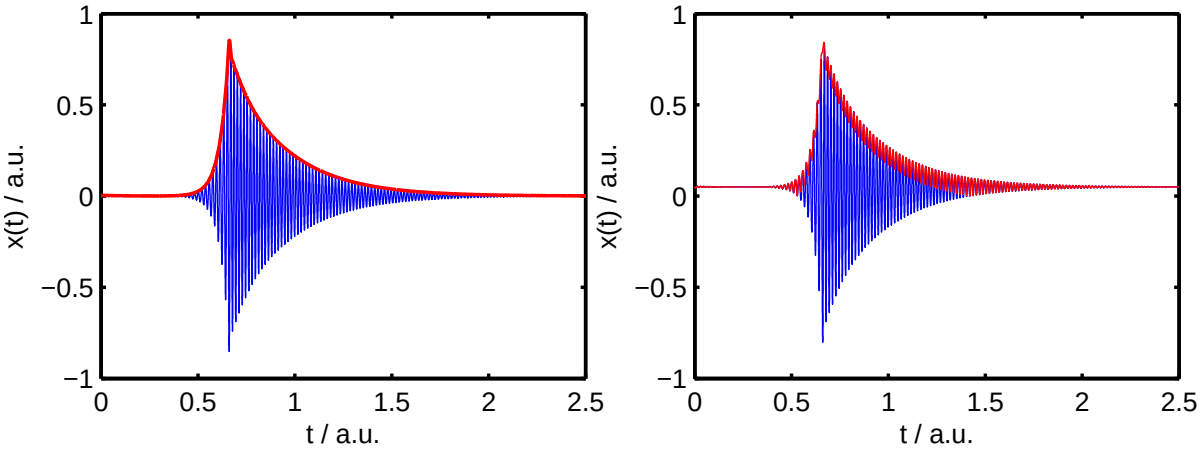

Figure 29: Oscillating signal $x(t)$ (blue) and calculated amplitude of the analytical signal $a(t)$ (red) for a signal with zero (left) and non-zero mean value (right). Only in the case of a zero-mean signal, the calculated amplitude $a(t)$ corresponds to the envelope of the signal.

5.3.4 Beam Spectrum

In addition to the phase space coordinates of all bunches, the frequency spectrum of the beam is calculated via a Fourier transform. In Fig. 30, the bunch spectrum of the entire beam is plotted. Since the beam is sampled only once for each passage of a bunch, the maximum frequency component is given by $f_{\max} = 1/(2 \cdot T_B) \approx 250\,\text{MHz}$. The maximum spectral component at about 31.2 MHz is shown in detail in the inset of the figure. Here, the right synchrotron sideband of the 12th revolution harmonic of the beam is visible, while the revolution harmonic itself is strongly suppressed since the simulation was performed with equal bunch charges. The mode number of the maximum spectral contribution corresponds

to the most unstable mode at the DELTA storage ring, which will be discussed in Sect. (8). However, in this simulation mode 12 is dominant due to the arbitrarily chosen higher-order-mode spectrum at the beginning of the simulation. Furthermore, Fig. 30 shows the summation of all single bunch spectra in the frequency range from zero to 100 kHz. Here, all frequency components are folded into the baseband of the single bunch (0 to $f_{\max} = 1/(2 \cdot T_0) = 1.3\,\mathrm{MHz}$), and the visibility of a large component at the synchrotron frequency of 14.7 kHz denotes the existence of a coupled-bunch oscillation. Although the entire information of the beam motion is already given by the phase space plot and the frequency spectrum, it is often useful to determine the coupled-bunch mode and its temporal evolution during the measurement. Therefore, the evolution of the mode spectrum is calculated as given in the next section.

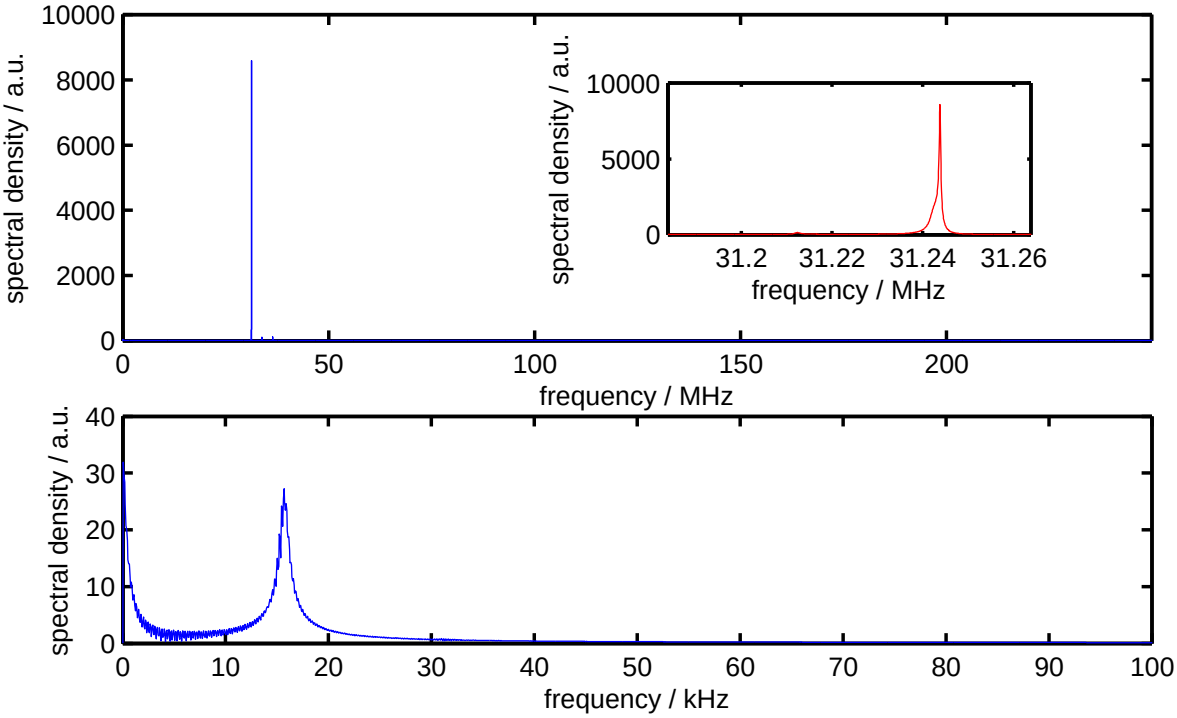

Figure 30: Total beam spectrum (top) calculated from the time series of the grow-damp simulation. The maximum frequency component at approximately 31.2 MHz is shown in the inset. The sum of all single-bunch spectra (bottom) shows the synchrotron sidebands at 14.7 kHz.

5.3.5 Mode Spectrum

The mode spectrum is calculated based on the scheme described in [51, 52, 53]. First, the analytical signal for each bunch is derived by a Hilbert transform as given in Eq. 5.37. If the bunch oscillation coordinate x_n^k of bunch k is given by

$$x_n^k = a_n^k \cdot \cos\left(2\pi n D_S \nu + \phi_n^k\right) \tag{5.40}$$

with the tune ν, the downsampling factor D_S, the amplitude a_n^k and the phase ϕ_n^k, the analytical signal can be expressed as

$$u_n^k = a_n^k e^{i\left(2\pi n D_S \nu + \phi_n^k\right)}. \tag{5.41}$$

By calculating the discrete Fourier transform of the sequence of the analytical signals of all bunches for one turn, the amplitudes of all eigenmodes of the bunch train are derived. This corresponds to a projection of the beam motion on the even-fill eigenmode (EFEM) basis. The analytical signal of the modal phase space coordinate U_n^m of the m-th EFEM at turn n is therefore given by [51, 52]

$$U_n^m = A_n^m e^{i(2\pi n D_S \nu + \Phi_n^m)} = \sum_{k=0}^{N-1} u_n^k e^{-i\frac{2\pi m k}{N}}. \tag{5.42}$$

The envelope plot of the mode amplitudes is derived by taking the absolute value of U_n^m. If not all buckets are filled with the same charge, the beam has eigenmodes that are a linear combination of EFEMs. In addition to the projection of the eigenmode basis, a bandpass filter is used in the calculation, which is centered either at the synchrotron or betatron sidebands. A plot of the modal amplitudes of the simulation is given in Fig. 31. It shows that only mode 12 is temporary excited by the feedback system.

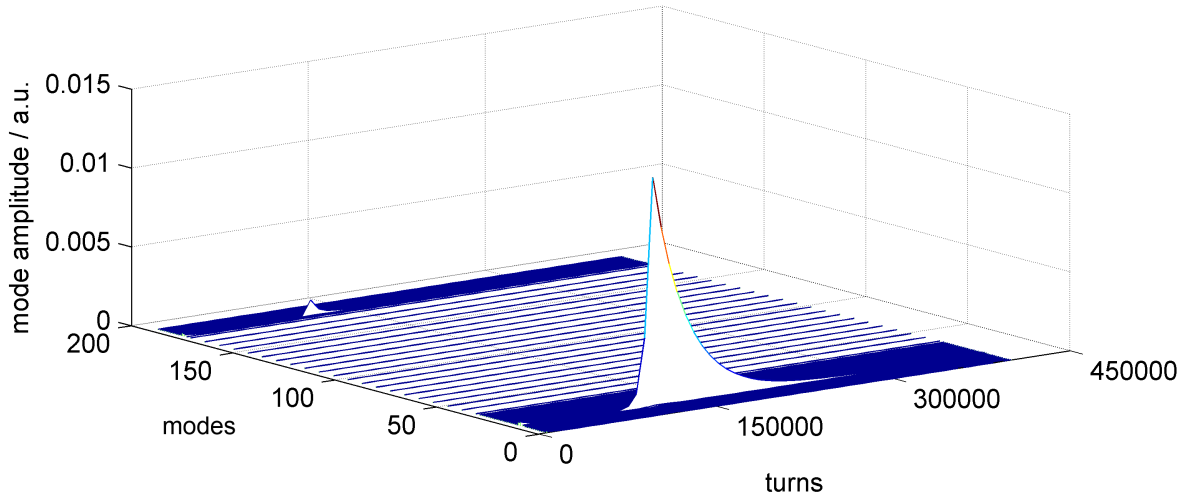

Figure 31: Calculated mode amplitude of the bunch train for all modes as a function of turns.

6 The DELTA Synchrotron Light Source

In this section, the basic parameters of the DELTA electron storage ring in general and an overview of the short-pulse facility is given.

6.1 The Electron Storage Ring DELTA

The 1.5-GeV electron storage DELTA is operated by the Center for Synchrotron Radiation [11] of the TU Dortmund University as a synchrotron radiation source and for research in accelerator physics (Fig. 32). The first beam was injected into the storage ring in 1996 [12]. Since 2000, the facility is in continuous operation [13].

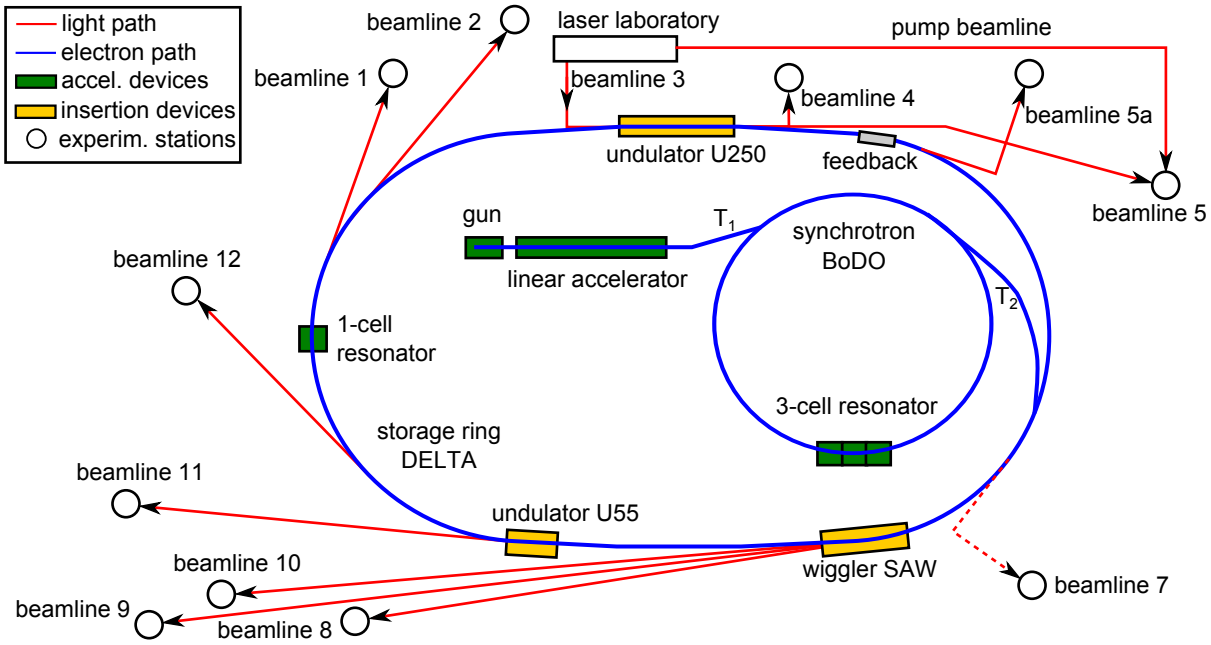

Figure 32: Sketch of the synchrotron radiation facility DELTA.

A thermionic electron source (gun) emits electrons that are accelerated by a linear accelerator to energies up to 70 MeV. These electrons are injected through the first transfer channel T1 into the booster synchrotron BoDo, which accelerates the electrons to 1.5 GeV. This allows a full-energy injection through the second transfer channel T2 into the electron storage ring. The storage ring has a circumference of 115.2 m, which corresponds to a revolution frequency of 2.6 MHz. At present, beam currents of up to 130 mA in multibunch mode and 20 mA in single-bunch mode are stored. The beam lifetime is about 12 hours (at 100 mA) in multibunch operation and a few hours (at 10 mA) in single-bunch operation. Several beamlines provide synchrotron radiation to the experimental stations. The superconducting wiggler SAW generates hard X-ray radiation for beamlines 8, 9 and 10 (photon energies in the range from 4.2 keV to 7.9 keV) [54]. The permanent-magnet undulator U55 generates X-ray radiation for beamline 11 (photon energies in the range from 55 eV to 1.5 keV). At

beamlines 1, 2 and 12 bending magnets generate X-ray radiation with a critical photon energy of 2.3 keV. The electromagnetic undulator U250 provides soft X-ray and VUV radiation for beamline 5 (photon energies in the range from 5 eV to 400 eV). In addition, the U250 is used as an optical klystron for the creation of ultrashort radiation pulses in the context of the short-pulse facility at DELTA. Beamline 7 is used as a synchrotron light monitor.
Table 1 summarizes the basic parameters of the storage ring.

Table 1: Basic parameters of the storage ring [55].

parameter	symbol	value
beam energy	E	1.5 GeV
maximum beam current (multibunch)	I_{B}	130 mA
maximum beam current (single bunch)	I_{B}	20 mA
circumference	L	115.2 m
revolution frequency	f_0	2.6 MHz
RF frequency	f_{RF}	500 MHz
nominal RF power	P_{RF}	26 kW
momentum compaction factor	α	0.0049
bunch length (FWHM)	τ_e	100 ps
horizontal emittance	ε_x	$17 \cdot \mathrm{nm} \cdot \mathrm{rad}$
energy acceptance	$\Delta E_{\mathrm{max}}/E$	1%
synchrotron frequency	f_{sync}	15.7 kHz
fractional horizontal tune	ν_x	~ 0.10
fractional vertical tune	ν_y	~ 0.28

6.2 The Short-Pulse Facility

The short-pulse facility at DELTA includes beamlines 3, 4, the THz beamline 5a and the beamline 5 in the northern part of the DELTA storage ring. The facility is in operation since 2011 [56]. It uses the Coherent Harmonic Generation (CHG) principle [57, 58, 59] in order to create coherent and ultrashort radiation pulses in the VUV regime. An overview of the short-pulse facility is given in Fig. 33.

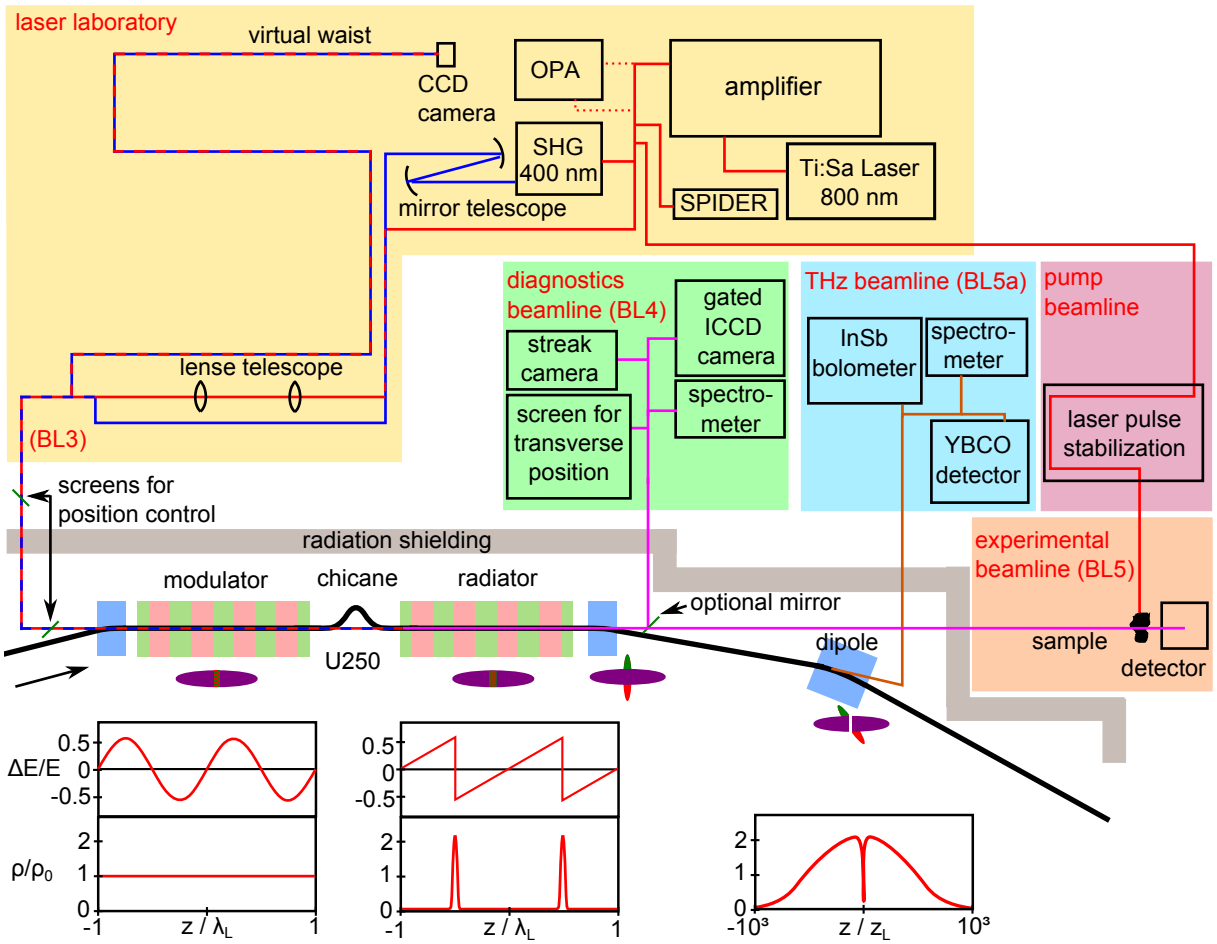

Figure 33: Sketch of the DELTA short-pulse facility. The lower plots show the energy modulation $\Delta E/E$ and electron density ρ as a function of the longitudinal coordinate z. In the undulator, the relevant longitudinal scale is the laser wavelength λ_L, while in the bending magnet the dip in the electron density is of the order of the laser pulse length z_L. The bending magnets (blue) allow to separate the electron path from the radiation.

To obtain the CHG pulses, ultrashort laser pulses of typically 40 fs full-width at half maximum (FWHM) are focused into the first part of the undulator U250 (modulator) via beamline 3 [60]. Here, the laser pulses interact with the electron bunches leading to a modulation of the electron energy due to the laser field. Since the electron bunches are 2000 times longer than the laser pulses, only a small fraction of the electrons at the center of the bunches is energy-modulated. Next, the electron bunches pass a magnetic chicane, which creates a den-

sity modulation inside the electron bunches due to the different path lengths of the off-energy electrons. The density modulation is also referred to as "micro-bunching" (see phase-space plots in Fig. 33). In the last part of the undulator (radiator) the density-modulated electrons emit coherent radiation at the laser wavelength and harmonics thereof. The intensity of the CHG radiation is given by

$$I_{\mathrm{CHG}} = b_n^2 \left(\frac{\tau_L}{\tau_e} \right)^2 N_e^2 I_e$$

with the bunch length τ_e, the laser pulse length τ_L, the number of electrons in the bunch N_e, the intensity emitted by a single electron I_e and the so-called bunching factor b_n. The bunching factor is a measure of the degree of micro-bunching and has a value between zero and one.

The short laser pulse is generated in a titanium-sapphire laser in mode-locked operation. Next, the laser pulse is amplified in a regenerative amplifier to a pulse energy of 8 mJ [61]. The pulse duration can be measured in a SPIDER and has a typically full width at half maximum (FWHM) of 40 fs. In addition, a second-harmonic-generation unit (SHG) allows to double the frequency of the laser pulse to reach a wavelength of 400 nm. The laser pulse is focused to the center of the modulator by using either a mirror telescope at at a wavelength of 400 nm or a lens telescope at 800 nm.
Remote-controllable screens and cameras allow to guide the laser pulse to the undulator. Behind the telescopes, it is possible to reflect the beam back to the laser laboratory so that its waist can be measured in the same distance as the modulator is away from the telescopes. A CCD camera allows to determine the beam profile and the divergence of the beam .
In order to establish the temporal and spatial overlap of the laser pulse and the electron beam in the modulator, the laser pulse and the undulator radiation created by the electron bunch is guided through the diagnostics beamline (BL4). For the temporal overlap, a streak camera (see Sect. 7.2) and a fast avalanche photodiode are used to compare the arrival times of the two light pulses. By a remote-controllable phase shifter, the laser pulse is delayed to achieve the temporal overlap.
The spatial overlap is obtained by comparing the positions of the undulator radiation and the laser pulse on screens. Remote-controllable mirrors are in used to change the laser path inside the undulator. A first indication for a successful overlap between the laser pulse and the electron bunch in the undulator is the emission of coherent THz radiation in a subsequent dipole magnet. Coherent THz radiation is emitted, since the energy-modulated electrons propagate out of the center of the bunch creating a dip in the electron density. To detect this THz radiation, a dedicated beamline was built in 2011 [62]. Here, an InSb bolometer is used for the detection of laser-induced THz radiation. In addition, an in-vacuum spectrometer and a fast YBCO detector are available to perform dedicated THz measurements [63].
Once the overlap is achieved, the CHG radiation can be analyzed in the diagnostics beamline

or is sent to the experimental beamline (BL5). The diagnostics beamline is, among other instruments, equipped with a Czerny-Turner spectrometer and a fast gated ICCD camera [64].
With a seeding wavelength of 400 nm, the fifth harmonic (80nm) was observed so far, while with a seeding wavelength of 800 nm the seventh harmonic (114 nm) was reached [65].
The main goal of the short-pulse facility is to perform pump-probe experiments at the experimental beamline (BL5). Therefore, a small fraction of the laser pulse is coupled out in the laser laboratory and guided directly to the experimental beamline in order to excite ("pump") a sample under investigation [66]. By changing the delay between the pump pulse and the CHG probe pulse, the dynamics of the sample excitation can be analyzed with sub-picosecond resolution.
An overview of the main parameters of the short-pulse facility is given in Tab. 2.

Table 2: Basic parameters of the short-pulse facility [66].

parameter	symbol	value
laser		
wavelength (first harmonic)	λ	796 nm
wavelength (second harmonic)	λ	398 nm
max. pulse energy (first harmonic)	E_L	8 mJ
max. pulse energy (second harmonic)	E_L	2.6 mJ
repetition rate	f_L	1 kHz
pulse length (FWHM)	τ_L	40 fs – 70 fs
undulator		
period length	λ_U	250 mm
number of periods (modulator / chicane / radiator)	N_u	7/2/7
max. undulator parameter	$K_{\max}$	10.5
max. r_{56} of chicane	r_{56}	130 μm
max. magnetic field of U250	$B_{\max}$	0.45 T
undulator gap	g	50 mm

Since the intensity and stability of the CHG radiation depends on the temporal and spatial overlap of the laser pulse and the electron beam, any oscillation of the electron bunch decreases the signal quality. To improve the CHG radiation and to investigate and suppress coupled-bunch instabilities at DELTA, a bunch-by-bunch feedback system was installed and commissioned as part of this thesis.

7 Experimental Setup

In this section, the setup of the the bunch-by-bunch feedback system is explained in detail. In addition, the streak camera, which was used to cross-check beam dynamics measurements performed with the feedback system, is described.

7.1 The Digital Bunch-by-Bunch Feedback System

In order to study beam dynamics and different instability mechanisms, the position of every bunch is measured over several thousand turns in the storage ring. By digitizing this data with the digital bunch-by-bunch feedback system, the bunch position is available for post processing. Applying digital filters to the input signal allows to feed back a correction signal to the beam in order to either damp bunch oscillations (negative feedback) or excite them (positive feedback). Furthermore, a numerically controlled oscillator (NCO), integrated in the signal processor, allows to create an RF signal with fixed frequency and phase which can be either applied in addition in closed-loop operation or separately in open-loop operation. To close the feedback loop, the output signal of the feedback units is sent to the corresponding kicker structure. Figure 34 gives an overview of the setup. Detailed information on the required components is given in the following sections.

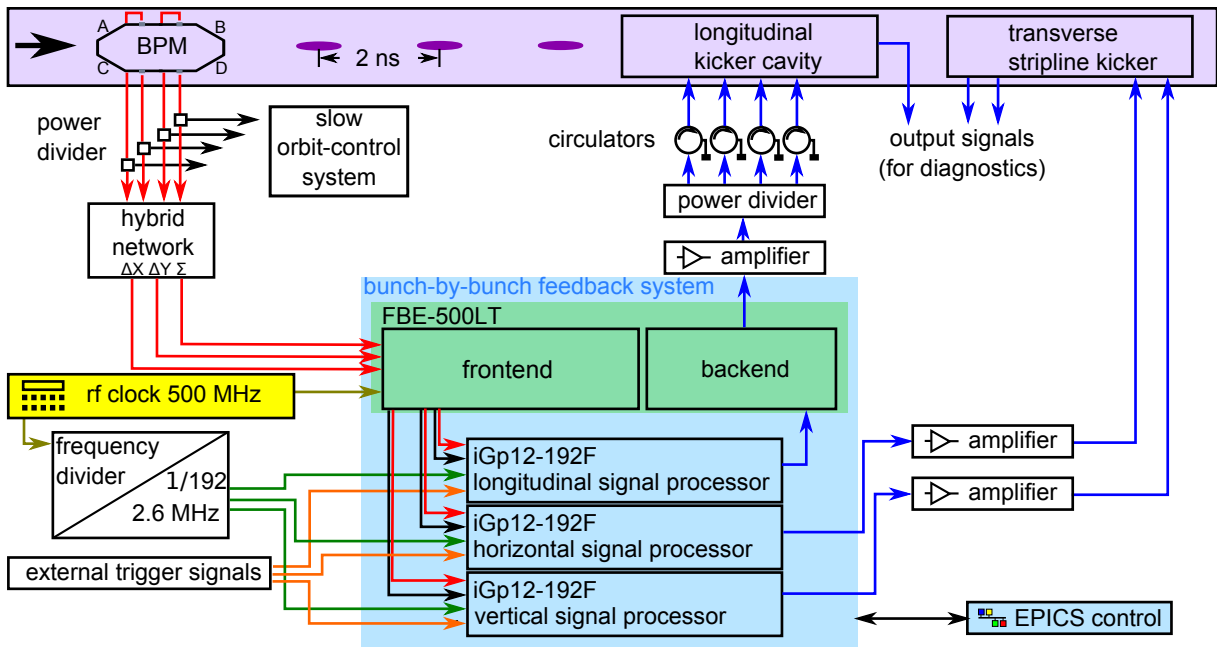

Figure 34: Signal-flow graph of the bunch-by-bunch feedback system including the detected input signal (red), the reference clock signals (green), external trigger signals (orange) and the output signals to the kicker structures (blue).

7.1.1 Beam-Position Monitor and Hybrid Network

The longitudinal, horizontal and vertical bunch position is determined by a beam-position monitor (BPM), a set of four pickup electrodes integrated in the DELTA vacuum chamber. Whenever an electron bunch passes the electrodes, a voltage is induced (see Fig. 35). The Gaussian-shaped electron bunch induces a Gaussian pulse, but due to the capacitive coupling the output signal is a differentiated pulse. Depending on the distance of the electron bunch, the amplitude of the detected signals at each electrode changes. While the sum signal could be created by a power combiner, the horizontal and vertical position is determined by comparing the either top and bottom signals or the left and right signals. All three signals are provided by a so called hybrid network (BPMH-20-2G [24]), which consists of four 180° hybrid couplers providing the sum and the difference of two input signals. The basic principle of the hybrid network creating the horizontal difference, vertical difference and sum signal is presented in Fig. 35.

Before the hybrid network, the signals are splitted by power dividers to serve the slow orbit correction system in addition to the bunch-by-bunch feedback system. The power dividers (ZN2PD2-50-S+[67]) have an operating bandwidth of 500 MHz to 5 GHz. The hybrid network has an operating bandwidth of 20 MHz to 2 GHz. This overall bandwidth is necessary, since the electron bunch length of 100 ps (FWHM) leads to a broad spectrum with a maximum at 3 GHz. In addition, the spectral component at 1.5 GHz, which is the digitization frequency of the processing units of the bunch-by-bunch feedback system is inside this bandwidth.

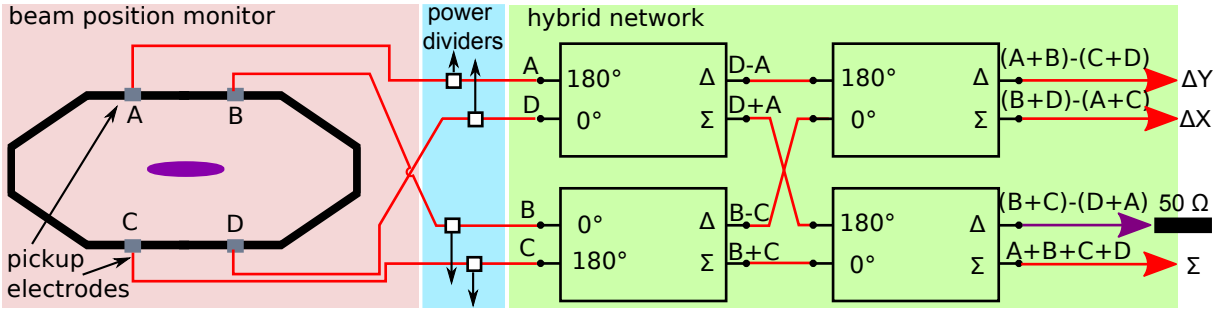

Figure 35: The induced signals from the pickup electrodes of the BPM (red) are directed to the hybrid network (green). A part of each signal is coupled out by power dividers. The hybrid network provides the horizontal difference, vertical difference and the sum signal. It consists of four hybrid couplers, which generate the differential (Δ) and sum (Σ) signal of the respective two input signals. The diagonal difference of the total hybrid network is terminated by a 50 Ω load.

7.1.2 Processing Units

The bunch-by-bunch feedback system consists of a combined frontend/backend module (FBE-500LT [24]) and three identical signal processing units (iGp-12-192F [24]) for the three planes. The three input signals from the hybrid network are at first processed in the frontend unit (see Fig. 36). Each input signal is stretched by a two-cycle comb filter to a pulse train of about 1.3 ns duration and is then mixed with a 1.5 GHz reference signal. The reference signal is an upconverted signal of the RF master.
A digital phase shifter allows to vary the phase of the reference signal. Since the pulse is finally passing a low-pass filter, the reference phase determines whether the output signal is proportional to the phase of the incoming signal or to its amplitude. The mixed signal

$$S(t) = A_1 \cdot \sin(\omega \cdot t + \phi_1) \cdot A_{\text{ref}} \cdot \sin(\omega \cdot t + \phi_{\text{ref}}), \tag{7.1}$$

with the amplitude A_1 and phase ϕ_1 of the input signal, the amplitude A_{ref} and phase ϕ_{ref} of the reference signal and the oscillation frequency ω. The relation can be transformed to

$$S(t) \sim A_1 \left[\cos(\phi_1 - \phi_{\text{ref}}) - \cos(2 \cdot \omega \cdot t + \phi_1 + \phi_{\text{ref}})\right], \tag{7.2}$$

where the second term is suppressed by the low-pass filter, resulting in

$$S(t) \sim A_1 \cdot \cos(\phi_1 - \phi_{\text{ref}}). \tag{7.3}$$

In the longitudinal plane, the input-signal amplitude is proportional to the beam current $A_1 = I_1$, which is given by the sum of all four pickup electrodes. By setting the reference phase to $\phi_{\text{ref}} = \pi/2$ and for small phase oscillations, the output signal is proportional to the input phase times the beam current

$$S_L(t) \sim A_1 \cdot \cos\left(\phi_1 - \frac{\pi}{2}\right) \approx I_1 \cdot \phi_1. \tag{7.4}$$

In the horizontal or vertical plane, the input-signal amplitude is proportional to the displacement of the bunch and its total current $A_1 = I_1 \cdot \Delta x,y$. By setting the reference phase to $\phi_{\text{ref}} = 0$, the output signal is not changing for small phase oscillations of the beam and is therefore only proportional to the displacement and the bunch current

$$S_{x,y}(t) \sim A_1 \cdot \cos(\phi_1) \approx I_1 \cdot \Delta x,y. \tag{7.5}$$

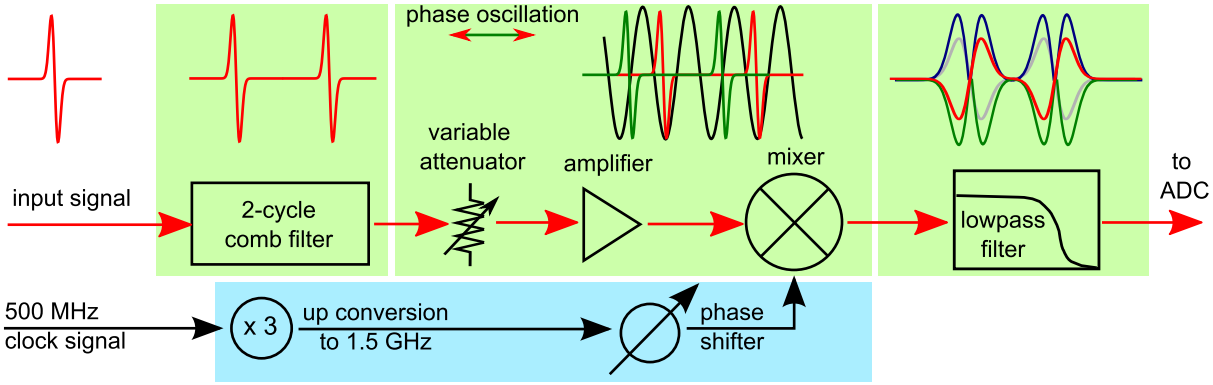

Figure 36: Signal-flow diagram of the feedback frontend unit. The signal shape after each element is shown. At the top-right, three possible signals are shown, which have a zero mean signal (red), a positive mean signal (blue) and a negative mean signal (green). How the output signal is shaped depends only on the phase (longitudinal plane) or amplitude (transverse planes) of the incoming pulse. However, the amplitude of the resulting signal is always proportional to the bunch current.

After preprocessing the input signal in the frontend module, the three signals for each plane are transferred to the signal processing units where they are digitized by 12-bit ADCs with a 500 MHz sampling rate. Therefore, one sample per bunch and revolution is taken, while the ADC is phase-locked to the RF master oscillator. Variable attenuators in the frontend module allow to use the full dynamic range of the ADC. To synchronize the bunch numbers with other components of DELTA, such as the filling pattern monitor, an external fiducial trigger can be supplied to the processing unit. This trigger is generated from the 500 MHz reference signal by using a 1/192 frequency divider.

After digitization, a finite-impulse response filter (FIR) is applied in order to calculate the output signal, which is fed back to the beam (see Section 4.3). In the current configuration of the system, the FIR-filter can use up to 24 taps. Furthermore, the digitized data is stored for all 192 buckets over up to 65000 turns. In addition, the data acquisition can be triggered on external events.

An additional 3-tap FIR filter can be used to shape the pulse of the outgoing signal. This helps to reduce the crosstalk to other buckets [68]. An overview of the signal flow is given in Fig. 37. The output signal calculated by the FIR filter is then converted to an analog signal by a DAC.

In case of the horizontal and vertical plane, the analog signal is directly sent to the power amplifier and the corresponding stripline kicker. In the longitudinal plane, the output signal of the DAC is sent to the backend module of the FBE500-LT where the output signal is upconverted to 1.5 GHz by using a phase mixer and a bandpass filter with a bandwidth of 550 MHz. This upconversion is necessary since the kicker cavity is operating at this higher frequency band. To fine-tune the output signal, the phase of the reference signal of the backend module can be varied. The signal-flow diagram of the backend module is given in Fig. 38.

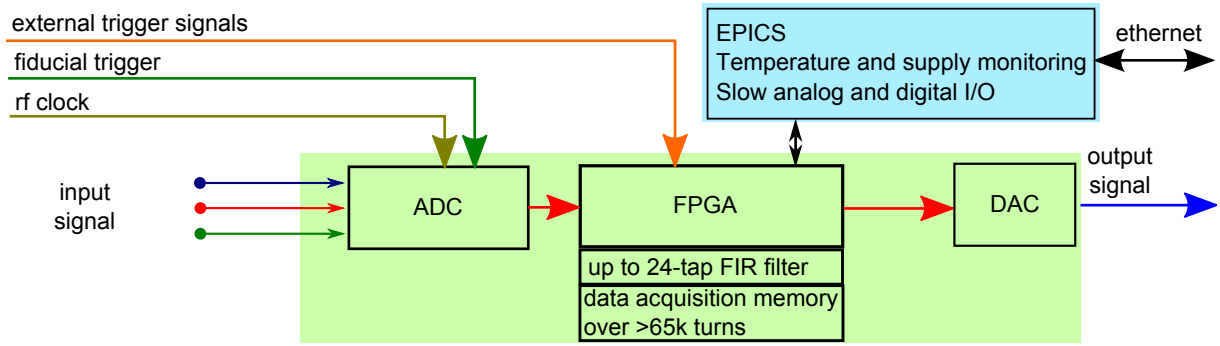

Figure 37: Signal-flow diagram of a signal processing unit. The ADC takes one sample per bunch. After processing the signal in the FPGA the DAC creates a output signal.

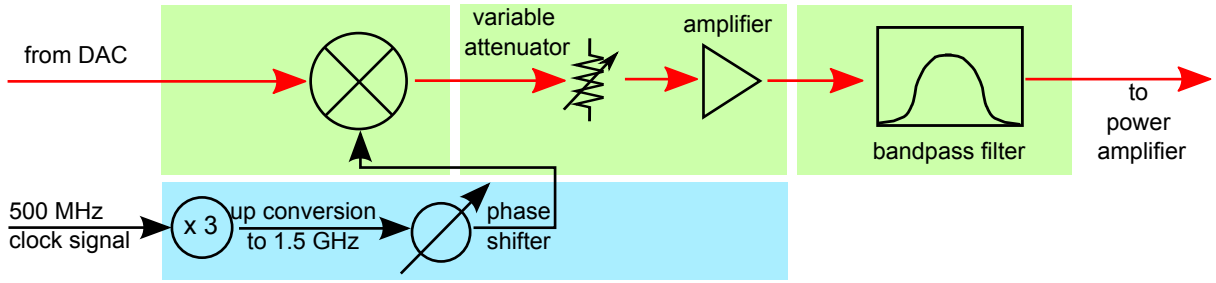

Figure 38: Signal-flow diagram of the backend module which is part of the FBE500-LT. The backend module upconverts the longitudinal output signal to the 1.5 GHz band of the kicker cavity.

7.1.3 Amplifier and Kicker Structures

The output signal of the bunch-by-bunch feedback system from the backend module (longitudinal) or directly from the signal processing units (transverse) is amplified. In the longitudinal plane, a *Milmega AS0102-200* [69] amplifier is used, which has an operation bandwidth of 1 GHz to 2 GHz, a gain of $g = 59\,\mathrm{dB}$, a saturation power of $P_{\mathrm{sat}} = 54.8\,\mathrm{dBm}$ and a 1-dB compression power of $P_{1\mathrm{dB}} = 54.7\,\mathrm{dBm}$. In order to operate the amplifier in its linear regime, a maximum input power of $P_{\mathrm{in}} = P_{1\mathrm{dB}} - g = -4.3\,\mathrm{dBm}$ should not be exceeded. Therefore, the backend attenuation was set to 16 dB in order to limit the longitudinal output signal of the feedback system to this value.

For the horizontal and vertical plane, two *Amplifier Research 100A250A* [70] amplifiers are in use. The operation bandwidth of these amplifiers is 10 kHz to 250 MHz. They have a gain of 50 dB and a 1-dB compression power of $P_{1\mathrm{dB}} = 54.7\,\mathrm{dBm}$. Thus, an input power of $P_{1\mathrm{dB}} = 4.7\,\mathrm{dBm}$ should not be exceeded. Finally, the amplified signals are sent to the kicker structures.

The structures are slightly modified versions of those used at BESSY II [71, 41]. While the basic geometry is the same, tapering to the DELTA vacuum chamber was required. In the longitudinal plane, a kicker cavity is used. In order to be able to damp each multibunch

mode, the kicker bandwidth must be at least $\Delta f = 250\,\mathrm{MHz}$. To achieve this, the cavity is highly damped by eight waveguides resulting in a quality factor of $Q = f_c/\Delta f \approx 5.5$ with a central frequency of $f_c = 1374\,\mathrm{MHz}$. The signal from the power amplifier is splitted into four by a power divider, which are driving the kicker structure. To protect the power amplifier from reflected power, circulators are inserted in the signal path to redirect any reflected signal to a 50-Ω load. The outgoing four waveguides of the kicker are terminated by 50-Ω loads as well. For diagnostics purposes, the output signal of one of these ports is forwarded to the outside of the radiation shielding wall.

In the transverse planes, a combined stripline kicker with two perpendicular pairs of electrodes (see Fig. 39) is used, which minimizes the total structure length in contrast to two individual stripline kickers. The electrodes match the geometry of the vacuum chamber to reduce the loss factor of the kicker. At DELTA, only one electrode is connected to the amplifier and the second one is kept floating. In case of the stripline kicker, the signal is coupled in from the downstream port. All outgoing power, either from the input signal itself or induced by the electron beam, is coupled out through the upstream port. Therefore, no circulators are necessary in the signal path. The signal from the upstream port is available outside of the shielding wall for diagnostic purposes and is terminated by a 50-Ω load, whenever not used. The stripline kicker operates in the baseband and has a bandwidth of 250 MHz. The shunt impedance depends on the operating frequency and varies from 10 kΩ at 1 MHz and 4 kΩ at 250 MHz in the horizontal plane. Due to geometry, in the vertical plane the shunt impedance is higher and varies from 20 kΩ at 1 MHz and 2 kΩ at 250 MHz [41]. Figure 39 shows the cross sections of the kicker structures.

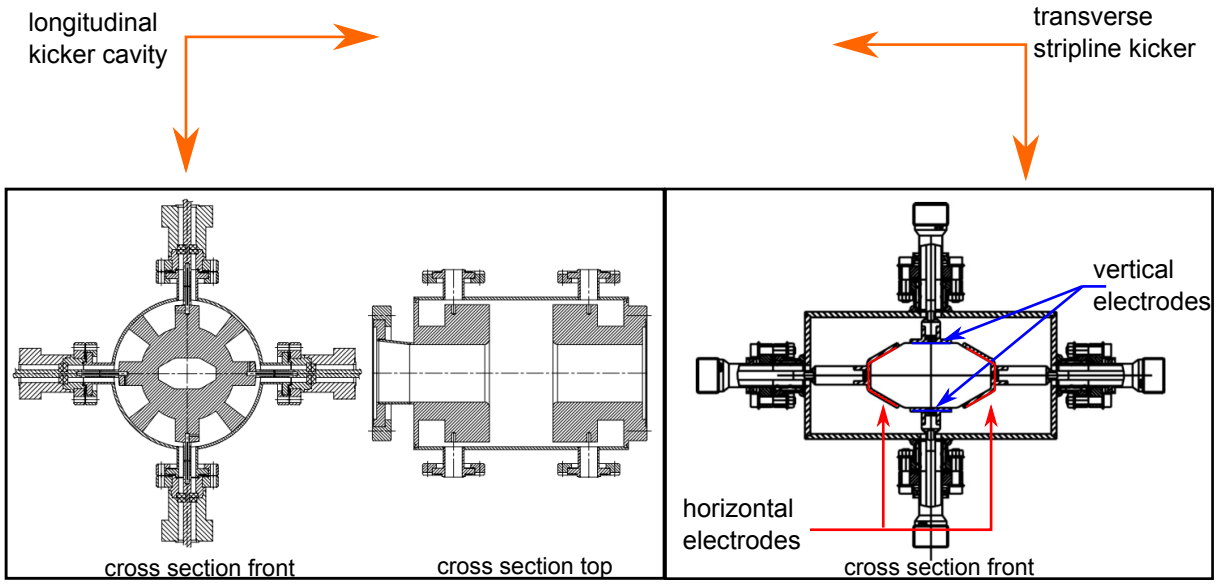

Figure 39: Cross section of the longitudinal kicker cavity (left) and the transverse stripline kicker (right) as installed at the DELTA storage ring (top) (from [41, 71]).

7.2 The Streak Camera

In order to compare beam dynamics studies performed with the bunch-by-bunch feedback system with other data sources, an *Optronis* streak camera [72] was used. The streak camera allows to detect the longitudinal motion of the electron bunches on a timescale of several picoseconds.

7.2.1 Modes of Operation

The streak camera detects the synchrotron radiation emitted from every bunch (see Fig. 40). First, the radiation pulse is focused to the input slit of the streak camera, where the input optics transfers the light pulse to the photo cathode. There, a certain amount of photo electrons proportional to the light intensity is emitted. Therefore, the bunch of photo electrons has the same temporal shape as the incident light pulse. Due to an accelerating gradient, the electrons propagate towards a phosphor screen. Before reaching the screen, high-voltage deflection plates change the transverse direction of the photo electrons. This correlates the temporal shape of the incident light pulse with the spatial distribution of the photo electrons hitting the screen. In addition, a multi-channel-plate (MCP) increases the number of electrons before hitting the screen. Finally, a CCD camera detects the light emitted by the phosphor screen. In order to observe the incident light pulse, the high-voltage plates and the CCD camera must be triggered. By changing the amplitude or rise time of the deflecting voltage, the resolution of the image can be changed. The maximum achievable resolution is of the order of a few picoseconds. In case of a long rise time, beam dynamics can be observed over several milliseconds. However, in that case the resolution is much smaller and is of the order of some microseconds.

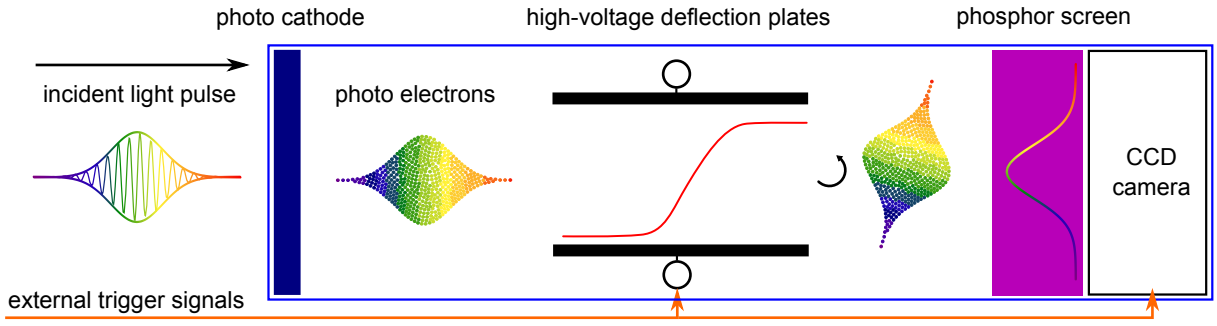

Figure 40: Basic principle of a streak camera. The incident light pulse is transformed to photo electrons which are deflected in the streak tube. By detecting the transverse intensity profile of a phosphor screen with a CCD camera, the initial longitudinal pulse shape information is obtained. The color of the pulses indicates the arrival time on the photo cathode.

Instead of having one transverse deflection for each trigger pulse, it is also possible to use a sinusoidal deflecting voltage. In this so-called synchroscan mode, a deflection frequency of 125 MHz, which is a quarter of the bunch repetition rate of 500 MHz, is used. The phase of

the deflecting voltage has a fixed phase relationship to the DELTA master oscillator. The phase can be shifted by software control. Since the deflection frequency is a quarter of the repetition rate, every fourth bunch is visible at the same place on the phosphor screen. By changing the phase relative to the master oscillator, the position on the phosphor screen and in the final CCD image can be changed. Some example configurations are shown in Fig. 41. To visualize small phase oscillations of every bunch over a wide time range, both deflecting modes can be used simultaneously. Therefore, a second pair of deflection plates is installed in the streak tube perpendicular to the first deflection plate. This results in a two dimensional image, where one axis corresponds to the fast time scale of the synchroscan unit (picosecond regime), and the second axis corresponds to a comparatively slow time scale of the single streak unit (millisecond regime).

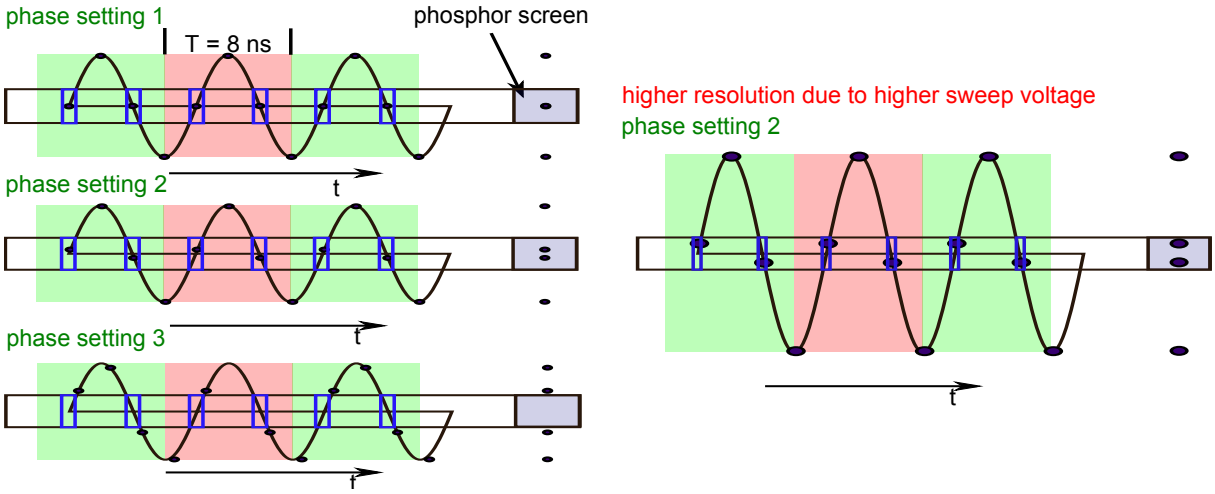

Figure 41: Synchroscan mode of the streak camera. A high frequency deflection voltage allows to integrate the light of several subsequent bunches at one position of the phosphor screen. By changing the delay of the deflection voltage, the bunch position on the screen changes. It is possible to have one spot (left, top), two spots (left, center), which is the standard operation mode, or no spot at all (left, bottom). By increasing the deflection-voltage amplitude the resolution of the streak camera is increased (right), since each bunch of photo electrons is streaked over a larger area of the phosphor screen.

8 Experimental Studies of Beam Instabilities

In this chapter, the experimental investigations of multibunch and single-bunch instabilities at DELTA are described in detail and are compared with simulations performed with the simulation tool presented in Sect. 5. At first, the input and output timing and the calibration of the feedback units to enable the correct functionality of the system is presented. Next, a measurement of the synchronous phase of the bunch train is discussed which allows to cross-check the longitudinal calibration. The determination of multibunch damping times represents the main content of this chapter. The chapter closes with the analysis of single-bunch instabilities.

8.1 Input Timing and Calibration

8.1.1 Amplitude and Phase Detection

In order to detect and digitize the longitudinal or transverse bunch position, the feedback unit must be either in phase-sensitive mode (longitudinal plane) or in amplitude-sensitive mode (transverse plane), as explained in Sect. 7.1.2. To find the correct phase setpoint, the phase of the reference signal is varied in several hundred steps ϕ_i while detecting the mean bunch signal for a measurement interval of 25 ms. Without calibration, the mean bunch signal is given by the measured ADC value $S(\phi_i)$ and varies in an interval of $[-2000, 2000]$. Ideally, the resulting curve would be sinusoidal as given in Eq. 7.3.
Due to non linearities of the system, the detected curve deviates strongly from the sinusoidal shape at low and high phase shifter settings. In Fig. 42, one measurement is shown as an example. Nevertheless, the maximum at about phase-shifter step 1400 may be used for

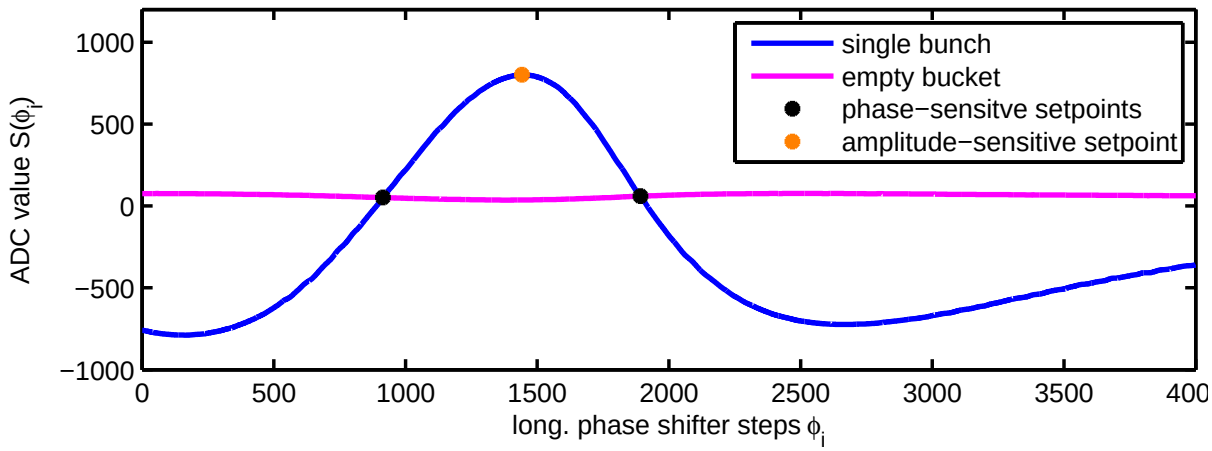

Figure 42: Variation of the longitudinal phase shifter. The mean signal of a single bunch (blue) varies with phase, while the empty reference bucket (magenta) shows only small changes. The possible phase-sensitive setpoints (black) are at the steps 910 and 1820. As reference, the amplitude-sensitive setpoint at 1480 step (orange) is marked, which is not usable for the longitudinal unit.

amplitude-sensitive measurements and the zero crossings at step 800 or 1800 for phase-sensitive measurements. The shown measurement was taken at a bunch current of about 8 mA, an input attenuation of 8 dB and an ADC delay of 200 ps. The ADC delay is an internal delay which determines the digitization timing of the ADC. The cavity power was 26 kW. It is important to note that even the empty buckets show a non-zero mean signal. This so-called mixer offset has a small variation over phase as well and shifts the measured mean signal of the single bunch accordingly. The above parameters influence the shape of the curve as will be shown in the following sections. In addition, different filling patterns change the synchronous phase of the bunches, which results in small changes of the optimum phase shifter setting.

As mentioned before, the ADC delay of the processing unit influences the optimum phase setpoint. In addition, it also increases the sensitivity and stability of the measured mean signal. In Fig. 43, the variations of a whole phase scan, as shown in Fig. 42, is plotted versus the ADC delay. It shows a broad flat top from 50 to 350 ps. Thus, the optimum ADC delay was set to 200 ps.

So far, the optimum ADC and phase shifter settings were discussed for the longitudinal unit. For the horizontal and vertical unit the procedure is the same. Each unit has an individual phase shifter and ADC delay. In contrast to the longitudinal unit, the amplitude-sensitive setpoints are used for the transverse plane. The resulting parameters are summarized in Tab. 3. In the horizontal plane, the input attenuation is much smaller than in the other two planes, since the beam is better horizontally centered, which creates a small input signal. It is important to note that the phase-shifter setpoint must be slightly changed whenever

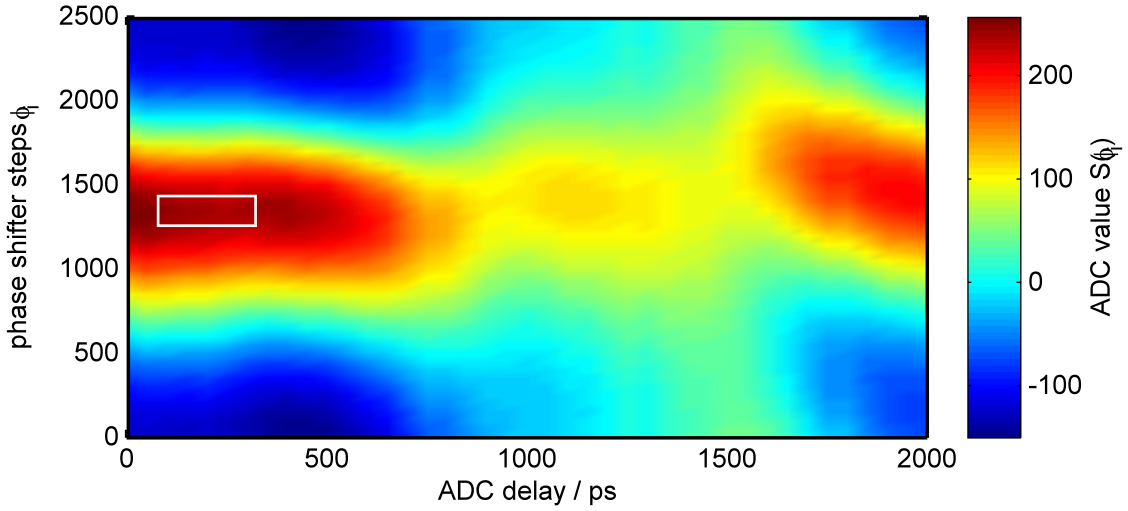

Figure 43: The ADC value $S(\phi_i)$ (color-coded) is plotted as a function of the phase shifter steps and the ADC delay. The area with the largest ADC value and low variation with the ADC delay is marked with the white rectangle. The ADC delay was, therefore, set to 200 ps. The measurement was performed at a bunch current of 0.8 mA.

the bunch synchronous phase varies, for example due to a different cavity power or filling pattern. The feedback system provides an automatic phase-servo loop, which keeps the longitudinal unit in the phase-sensitive regime. To do so, the loop compares the beam signal of the filled buckets with the empty buckets and changes the phase shifter until these signals are identical. The transverse units can be coupled to the longitudinal one, so that phase changes by the phase-servo loop can be applied to all three units.

Table 3: Overview of the main parameters for the detection of the input signals.

	phase-shifter setpoint	ADC delay	attenuation
longitudinal unit	1890 steps	200 ps	14 dB
horizontal unit	1800 steps	440 ps	4 dB
vertical unit	1740 steps	600 ps	16 dB

8.1.2 Bunch-Current Correction

The measured bunch signal is always proportional to the bunch current (cf. Sec. 7.1.2). To compare different measurements, they should be normalized by the bunch current. Since even the empty buckets show the mixer offset $M(\phi_i)$ with the phase shifter step ϕ_i, the corrected signal S_C is given by

$$S_C(\phi_i) = \frac{S(\phi_i) - M(\phi_i)}{I_B(\phi_i)}$$

with the measured signal $S(\phi_i)$ and the bunch current $I_B(\phi_i)$ in mA. Since the bunch current is decreasing during the measurement, a different bunch current is used for the normalization at each phase step. Figure 44 shows different phase scans for different bunch currents before and after normalization.

The signal of an empty bucket (mixer offset) shows a small variation with the phase as well. While the signal strength and the mixer offset can be determined by the feedback system, the bunch current can not directly be measured. At DELTA, there are three methods to determine the bunch current. For all methods, the total beam current is measured by electromagnetic inductance using a parametric current transformer of the type described in [73]. Next, the ratio of the bunch charges in the different buckets must be measured. This can be either done with a fast oscilloscope connected to at one of the BPMs providing the DELTA filling pattern [74], or it can be extracted from a dataset provided by the feedback system. From the feedback dataset, there are two possibilities to extract the relative bunch

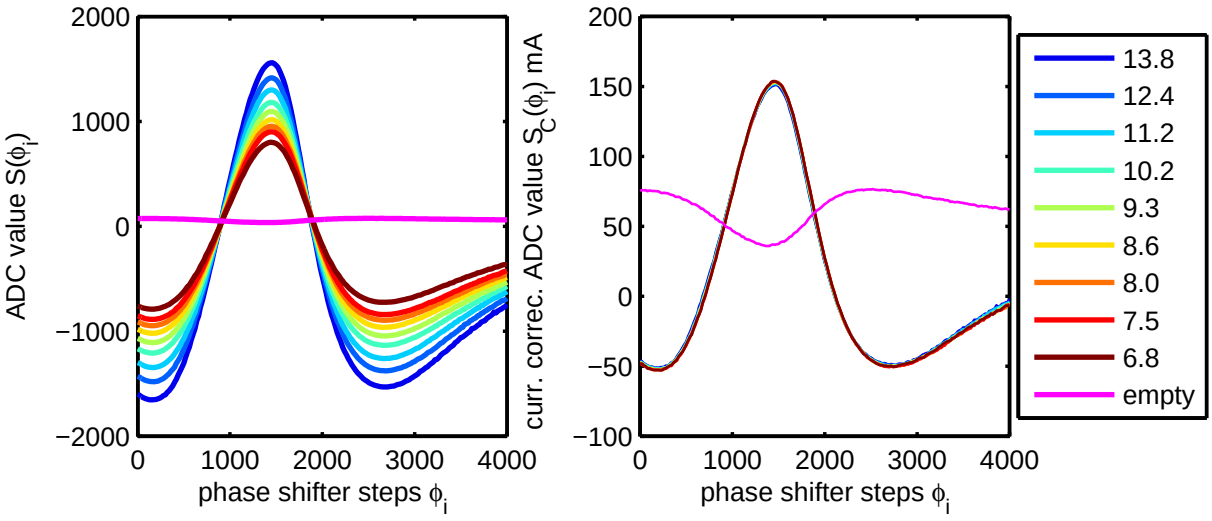

Figure 44: Phase variation for different bunch currents (left). After current correction, the different curves are identical (right). As reference, the signal of an empty bucket (mixer offset) is plotted (magenta). The legend contains the bunch currents in mA at the beginning of each measurement.

charge. The first is to set the longitudinal processing unit to the amplitude-sensitive regime, since then the detected signal is only proportional to the beam current. However, in this configuration the longitudinal unit can not used for beam diagnostics anymore. Therefore, a better solution to determine the ratio of the bunch currents is based on the bunch spectrum and does not require a change of the phase shifter setpoint. While the high frequency components result from the bunch oscillation relative to the synchronous phase, the low frequency components result from slow orbit oscillations and would therefore be identical for each bunch, if they would have the same bunch current. In case of different bunch currents, the strength of these frequency components varies between the buckets and directly reflects the ratio of the respective bunch charges.

8.1.3 Input Attenuation

In the previous section, the input attenuation was set to a fixed value in a way that the full dynamic range of the ADC is used. Since the previous examples were measured in single-bunch mode, in which the bunch current is up to 25 mA, the ADC requires a large input attenuation. In multibunch mode, the bunch current is 1 mA at the most, which allows to reduce the input attenuation in order to increase the dynamic range of the ADC. To compare the measured signal strengths in single-bunch or multibunch mode, the signal should be corrected by the input attenuation value. The corrected signal strength $S_{CA}(\phi_i)$ is given by

$$S_{CA}(\phi_i) = S_C(\phi_i) \cdot 10^{\frac{a}{20}}$$

with the attenuation value a in dB. Figure 45 shows the current-corrected ADC value S_C for different attenuation values. The attenuation and current-corrected phase scan has a signal amplitude of $S_{CA} = \pm 500/\text{mA}$ (c.f. Fig. 46).

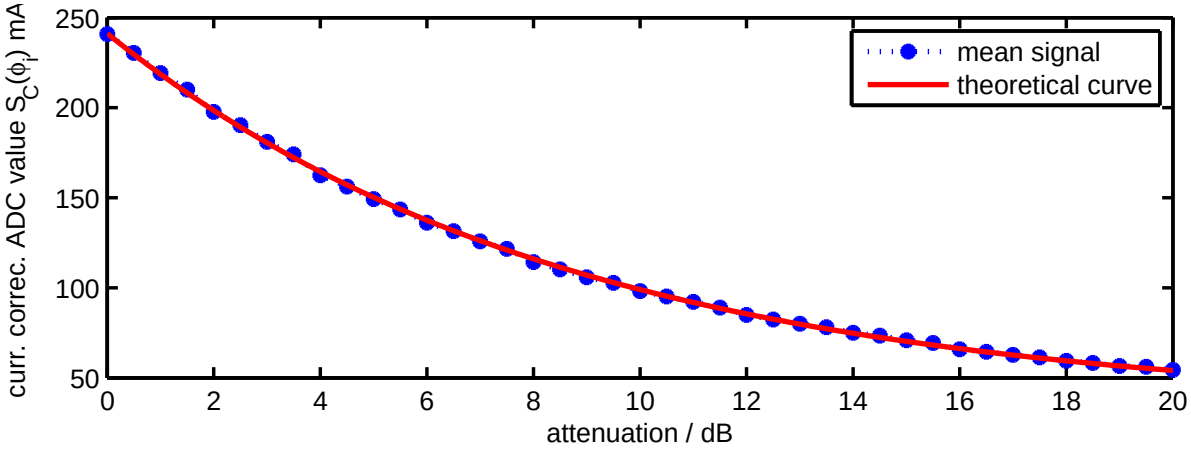

Figure 45: Current-corrected ADC value S_C for different attenuation values.

8.1.4 Absolute Calibration of the Longitudinal Unit

The phase shifter steps ϕ_i and the mean signals $S(\phi_i)$, $S_C(\phi_i)$ and $S_{CA}(\phi_i)$ do not reflect the absolute bunch phase or the absolute transverse excursion, since no external calibration was performed. In order to calibrate the longitudinal unit, the knowledge of the external 1.5 GHz reference signal is used. Moreover, the detected mean signal can be correlated to a phase change in the phase-sensitive linear regime of the unit.
The corrected ADC value shows a sinusoidal shape in the center of the phase-shifter scan. From a sinusoidal fit, the oscillation period of the sine wave can be expressed in terms of phase shifter steps. The sinusoidal fit

$$S_{CA}(\phi_i) = S_1 \cdot \sin\left(\underbrace{a \cdot (\phi_i - \phi_0)}_{\Phi}\right) + S_0$$

results to the following fit parameters:

$$\begin{aligned} a &= 3.23 \cdot 10^{-3}/\text{steps} \\ \phi_0 &= 826\,\text{steps} \\ S_1 &= 565 \\ S_0 &= 42.38 \end{aligned}$$

For one period of the sine wave, the phase difference $\Delta\Phi$ at 1.5 GHz equals 2π. From the relation

$$\Delta\Phi = a \cdot \Delta\phi,$$

the calibration for the phase shifter steps is obtained

$$\Delta\phi = \frac{2\pi}{a} = 1948\,\text{steps}.$$

One phase shifter step corresponds to 0.554° at 500 MHz, which is the RF frequency. Moreover, this phase shift can be transformed into a time delay. One phase shifter step corresponds to a delay of 0.342 ps.
A linear fit to the datapoints next to the zero crossing yields that a change in the ADC value of $\Delta S_{CA} = 1$ corresponds to -0.19 ps. Figure 46 shows the calibration measurement and the appropriate fits.

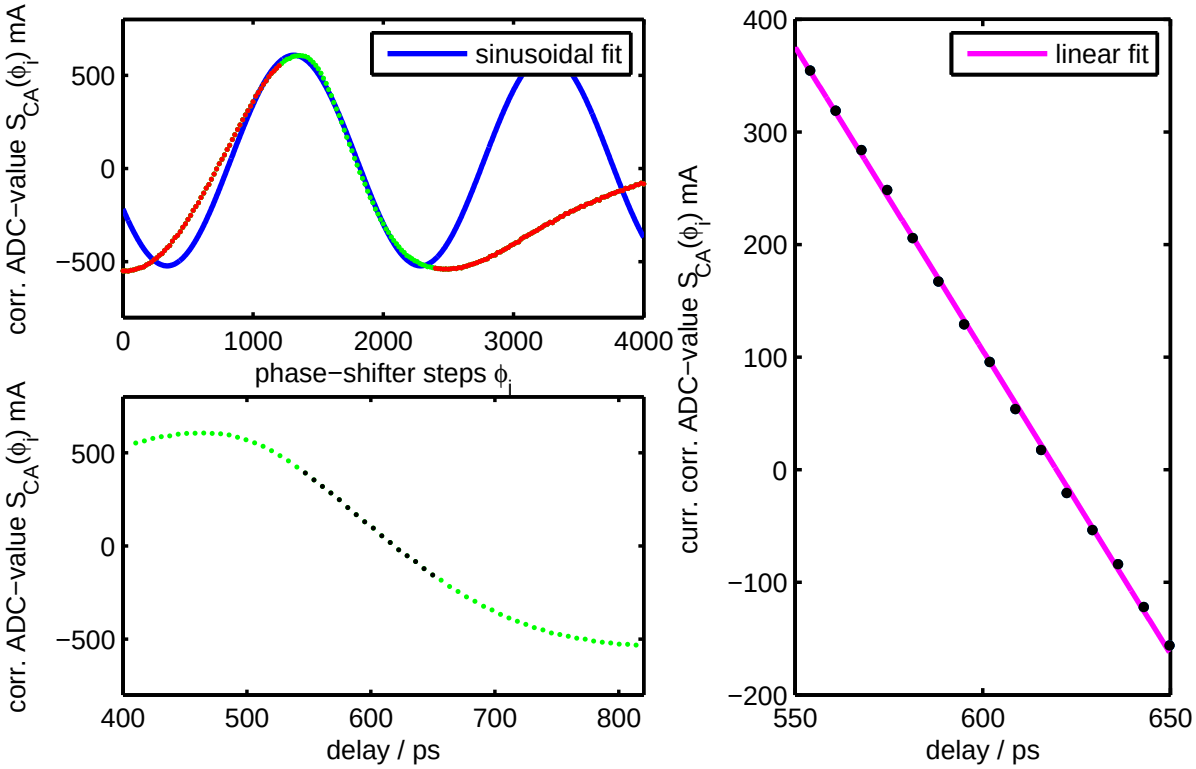

Figure 46: Absolute calibration of the longitudinal feedback unit. A longitudinal phase scan with current and attenuation correction is shown in red (top, left). Green dots indicate the fit area for the sinusoidal fit, which is plotted in blue. From the sinusoidal fit, the phase-shifter steps can be converted to a longitudinal delay (bottom, left) with the linear regime in black. A linear fit (magenta, right) allows to convert the current- and attenuation-corrected ADC-value S_{CA} to a longitudinal delay of the input signal.

8.1.5 Absolute Calibration of the Transverse Units

For the calibration of the transverse units, the corresponding phase shifter is set to the amplitude-sensitive regime (c.f. Tab. 3). In the next step, the orbit position at BPM 16, to which the feedback units are connected, is changed by the slow orbit correction system, which automatically creates an orbit bump to reach the given orbit excursion.
After correcting for the bunch current and the input attenuation, the measured ADC signals are plotted against the respective orbit position. A linear fit provides the transverse absolute calibration of the feedback units (cf. Fig. 47). In the horizontal plane, the linear fit

$$S_{\mathrm{C,x}}(x) = m_{\mathrm{H}} \cdot x + n_{\mathrm{H}}$$

results in the fit parameters:

$$\begin{aligned} m_{\mathrm{H}} &= -32 \, \frac{1}{\mathrm{mA\,mm}} \\ n_{\mathrm{H}} &= 151 \, \frac{1}{\mathrm{mA}}. \end{aligned}$$

This means that a change in the ADC value of $\Delta S_x = \pm 1$ corresponds to a position change of $\mp 32\,\mu\mathrm{m}$, if the beam current is 1 mA and no attenuation is applied. Analogously, in the vertical plane, the linear fit

$$S_{\mathrm{C,y}}(y) = m_{\mathrm{V}} \cdot y + n_{\mathrm{V}}$$

results in the fit parameters:

$$\begin{aligned} m_{\mathrm{V}} &= -7 \, \frac{1}{\mathrm{mA\,mm}} \\ n_{\mathrm{V}} &= 391 \, \frac{1}{\mathrm{mA}}. \end{aligned}$$

Here, a change in ADC value of $\Delta S_y = \pm 1$ corresponds to a position change of $\mp 142\,\mu\mathrm{m}$, if the beam current is 1 mA and no attenuation is applied.
Due to the so-called pincushion distortion of the BPM for large deviation of the beam from the central position, the error of the derived calibration is of the order of 5 µm.
Although the absolute calibration is sometimes useful, for many applications like determination of damping rates only the relative change is important. Therefore, the following measurements use normalized coordinates for simplicity, whenever no absolute value is necessary. In addition, it is important to note that the orbit position at the feedback BPM is not fixed over time, but can change from time to time . Therefore, the absolute calibration must be repeated, whenever the orbit position is significantly changed.

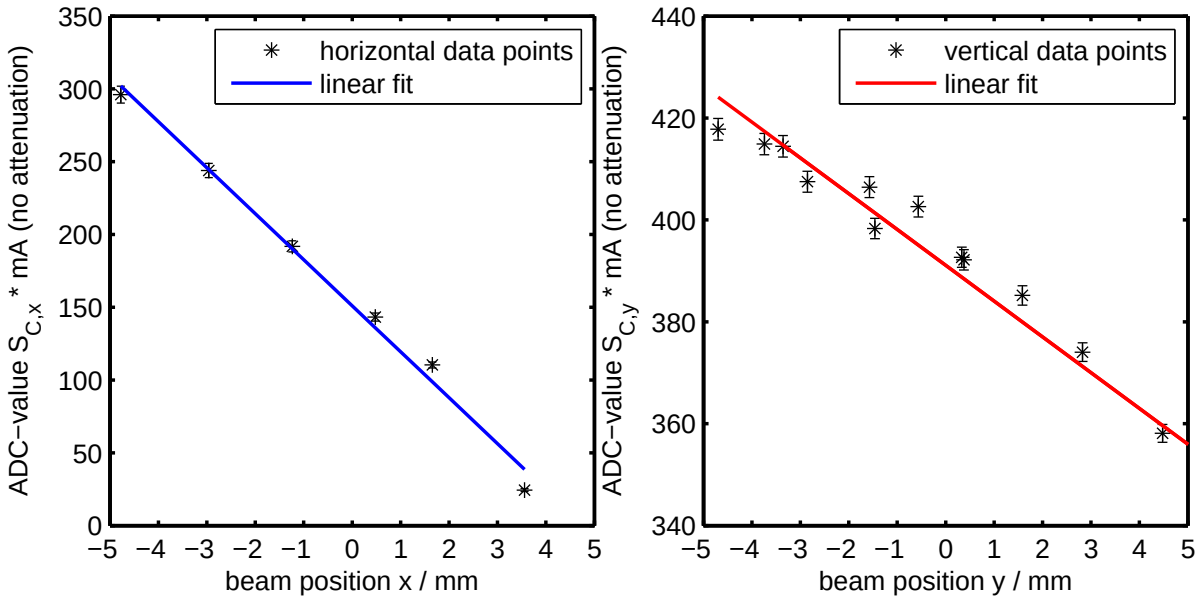

Figure 47: Absolute calibration of the horizontal (left) and vertical (right) feedback units. The BPM position obtained from the orbit correction system is related to the current-corrected ADC values obtained by the feedback system.

8.2 Output Timing

While the input timing is responsible for a correct digitization of the bunch position, the output timing must be set up correctly to interact with the desired electron bunch.
In order to set up the system, the machine is filled with a single bunch. Then, the internal NCO is switched on to excite that bunch. If the timing is wrong, the feedback system does not excite the single bunch. By changing the so-called output delay, the timing is changed in steps of 2 ns, until the single bunch is excited. This process can be sped up if a binary search is applied, where the first half of the buckets and then a quarter of the buckets and so on are excited, until the correct output delay is found. For fine-tuning, the so-called DAC delay is scanned from zero to 2 ns. As an example, a delay scan over 10 ns is shown in Fig. 48. Here, the spectral component at the synchrotron frequency of the single bunch spectrum is observed while the output and DAC delay is varied. The maximum spectral component of the single bunch indicates the correct output timing.
Unfortunately, due to the pulse lengthening of the excitation signal by the amplifier, there is a excitation of the single bunch if the previous bucket is excited (smaller delay, 16.0 dB) and if the following bucket is excited (larger delay, 25.7 dB). Therefore, in multibunch mode, in which the time interval between consecutive bunches is 2 ns, the excitation of one bunch always results in a small excitation of the following bunches. Alternatively, the DAC delay can be set in a way that the suppression before and after the bunch is equal. In that case, the maximum amplitude is reduced. Depending on the requirements of the measurement, one or the other delay setting is used.

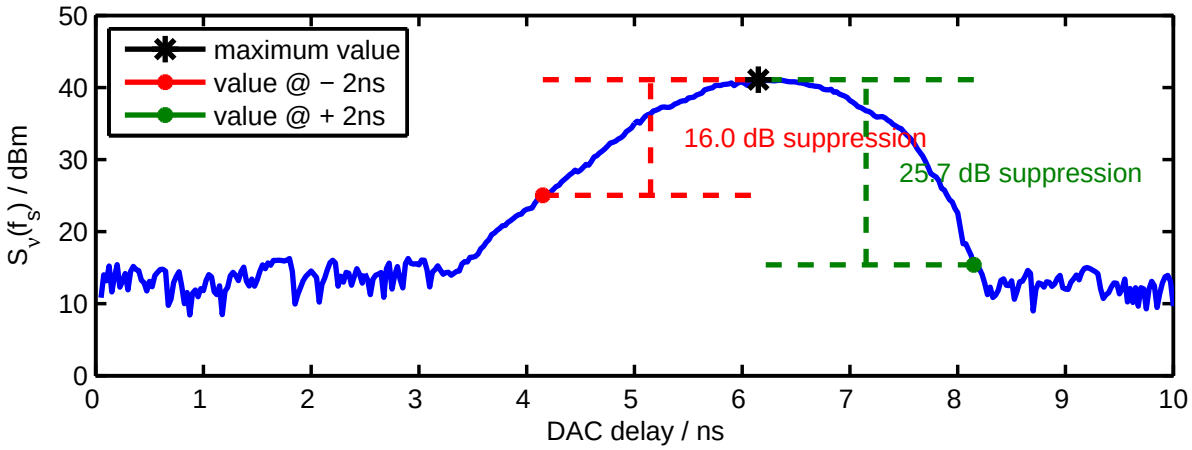

Figure 48: Scan of the longitudinal output and DAC delay (here combined to a common delay) while observing the spectral component at the synchrotron frequency as a measure for the oscillation amplitude. At a delay of 6.2 ns, the timing is set correctly, showing a maximum excitation of the single bunch. The asymmetry results from amplifier ringing. The red and green lines indicate the suppression of the single bunch, if the previous bucket (red) or the following bucket (green) is excited.

In the transverse plane, the amplifiers even more lengthen the excitation pulse compared to the longitudinal plane. In Fig. 49, the vertical excitation of the single bunch is depicted depending on the output and DAC delay. The suppression of the excitation is determined to be 12.7 dB when the previous bucket is excited and 14.4 dB when the next bucket is excited. However, even an excitation 18 ns in advance leads to a significant excitation of the single bunch.

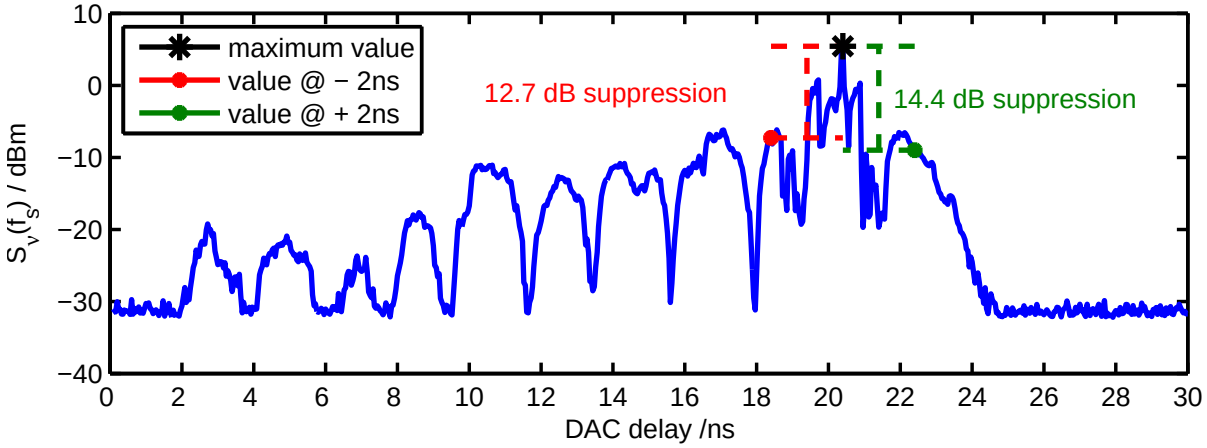

Figure 49: Scan of the vertical output and DAC delay (here combined to a common delay) while observing the spectral component at the synchrotron frequency as measure for the oscillation amplitude. At a delay of 20.4 ns, the single bunch shows maximum excitation. The red and green lines indicate the suppression of the single bunch, if the previous bucket (red) or the following bucket (green) is excited.

8.3 Synchronous Phase Measurement

In the previous sections, the phase of the bunch was assumed to be constant. Whenever the bunch phase changes, the maximum and the zero crossing of the phase calibration curve shifts as depicted in Fig. 50. While for small phase changes the ADC value changes linearly with input bunch phase, for larger phase changes the position of the zero crossing is a better indication for the observed phase shift.

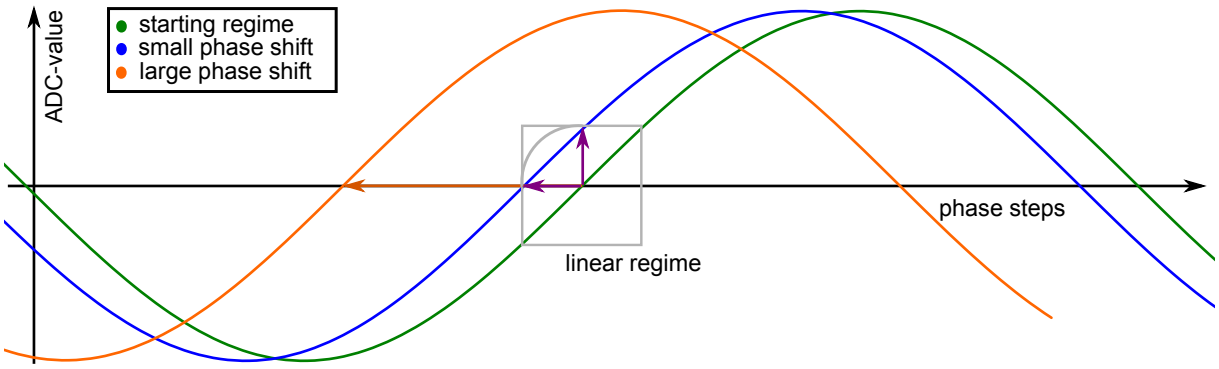

Figure 50: Sketch of the variation of the longitudinal phase shifter. The green line corresponds to the standard settings of the machine, whereas the blue line corresponds to a signal of a phase-shifted electron bunch. In the linear regime of the curves, the change of the ADC value is equivalent to the shift between the two curves. In the sketch, this is indicated by the purple arrows, which are proportional to each other. In case of large phase shifts of the electron bunch (orange curve), the ADC value can no longer used as measure of the phase shift and the position of the zero crossing is used instead.

The synchronous phase ϕ_S of an electron bunch depends on the cavity voltage or power and is given by (e.g. [25])

$$\phi_S = \pi - \arcsin\left(\frac{V_\mathrm{S}}{\sqrt{P \cdot R_S}}\right) \tag{8.1}$$

with the voltage V_S which is necessary to compensate for energy losses of the electrons during one turn, the cavity power P and the shunt impedance of the cavity R_S. At DELTA, a typical value for the shunt impedance is $3\,\mathrm{M\Omega}$, while V_S can be calculated according to [26]

$$V_\mathrm{S} = \frac{e}{3\varepsilon_0 \left(E_0\right)^4} \cdot \frac{E^4}{R} \approx 135\,\mathrm{kV} \tag{8.2}$$

with the bending radius of the dipole magnets R, the beam energy E, the electron rest energy E_0, the vacuum permittivity ε_0 and the elementary charge e. All insertion devices were switched off during the measurement.

While all other parameters were kept constant, the cavity power was changed in order to observe a change in synchronous phase. Figure 51 shows six phase scans for different cavity power, which were normalized to the interval $[-1,1]$.

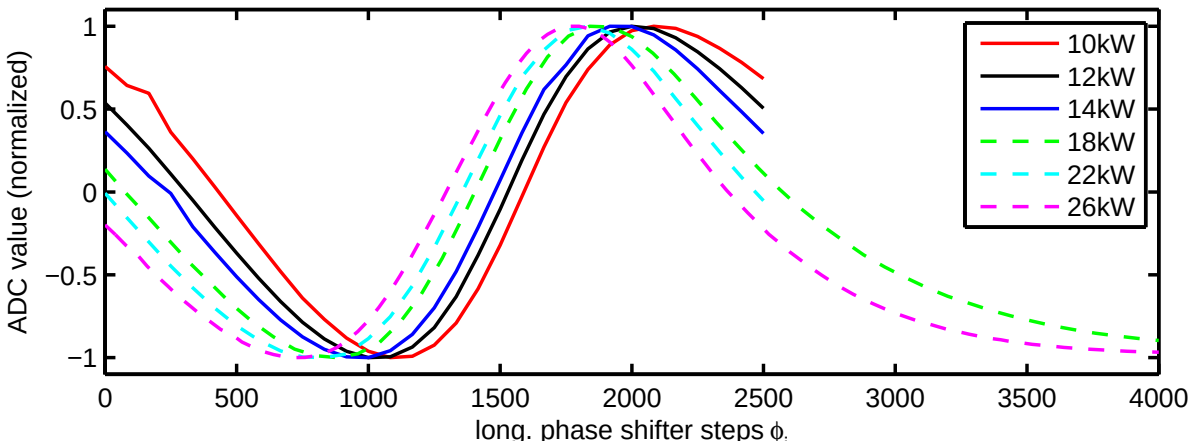

Figure 51: Longitudinal phase scan for different values of the power of the DELTA cavity. The position of the zero crossing shifts, which indicates a change of the synchronous phase of the electron bunch.

From the previous calibration of the longitudinal phase shifter, the different position of the zero crossing, i.e., the synchronous phase of the electron bunch can be expressed in terms of a delay of the electron bunch. In the observed interval, the delay changes by 100 ps when changing the cavity power from 10 kW to 26 kW. In Fig. 52, the measured change in arrival time of the electron bunch due to a variation of the cavity power is compared to the expected change according to Eq. 8.1. The measurement shows a qualitatively good agreement with the analytical calculation.

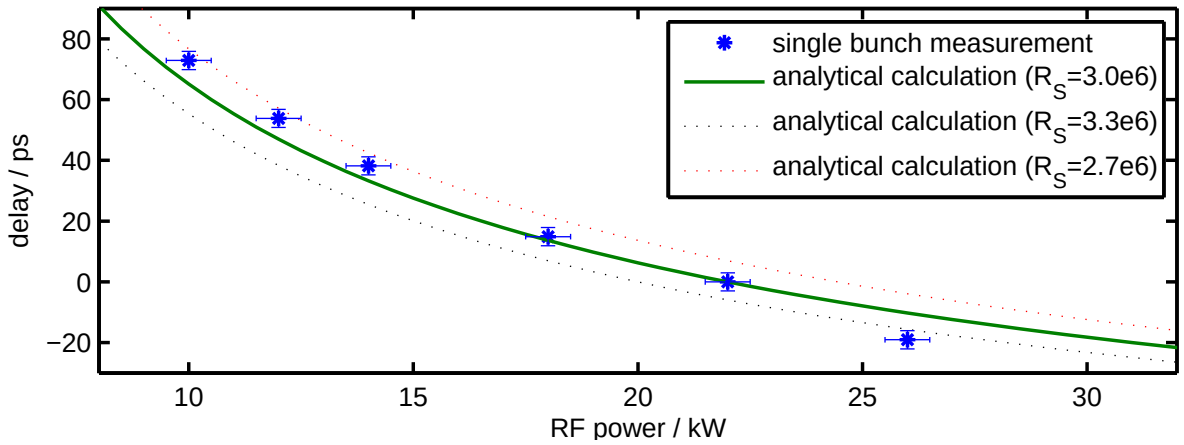

Figure 52: Relative delay of the electron bunch for different values of the RF power of the DELTA cavity. The measured data points (blue) are compared to the analytical calculation (green). In addition, the analytical calculation was repeated for a slightly smaller (red) and a slightly larger (black) shunt impedance. The delay was calculated relative to the value at 22 kW. Since the cavity power is not precisely known an error of ±0.3 kW was assumed.

8.4 Determination of Multibunch Damping Times

8.4.1 Grow-Damp Measurement

As a consequence of a coupled-bunch instability, the electron bunches oscillate in a specific multibunch mode. In order to determine the growth rate of this coupled-bunch mode, the following so-called grow damp measurement scheme is applied.
The entire electron beam is stabilized by the bunch-by-bunch feedback system. At a certain time, the feedback loop is opened and the electron beam starts to oscillate in the multibunch mode with the highest growth rate. From an exponential fit to the oscillation amplitude, the growth rate is obtained. After several milliseconds, the feedback system is switched on again, which re-stabilizes the beam.
In Fig. 53, a typical longitudinal grow-damp measurement is shown. The bunch oscillation of a multibunch train with ∼144 filled buckets was observed for about 25 milliseconds (Fig. 53a). The envelope of the oscillation amplitude was extracted from the raw data as explained in Sect. 5.3.3. From a modal analysis using the FFT algorithm, the mode-resolved beam dynamics was calculated as shown in Sec. 5.3.5 (Fig. 53b).
The measurement shows that multibunch mode 12 is the mode with the highest growth rate. By repeating this measurement for different beam currents, the current-dependence of the multibunch growth rate of mode 12 was determined (Fig. 53c).

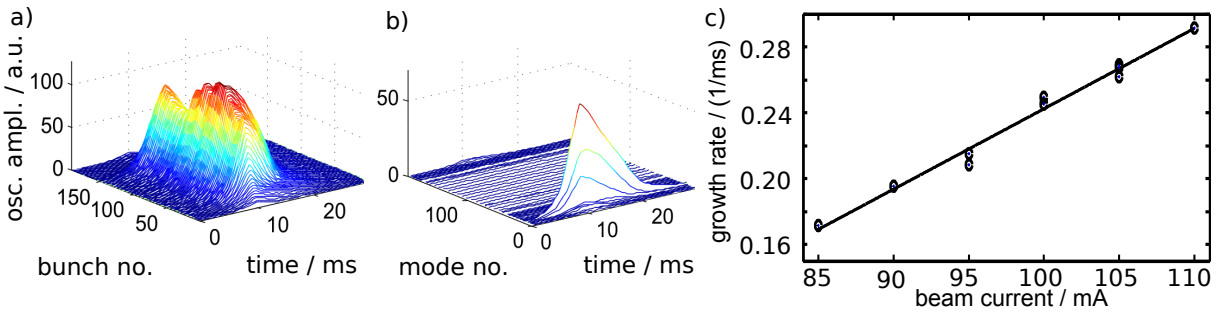

Figure 53: Typical grow-damp measurement in time domain (a), after modal analysis (b) and the linear dependence of the growth rate on the beam current (c).

From the analytical calculations discussed in Sect. 3.3, a linear dependence of the growth rate on the beam current is expected (c.f. Eq. 3.44). A linear fit to the obtained growth rates yields

$$\frac{1}{\tau} = (4.9 \pm 0.2) \cdot 10^{-3} \frac{I}{\mathrm{ms} \cdot \mathrm{mA}} - (0.246 \pm 0.023) \frac{1}{\mathrm{ms}}.$$

From this fit, two machine-specific numbers can be extracted.
The zero crossing indicates the beam current, at which the impedance-driven growth rate equals the natural damping rate, i.e. the total growth rate is zero. From this measurement, the instability threshold was estimated by extrapolation to be $I_{\mathrm{th}} = (50 \pm 6)\,\mathrm{mA}$. The value at zero current reflects the natural damping rate of the machine. It shows a good agreement

(deviation of 5%) with the analytical value of the natural damping rate, given by [26]

$$\frac{1}{\tau_S} \approx \frac{V_S f_0}{E} \approx 0.233 \frac{1}{\mathrm{ms}} \tag{8.3}$$

with the beam energy $E = 1.5\,\mathrm{GeV}$, the revolution frequency $f_0 = 2.6\,\mathrm{MHz}$ and the energy loss per turn $V_S \approx 135\,\mathrm{keV}$. During the measurement, the DELTA wiggler (SAW) was switched off.

8.4.2 Instability Threshold

Besides calculating the instability threshold I_{th} from an extrapolation of the growth rate, it may also be determined directly by observing the spectral component at the synchrotron frequency of the beam spectrum continuously for different beam currents during the injection. This can be automatically performed by using the mode visualization tool described in the appendix A.2.

As a first indication for beam instability, each bunch starts to oscillate with the synchrotron frequency. This results in an increase of the spectral power $P(f_S)$ at the synchrotron frequency in the single-bunch spectrum. The single-bunch spectrum is the FFT of the bunch position data of only one bunch sampled once per revolution. By adding up all single-bunch spectra of all bunches, the resulting spectral power at the synchrotron frequency is a measure for the strength of the beam instability. However, any information of the coupled-bunch mode number is lost in this approach. A modal analysis of the instability threshold will be given afterwards.

In Fig. 54, the spectral power at the synchrotron frequency is plotted against the beam current for two different machine configurations. In the first configuration, the DELTA wiggler (SAW) is switched off, while in the second configuration the SAW is on. The measurement was repeated for several subsequent beam injections showing that the instability threshold increases by more than 20 mA when the SAW is switched on, which will be explained in the following.

The impedance budget, which is driving the longitudinal multibunch instability, is dominated by the higher-order modes of the RF cavity and other resonant structures in the ring and is not changed on purpose. Therefore, the growth rate of the instability should not change either. However, the natural damping rate is increased by introducing an additional insertion device, since the radiation losses are increased. This shifts the instability threshold to higher beam currents. In addition, the measurements show that the instability threshold varies by several mA, which might be explained by a temperature-dependent change of the impedance. In accordance with the previous determination of the instability threshold by extrapolation, the instability threshold without SAW varies between $I_{\mathrm{Th}} = 48\,\mathrm{mA}$ and $I_{\mathrm{Th}} = 56\,\mathrm{mA}$.

So far, only the single-bunch spectrum was used in order to characterize the instability

threshold. Since the total beam spectrum is folded into a frequency band from zero to $f_0/2 = 1.3\,\mathrm{MHz}$, a large spectral component indicates only the existence of a multibunch instability in general, but does not give a hint on which multibunch mode is excited. By calculating the mode spectrum, additional information on the instability threshold can be derived.

In Fig. 54, the mode amplitudes of mode 8 to 20 of the beam are depicted for injection run 4 and run 8 (c.f. Fig. 54). The measurements show two basic results.

First of all, not only one mode is present, but a superposition of modes. Secondly, the mode with the maximum amplitude changes during the injection.

This might be explained by two mechanisms. On the one hand, the impedance of the machine may be slightly changed due to temperature drifts. On the other hand, the filling pattern is changed during the injection, because with each injection cycle of the synchrotron only 8 buckets of the DELTA storage ring are filled. Since the calculation of the mode spectrum is based on the projection on even-fill eigenmodes (EFEM), there is a inherent discrepancy. The beam eigenmode is a superposition of EFEM. If the filling pattern changes, the set of EFEMs is also changed.

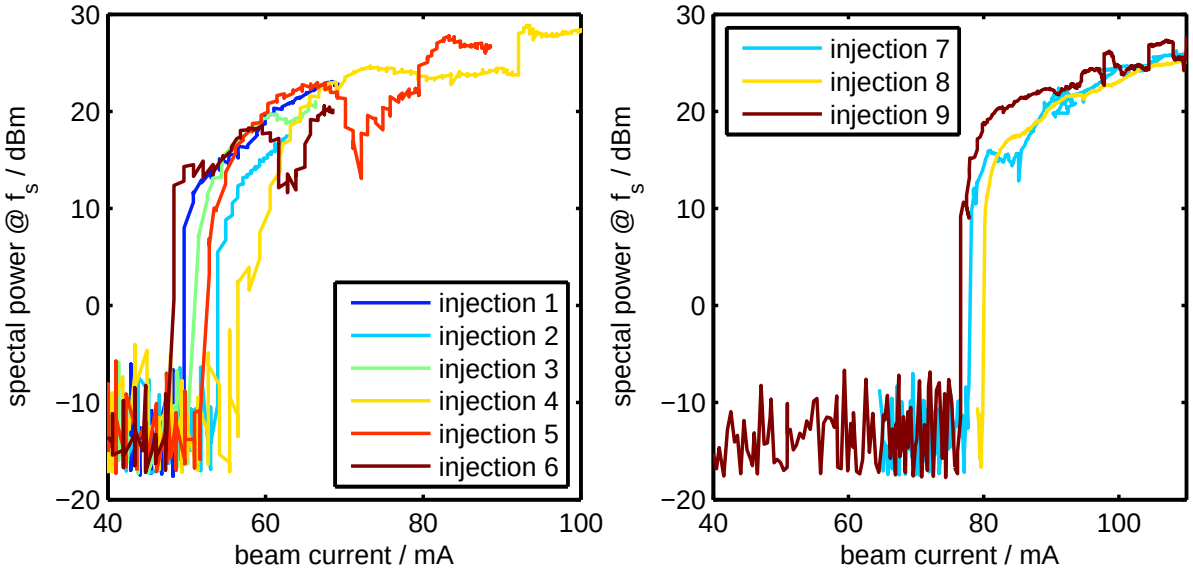

Figure 54: Spectral component at the synchrotron frequency as a function of the beam current for different subsequent injections. When the wiggler is switched on (right) the instability threshold is increased by more than 20 mA.

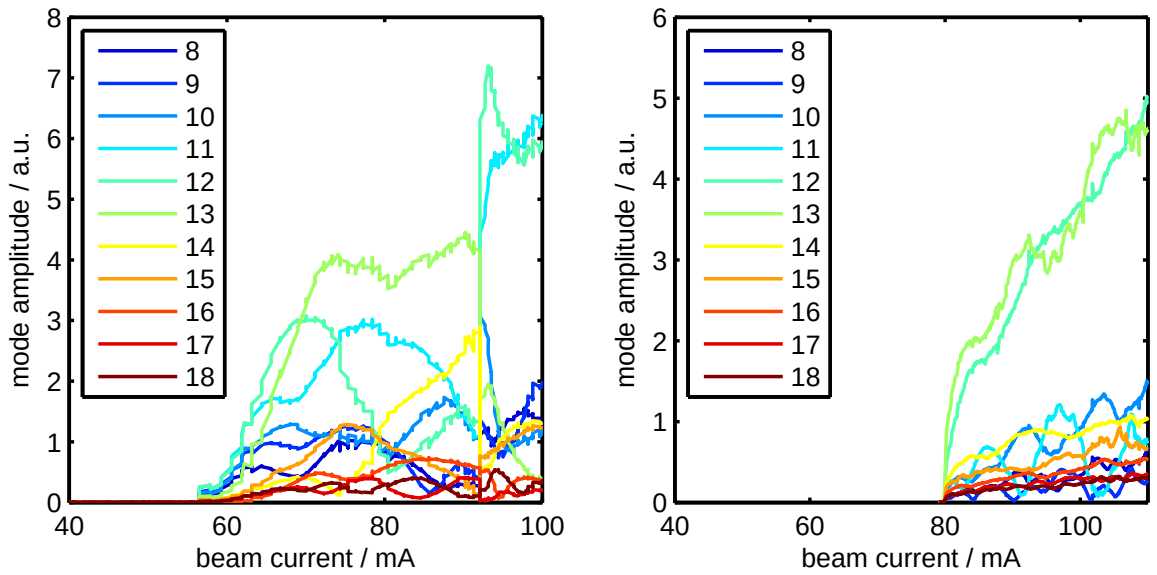

Figure 55: Mode amplitude of multibunch mode 8 to 18 for injection run 4 (see previous figure) with SAW on (left) and injection 8 run (see previous figure) with SAW off (right).

8.4.3 Mode-Selected Damping Times

While the previous measurements allow to determine the natural damping time and the growth rate of the most dominant multibunch mode, the information of all other multibunch modes is not accessible. In order to study all 192 multibunch modes, the internal NCO (drive generator) of the feedback processing units was used to excite one specific multibunch mode by exciting the beam longitudinally with a fixed frequency and amplitude.
By switching off the excitation, the oscillation of the electron beam is damped, since the measurement was performed below the instability threshold of the machine (SAW switched on). One example measurement is shown for mode 20 in Fig. 56. Here, the entire beam is oscillating in the chosen mode. From an exponential fit to the damping transient, the damping rate of the multibunch mode was determined. This measurement was repeated for all multibunch modes.

The damping rates of the modes differ by more than a factor of five. As expected from the previous measurements, mode 12 has the lowest damping rate, since it is the most unstable multibunch mode. The damping rates for a beam current of 59 mA are depicted in Fig. 57. Pairs of modes μ and $h-\mu$, where h is the harmonic number, show a complimentary behavior. While one of them has a higher damping rate than the average value, the corresponding one has a lower damping rate and vice verse. This can be explained by having a look at the

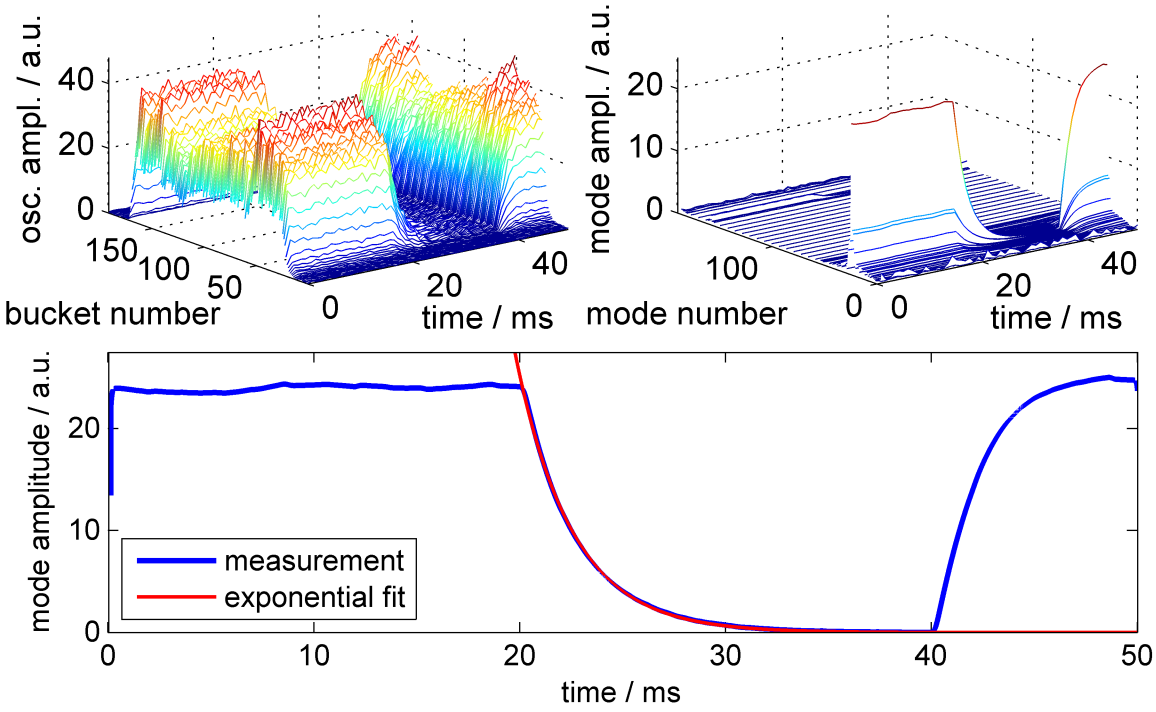

Figure 56: The beam is excited at one specific mode by the internal signal generator of the feedback. The temporal evolution is shown on the bunch-by-bunch basis (top, left) and on the mode-by-mode basis (top, right) while the excitation is temporary switched off. An exponential fit to the amplitude of the previously excited mode (bottom) yields the damping rate.

analytical expression for the multibunch growth rate given by (cf. Sect. 3.3 Eq. 3.44)

$$\frac{1}{\tau_\mu} = \frac{hNe^2\eta}{2\omega_\mathrm{s}ET_0^2} \sum_{p=-\infty}^{\infty} (ph\omega_0 + \mu\omega_0 + \omega_\mathrm{s}) \,\mathrm{Re}\left[Z_\parallel (ph\omega_0 + \mu\omega_0 + \omega_\mathrm{s})\right] \tag{8.4}$$

with the number of electrons in each bunch N, the electron charge e, the slippage factor η, the synchrotron frequency ω_s, the revolution frequency ω_0, the beam energy E , the revolution time T_0 and the longitudinal impedance $Z_\parallel$. For a given narrow-band impedance $Z_\parallel$ from a higher-order cavity mode with a central frequency at about $\omega_\mathrm{RF} + \mu\omega_0$ as an example (see Fig. 58), the sum in Eq. 8.4 reduces to one single summand ($p = 1$) and the growth rate for mode μ is given by

$$\frac{1}{\tau_\mu} = \frac{hNe^2\eta}{2\omega_\mathrm{s}ET_0^2} \underbrace{(h\omega_0 + \mu\omega_0 + \omega_\mathrm{s})}_{>0} \underbrace{\mathrm{Re}\left[Z_\parallel (h\omega_0 + \mu\omega_0 + \omega_\mathrm{s})\right]}_{>0}.$$

Since the real part of the longitudinal impedance is always positive, the HOM-driven growth rate for mode μ is positive as well. Assuming that only one HOM exists, the evaluation of Eq. 8.4 for all the other modes returns zero due to zero impedance, except for mode $h - \mu$.

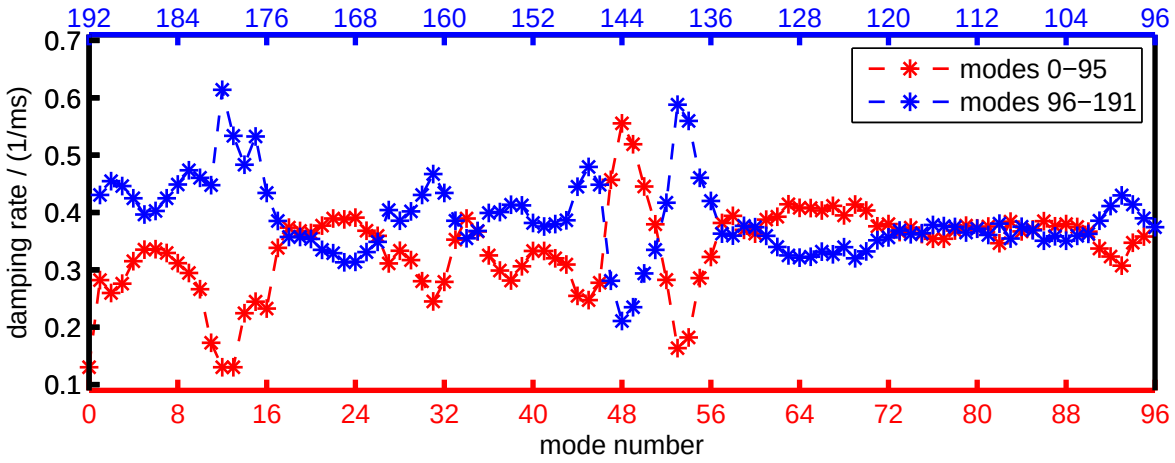

Figure 57: Damping rates of all 192 multibunch modes. To show the corresponding behavior of pairs of modes, the first half of the modes (0-95, red) and the second half of the modes (96,191) are plotted on a common scale.

In that case, the sum reduces again to one summand ($p = -2$) and the growth rate is given by

$$\frac{1}{\tau_{h-\mu}} = \frac{hNe^2\eta}{2\omega_s E T_0^2} \underbrace{(-h\omega_0 - \mu\omega_0 + \omega_s)}_{<0} \underbrace{\mathrm{Re}\left[Z_\parallel\left(-h\omega_0 - \mu\omega_0 + \omega_s\right)\right]}_{>0},$$

which has a negative sign. Besides the different signs of the growth rates of modes μ and mode $h-\mu$, it is important to note that the impedance is sampled at two slightly different frequencies, which have a frequency difference of $\Delta\omega = |h\omega_0 + \mu\omega_0 + \omega_s| - |-h\omega_0 - \mu\omega_0 + \omega_s| = 2{\cdot}\omega_s$. While for higher-order-modes this difference is not relevant, for the fundamental mode zero the impedance is sampled twice, and the difference in both damping and growth rate decides whether the beam is unstable or not. This is well-known as Robinson damping and results in the fact, that the resonance frequency of the fundamental mode should be always slightly lower than its closest revolution harmonic $h \cdot \omega_0$.

At DELTA there are several impedance components, which results in many different damping rates as shown in Fig. 57. Furthermore, all modes have a positive total damping rate, although half of them have a positive HOM-driven growth rate. This results from the fact that the HOM-driven growth rate is overlain by the natural damping rate as discussed in Sect. 8.4.1 and that the measurement was performed below the instability threshold of the machine.

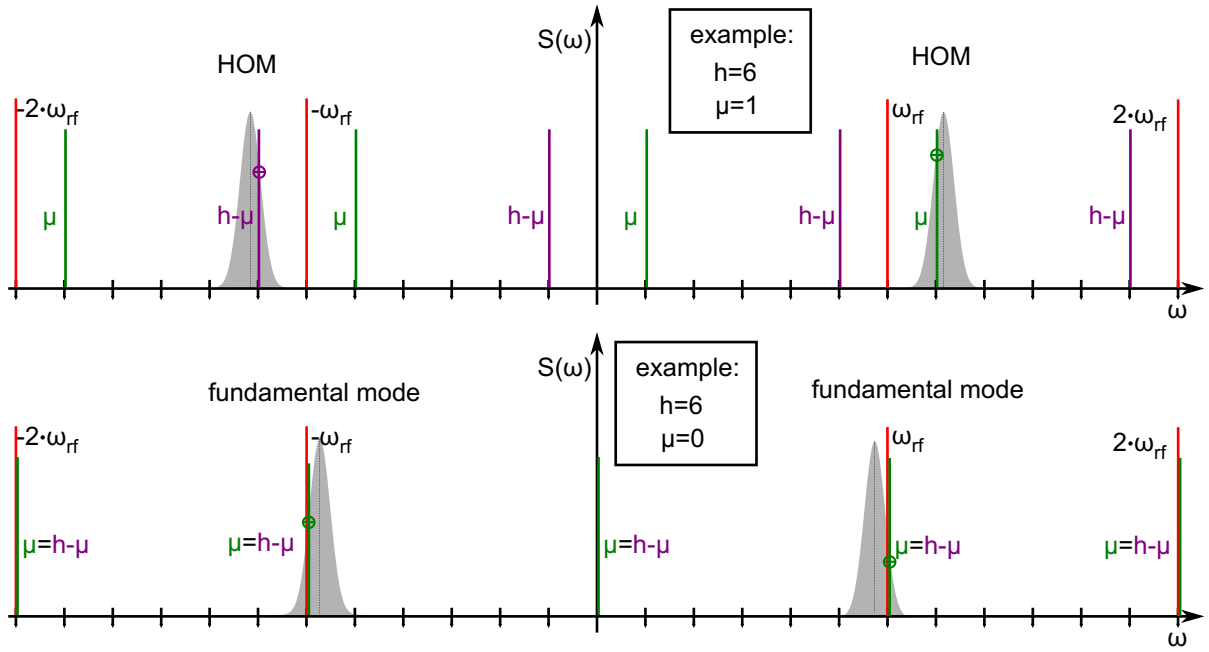

Figure 58: To explain the beam-cavity interaction, relevant spectral components of the frequency spectrum for an example machine with a harmonic number of 6 are shown. For an example HOM (top, gray), the multibunch mode $\mu = 1$ (green) has a positive growth rate, while the corresponding mode $\mu = 5$ (purple) has a negative growth rate. Possible other HOMs influencing the same multibunch modes are neglected in this example. In the case of the fundamental cavity mode (bottom), multibunch mode zero has a negative growth rate and is Robinson-damped.

8.4.4 Dependence on the Beam Current

For a fixed filling pattern, Eq. 8.4 predicts a linear dependence of the growth rates on the number of particles N. Therefore, the previous measurement was repeated for several different beam currents. The damping rates of selected modes with comparatively high and low damping rates are shown as a function of the beam current in Fig. 59. A linear fit to the growth rates of the multibunch modes allows to extrapolate to the growth rate at zero current, which yields to a common value of $1/\tau \approx 0.42\,/\text{ms}$. As expected from Eq. 8.4, the modes with a positive (negative) HOM-driven growth rate show a decrease (increase) of the damping rate with increasing beam current.

The deviations of the growth rates from the linear dependence result from small deviations of the filling pattern from a even fill. The determined damping rate at zero current is about a factor of two higher than the natural damping rate of $1/\tau \approx 0.233\,/\text{ms}$ (cf. Eq. 8.3) This can be explained by the fact that the feedback system is only capable of detecting the center-of-mass motion while the incoherent motion can not be detected. For a very small excitation amplitude as it was e.g. done at the grow-damp measurements described in Sect. 8.4.1 the bunch is not lengthened significantly and the center-of-mass motion reflects the incoherent damping, i.e., the damping of an individual electron, quite well. However, also at

that measurement the calculated damping rate at zero current was slightly larger than the natural damping rate.

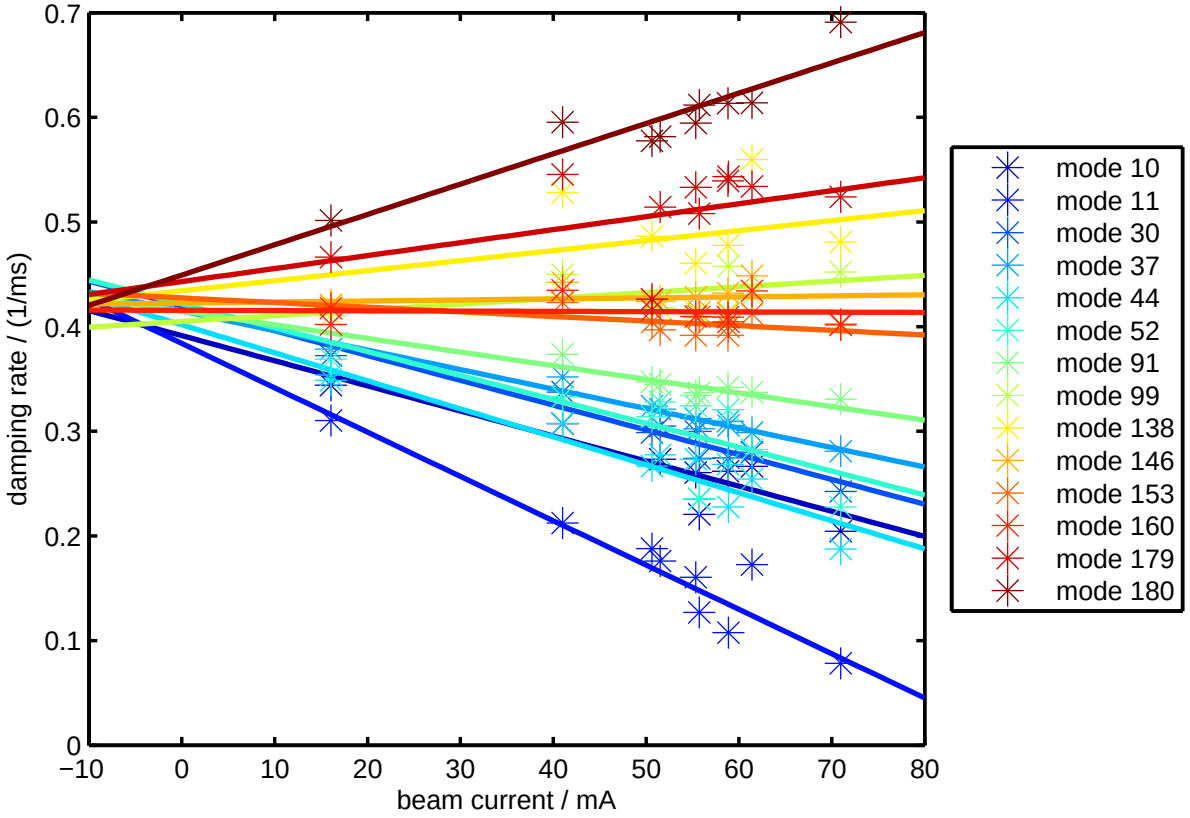

Figure 59: The damping rates of selected multibunch modes as a function of the beam current. Linear fits allow to extrapolate to a common zero-current damping rate.

8.4.5 Comparison with Streak-Camera Data

In order to visualize the different damping rates of the center-of-mass motion versus the incoherent damping rate, streak-camera images were compared to the bunch position data of the bunch-by-bunch feedback.

Figure 60 shows a streak camera image of the electron beam, in which the beam was temporarily excited by positive feedback in a time interval of about 8 ms. Both streak units were in operation. The fast unit was operating in synchroscan mode (cf. Sect. 7.2), showing the bunch length on a time scale of a few hundred picoseconds, while the slow unit performed a single streak over 15 milliseconds. Feedback system and streak camera were triggered by a common clock signal. Due to the slow time scale at the abscissa, the actual bunch oscillation is not resolved but the excitation by positive feedback results in a broadening of the apparent bunch length.

To compare the streak-camera data with the feedback data, the rms width of the bunch length is calculated from the streak-camera image and plotted on the same time scale as the oscillation amplitude of the bunches detected with the feedback system. The relative timing between both curves depicted in the bottom of Fig. 60 is chosen such that the damping of the oscillation starts at the same time. The scaling of the ordinates, although independent, is chosen in a way that the rising edge of the oscillation for both curves coincides. An exponential fit to the falling edges yields a damping rate of 0.58/ms for the streak-camera data and a factor two higher damping rate of 1.16/ms for the feedback data. This shows clearly that the center-of-mass motion is damped faster than the incoherent motion. The effect of the fast damping of the center-of mass was also discussed in Ref. [75] but no comparison with the feedback data was performed. Since active damping of the feedback was used, the absolute value of the damping rates shown in Fig. 60 are higher than those presented in the previous section.

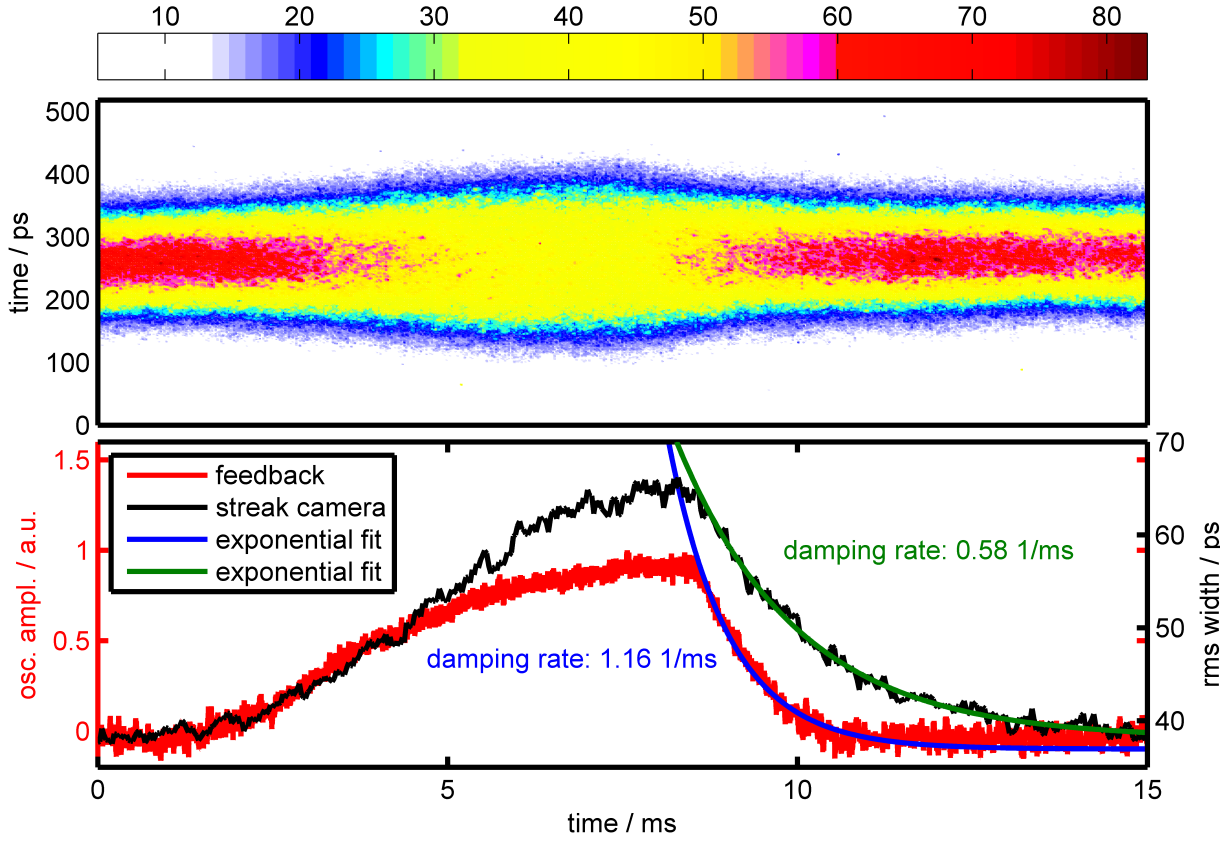

Figure 60: Streak-camera image with color-coded light intensity (top). The lack of light intensity at the center of the image results from the temporal excitation due to positive feedback, which causes an oscillation and bunch lengthening. The rms width of the streak-camera image is determined for every pixel line and is depicted as black curve (bottom). For comparison, the bunch oscillation amplitude detected with the feedback unit is plotted on the same scale (red). Exponential fits (blue and green) allow to compare the damping rates. Streak camera and feedback were triggered by a common clock signal and only one excitation was performed to make sure that the same event is observed.

8.4.6 Saturation Values of Specific Multibunch Modes

For the measurement described in the following, the feedback system is not switched off for a period of time, but is phase-shifted by 180 degrees, i.e. the feedback is actively exciting all bunch oscillations driving them strongly into saturation [76]. Here, saturation means that the oscillation amplitude is not increasing anymore, although the excitation persists. This scheme applied to the beam would result in an oscillation of the most dominant mode 12. To study the other multibunch modes it is necessary to preexcite them by the NCO, as it was done in the previous measurements, so that the positive feedback amplifies the preexcited multibunch mode more than others. Figure 61 shows two example measurements.

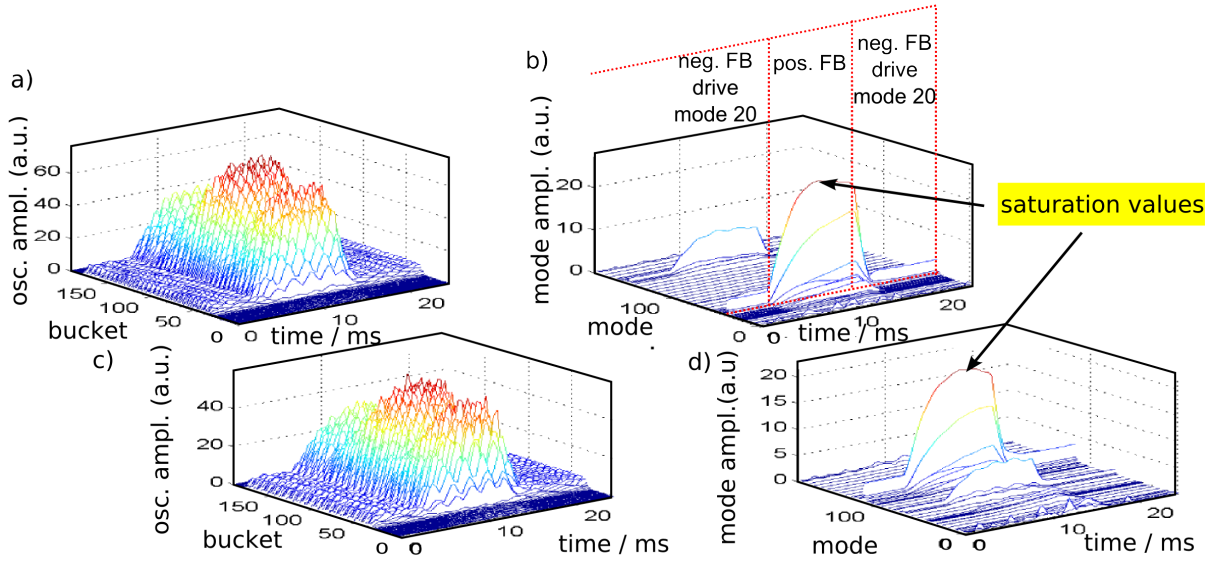

Figure 61: Time evolution of the beam while preexciting multibunch mode 20 (a/b) and 120 (c/d) is displayed on a bunch-by-bunch (a/c) and a mode-by-mode (b/d) basis.

The saturation amplitudes differ from mode to mode. The dependence of the saturation values on the mode number shows two characteristic trends as depicted in Fig. 62. First, they follow a parabola which is centered at mode 95. In addition, there is a small variation similar to the variation of the damping rates as presented in Fig. 57 in Sect. 8.4.3. This can be shown by subtracting a quadratic dependence of the saturation amplitude as shown in Fig. 62 and comparing the result with the mode-selected damping rates. As expected, whenever the saturation amplitude of one mode is high compared to the other modes, the damping rate of this mode is small, since a higher damping rate reduces the maximum oscillation amplitude for a given feedback excitation rate. However, the feedback excitation rate is not fixed over the entire frequency range due to the frequency response of the amplifier and kicker structure. This results in a slight increase of the excitation rate for small frequencies. Therefore, the saturation amplitude of mode 95, which corresponds to the highest frequency in the 250-MHz baseband, has the lowest saturation amplitude.

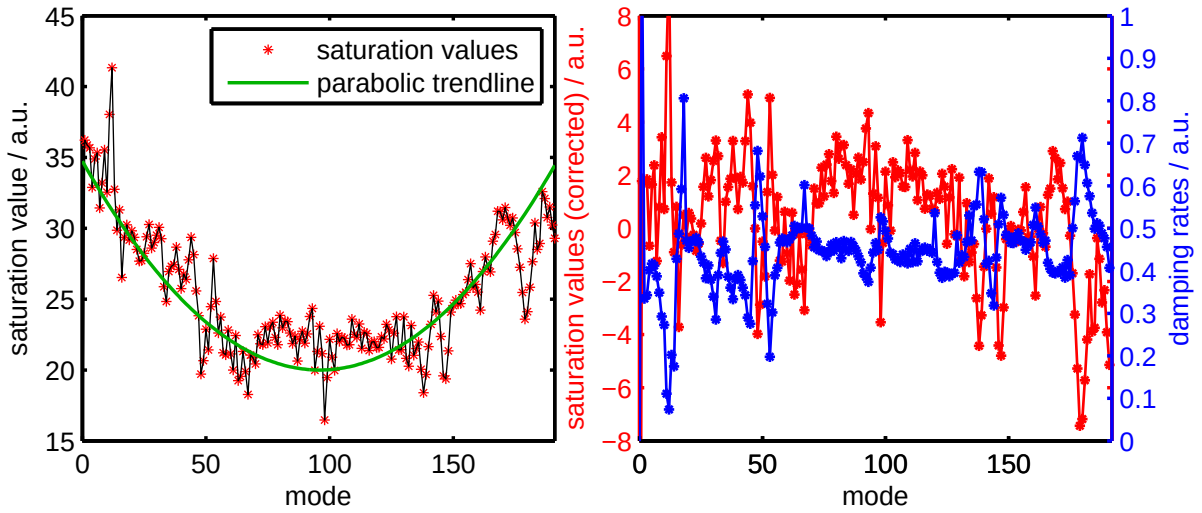

Figure 62: Saturation amplitudes of all multibunch modes and a parabolic trendline (left). The saturation amplitudes after subtraction of the parabolic trendline are plotted together with the damping rates of all modes on a common scale (right).

8.5 Inter-Bunch Coupling

So far, the oscillation of the multibunch train was studied under the influence of the bunch-by-bunch feedback system. The system was used to either temporary excite or suppress the oscillation of all bunches [77].
In this section, a measurement is described, in which only a part of the bunch train is excited by the bunch-by-bunch feedback system. It will be shown that also the bunches which are not affected by the feedback system may be stabilized above the instability threshold of the storage ring if the number of stabilized bunches is large enough. The measurements will be compared with simulations in order to explain the coupling mechanism.

8.5.1 Partial Excitation of the Bunch Train

Figure 63 shows a typical measurement in which only a part of the bunch train is interacting with the feedback system. The measurement is performed above the instability threshold, so that without feedback all bunches would oscillate longitudinally. At the beginning, bunches 55 to 165 are stabilized by negative feedback until the feedback output is shifted by 180° in phase causing an excitation of these bunches. This positive feedback is enabled for 2 ms. After the excitation period, the bunch oscillation is damped again by negative feedback. Bunches 20 to 54 are not damped or excited by the feedback system at all. Since buckets 1 to 19 and 166 to 192 are empty, they show no signal.
Although bunches 20 to 55 are not under feedback control, they show an increase of the oscillation amplitude several milliseconds after the excitation. In this example, the oscillation of these bunches is damped afterwards. The damping results from the fact that most other bunches are stabilized by the feedback system.

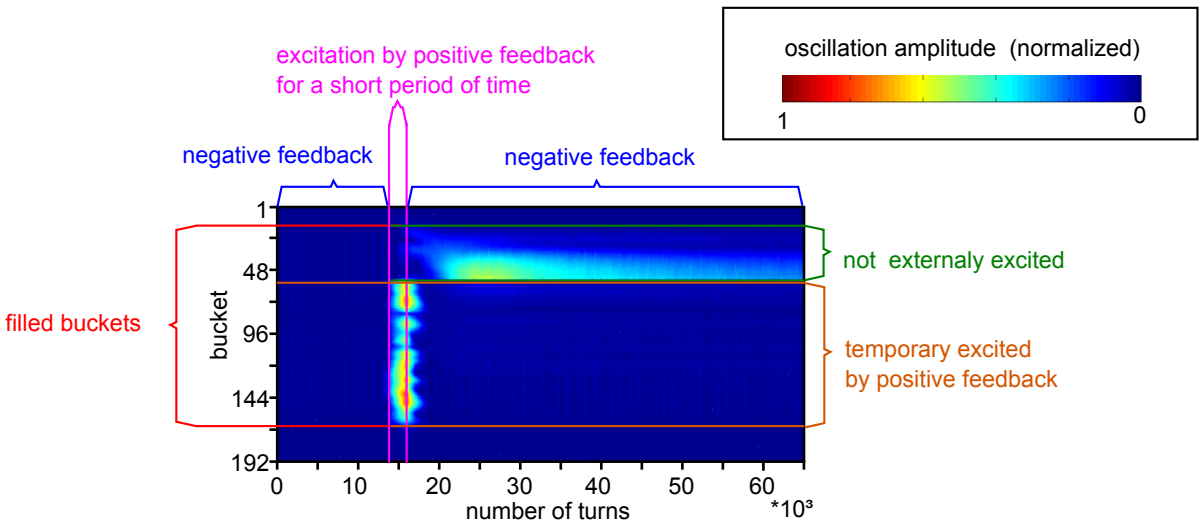

Figure 63: Typical measurement of the oscillation amplitude of all bunches while the bunch train is partially and temporarily excited. The colored lines indicate which bunches are excited and are explained in the figure.

In order to show this effect, in Fig. 64, the measurement is repeated with varying number of bunches which are under feedback control. When only a small number of bunches is not affected by the feedback system at all, the bunches are initially stable but start to oscillate for a small period of time due to coupling between them and the excited bunches. By reducing the number of excited bunches even more, the oscillation amplitude of the non-excited bunches is increased. Eventually, all bunches which are not affected by the feedback are unstable even before the excitation, since the measurement is performed above the instability threshold. In addition, it is observed that the maximum oscillation of the subsequent bunches is shifted by several milliseconds depending strongly on the bunch position relative to the excited bunch train.
In a second measurement, shown in Fig. 65, not the bunches at the head of the bunch train are under feedback control, but the bunches at the tail of the bunch train. Again, there is a certain number of buckets which must be stabilized in order to observe only a temporary oscillation of the non-affected bunches at the head of the bunch train.
Again, this measurement shows that the delay when the non-excited bunches show their maximum oscillation amplitude depends on the position relative to the excited bunch train.

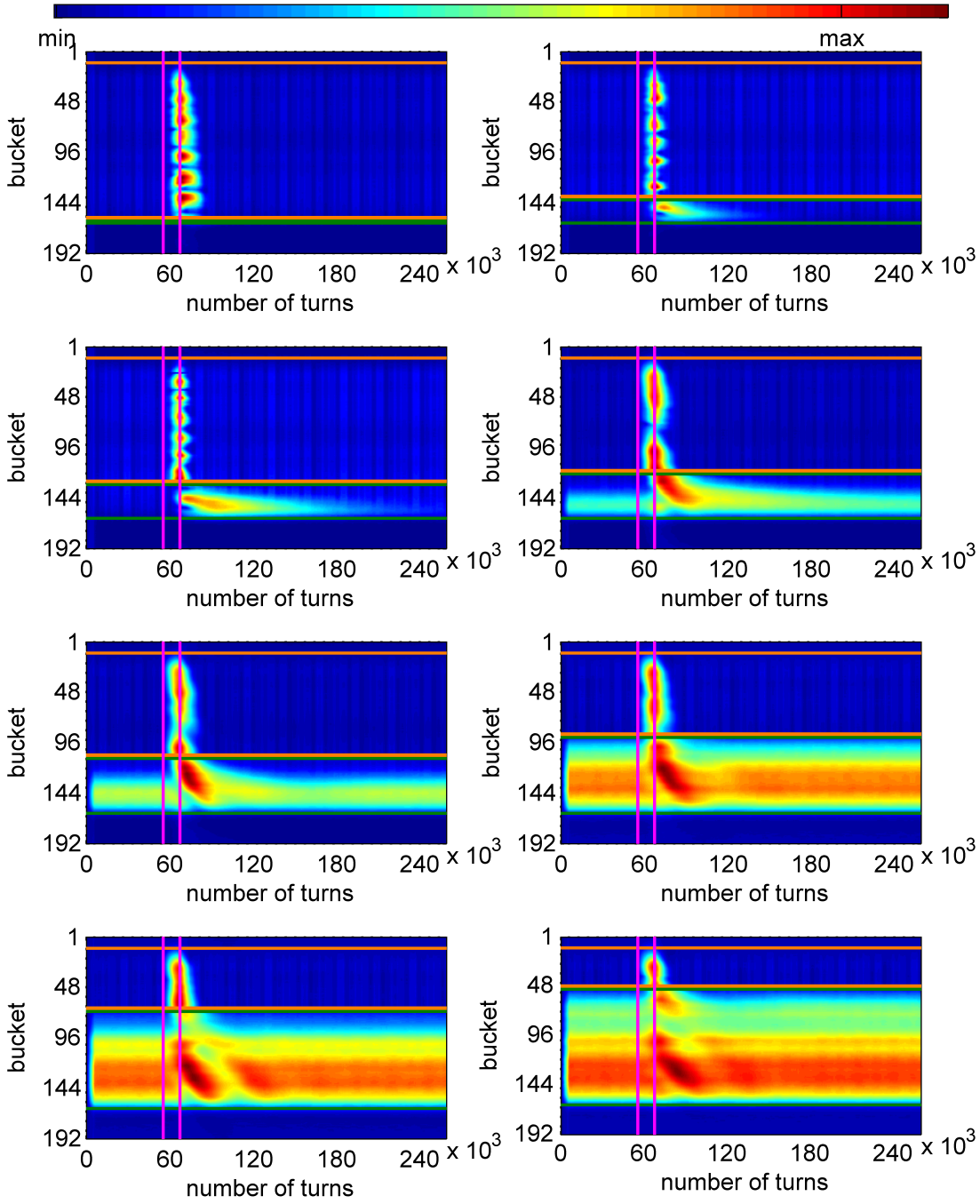

Figure 64: The feedback system excites and damps only the indicated buckets at head of the multibunch train (green lines). The excitation by positive feedback is limited to the indicated short time interval (purple lines). Buckets 1 to 19 and 166 to 192 are not filled with electrons and, therefore, show no signal.

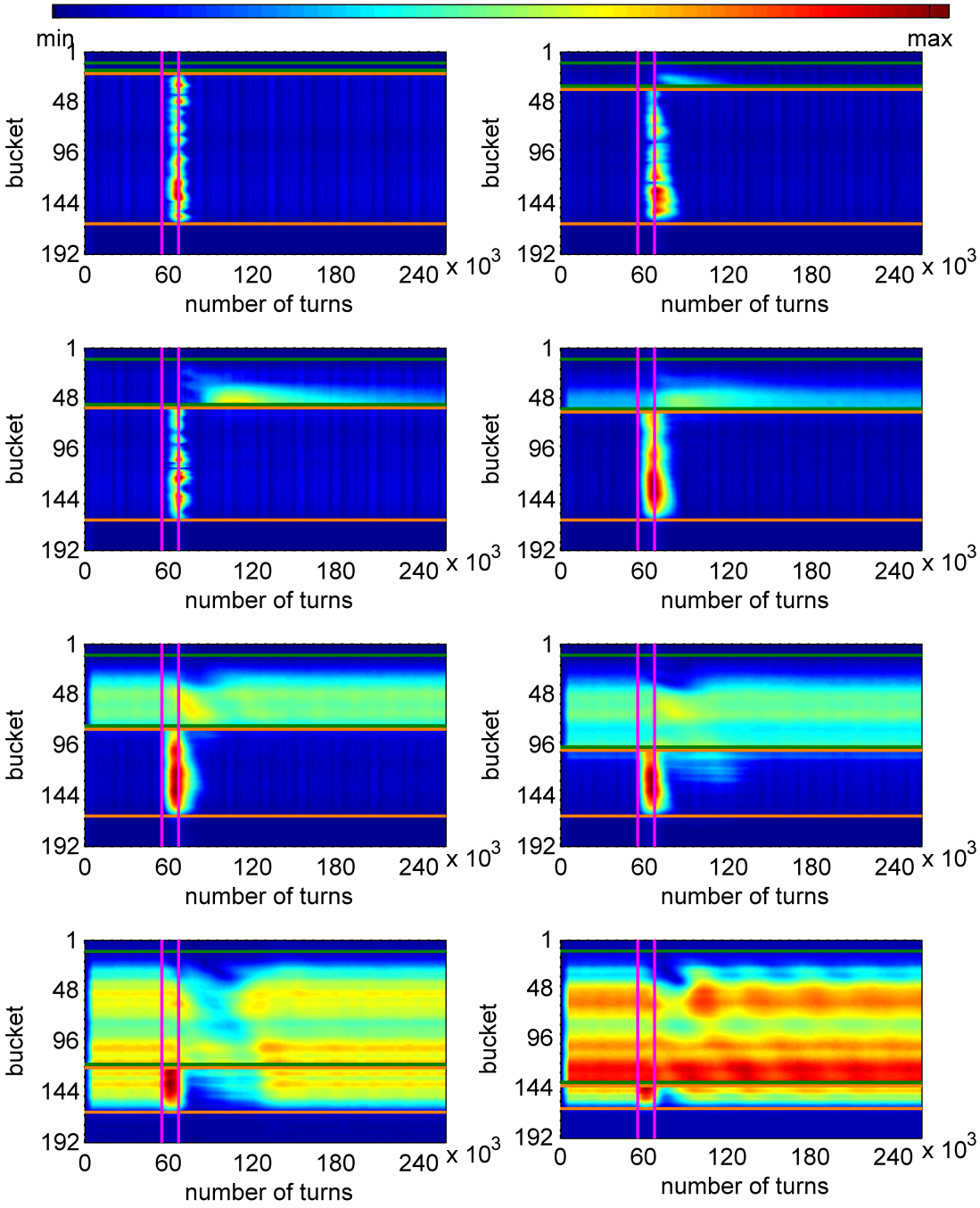

Figure 65: The feedback system excites and damps only the indicated buckets at the tail of the multibunch train (green lines). The excitation by positive feedback is limited to a short time interval (purple lines). Buckets 1 to 16 and 168 to 192 are not filled with electrons and, therefore, show no signal.

8.5.2 Comparison with Simulation Results

In order to understand the coupling mechanism between the excited and non excited bunches, the simulation tool presented in Sect. 5 is used to simulate the coupling between the bunches. Since calculations of the longitudinal impedance (e.g. [20, 14, 78]) of the DELTA storage ring are not able to reproduce the experimentally observed mode spectrum, a different simulation approach is necessary. An impedance pattern was created based on the measurement of the natural damping times of the beam presented in Fig. 57 in Sect. 8.4.3. For each multibunch mode with a damping rate which significantly deviates from the mean damping rate, a narrowband impedance is assumed. All impedances are assumed to have the same quality factor of $Q = 6.6 \cdot 10^4$ and a shunt impedance in the interval of $R \in [3.5 \cdot 10^4, 3.5 \cdot 10^5]$. The values are oriented to higher order modes of the DELTA cavity described in [19]. The particular shunt impedance of each narrow-band impedance is chosen depending on the measured damping rate of the multibunch mode. A high damping rate corresponds to a low shunt impedance and vice verse. The center frequencies of the narrow-band impedances are set to

$$f = 5 \cdot f_{\mathrm{RF}} + n \cdot f_0 + \Delta f$$

with a constant frequency detuning of $\Delta f = 213.5\,\mathrm{kHz}$ and the corresponding multibunch mode number n. The frequency detuning is necessary to avoid resonances. It is important to note, that the narrow-band impedances are only one possible solution and an other set of narrow-band impedances could result to the same damping rates. However, with impedance pattern created this way, the simulation is able to reproduce the damping rates which were experimentally observed. The simulated damping rates of all modes are shown in Fig. 66. To obtain them, the simulation was performed as follows. The beam was temporarily excited by a fixed frequency corresponding to the mode under investigation. Then, the excitation was switched off and the damping rate was obtained by an exponential fit to the oscillation amplitude. This was repeated for all 192 multibunch modes.

Based on this impedance pattern, the partial excitation of bunches was simulated. Figure 67 compares one measurement with a simulation, as an example. In addition, Fig. 68, shows simulation of the partial excitation above the instability threshold for a different number of bunches under feedback control. By reducing the number of bunches which are under feedback control, the non-affected bunches get more and more unstable, as it was observed in the measurement. The non excited bunches show a delayed response on the excitation of the bunches under feedback control.

Since the simulation is able to reproduce the coupling of the bunches which was experimentally observed, it is likely that this coupling due to narrow-band impedances is either driven by the accelerating cavity itself or other resonant structures in the ring.

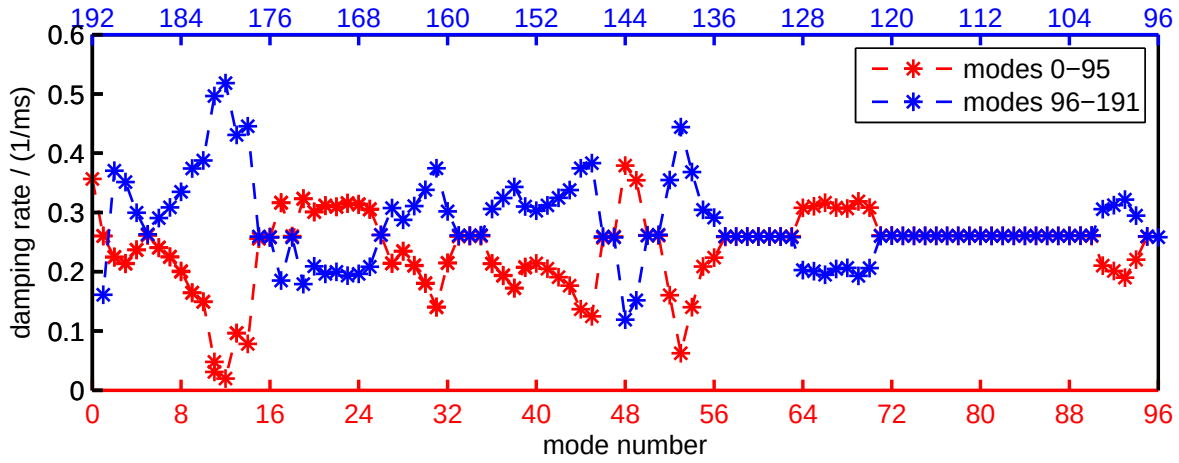

Figure 66: Simulated damping rates of all 192 multibunch modes. The first half of the modes (0-95, red) and the second half of the modes (96-191, blue) are plotted on a common scale.

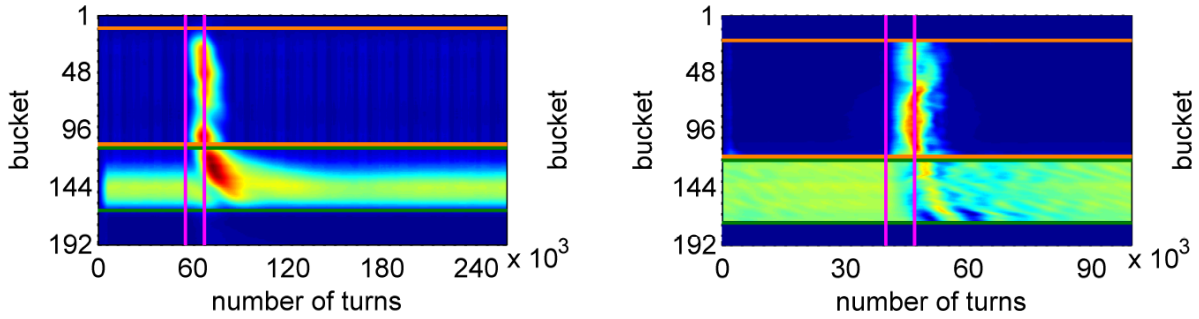

Figure 67: Measurement (left) and simulation (right) of the partial excitation of the bunch train above the instability threshold. The feedback system excites and damps only the indicated buckets (green lines). The excitation is limited to a small time interval (purple lines). The bunches that are not under feedback control show a delayed response on the excitation depending on the distance of the bunch from the bunch train.

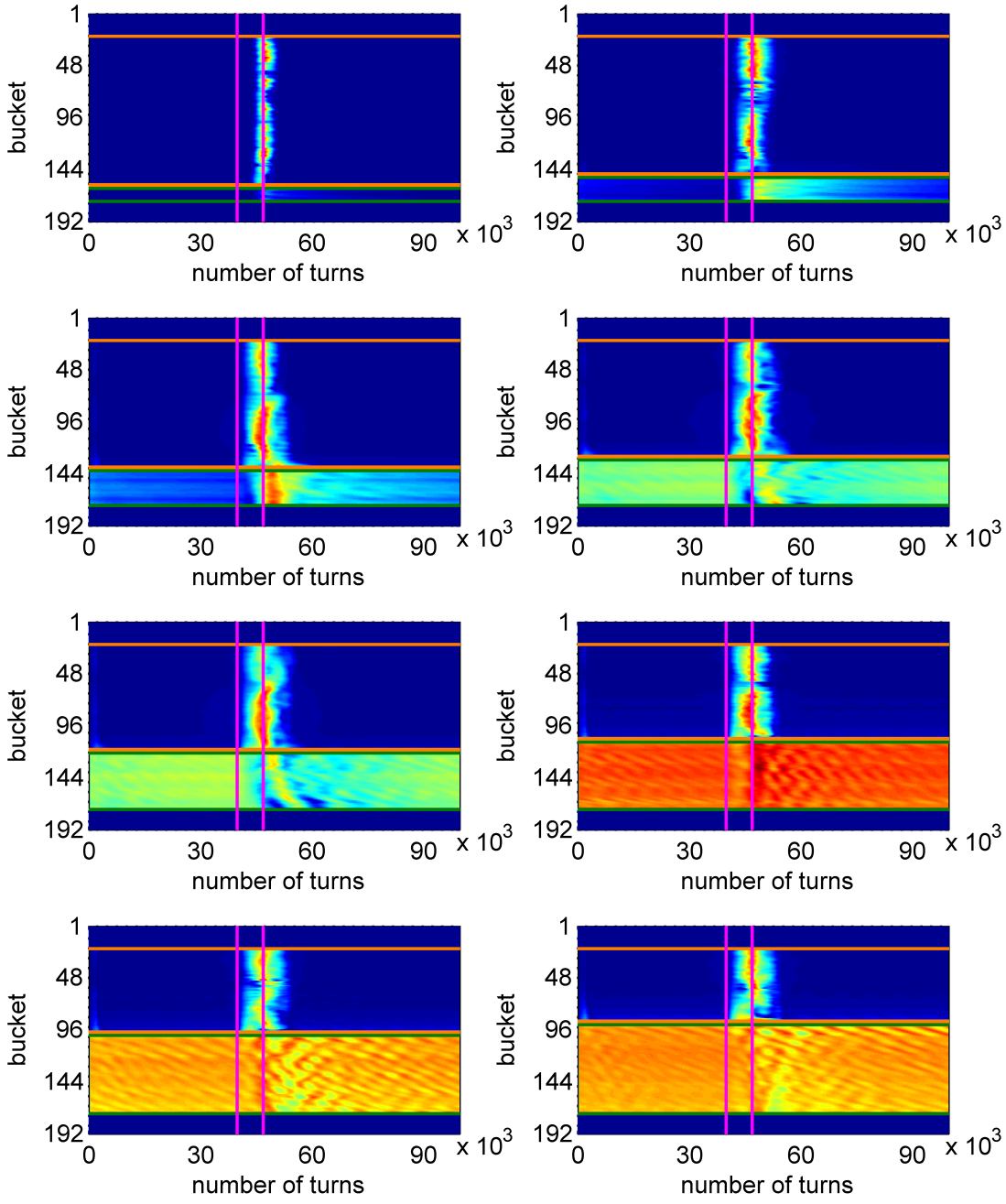

Figure 68: Simulation of the partial excitation of the bunch train above the instability threshold. The feedback system excites and damps only the indicated buckets (green lines). The excitation is limited to a small time interval (purple lines). Buckets 1 to 20 and 172 to 192 are not filled with electrons and, therefore, show no signal.

8.6 Investigation of Single-Bunch Instabilities

In addition to the analysis of coupled-bunch instabilities in multibunch mode, single-bunch instabilities have also been investigated at the DELTA electron storage ring.
In the past years, it was observed that the single-bunch injection is sometimes limited to a certain beam current, which is correlated to the settings of the sextupole magnets. Since the sextupole magnets influence the chromaticity of the storage ring, the chromaticity was changed on purpose to investigate the influence on single-bunch instabilities and will be discussed in the following, while the injection process will be discussed in Sect. 9.2.3.

8.6.1 Dependence of Single-Bunch Instabilities on the Chromaticity

The chromaticity of the storage ring was changed in a dedicated measurement while observing the beam dynamics with the bunch-by-bunch feedback system. In order to change the chromaticity, the current of a part of the sextupole magnets was varied. The chromaticity was measured by changing the RF frequency of the DELTA cavity. The frequency variation forces the electron beam on a dispersive orbit with an energy deviation of [26, 25]

$$\frac{\Delta E}{E} = \frac{1}{\alpha}\frac{\Delta L}{L}. \tag{8.5}$$

With the circumference L and the path difference ΔL, this is the definition of the momentum compaction factor α which has a value of $5 \cdot 10^{-3}$ [55].
Since the circumference of the electron orbit is an integer multiple of the RF wavelength, the relative path length difference is equivalent to a change in the RF frequency

$$\frac{\Delta L}{L} = -\frac{\Delta f_{\mathrm{RF}}}{f_{\mathrm{RF}}}. \tag{8.6}$$

The chromaticity is defined as the change in betatron tune per relative energy deviation

$$\xi_{x,y} = \frac{\Delta Q_{x,y}}{\Delta E/E}. \tag{8.7}$$

Inserting Eq. 8.5 and Eq. 8.6 into Eq. 8.7 yields

$$\Delta Q_{x,y} = -\xi \frac{1}{\alpha \cdot f_{\mathrm{RF}}} \cdot \Delta f_{\mathrm{RF}} \tag{8.8}$$

By measuring the change in betatron tune in relation to the change in RF frequency, the chromaticity is determined according to

$$\xi = -\alpha \cdot f_{\mathrm{RF}} \cdot \frac{dQ_{x,y}}{df_{\mathrm{RF}}}. \tag{8.9}$$

As an example, one chromaticity measurement is shown in Fig. 69.

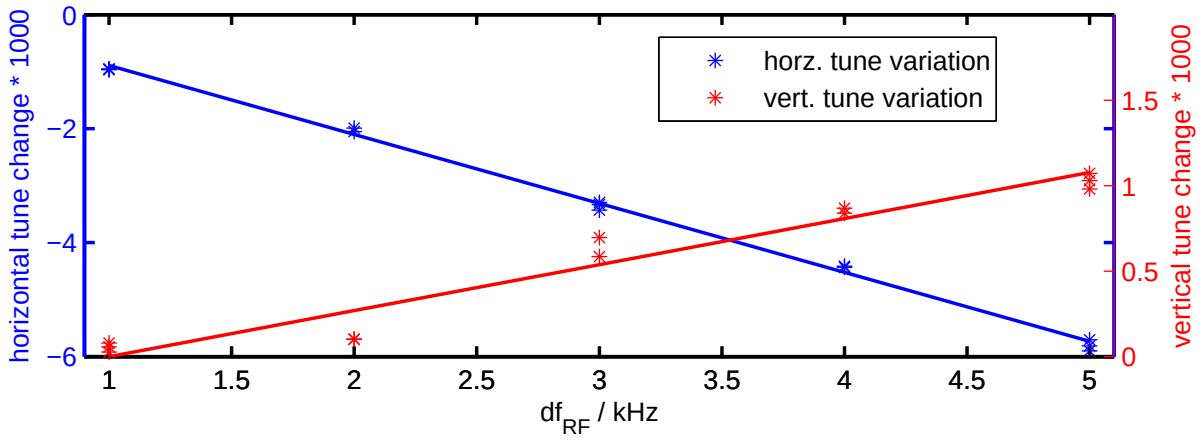

Figure 69: Horizontal and vertical tune variation by changing the RF frequency. The solid lines are linear fits to the data points, from which the chromaticity can be calculated. In this measurement, the horizontal chromaticity is $\xi_x = 3.02$, while the vertical chromaticity is $\xi_y = -0.67$.

In standard operation, the chromaticities at DELTA have slightly positive values of $\xi_x \approx 3$ and $\xi_y \approx 2$. By reducing the sextupole current of particular sextupoles, the vertical chromaticity becomes negative, while the horizontal chromaticity increases. The negative vertical chromaticity gives rise to a vertical oscillation of the single bunch (c.f. Fig. 70), which shows a periodic beating.

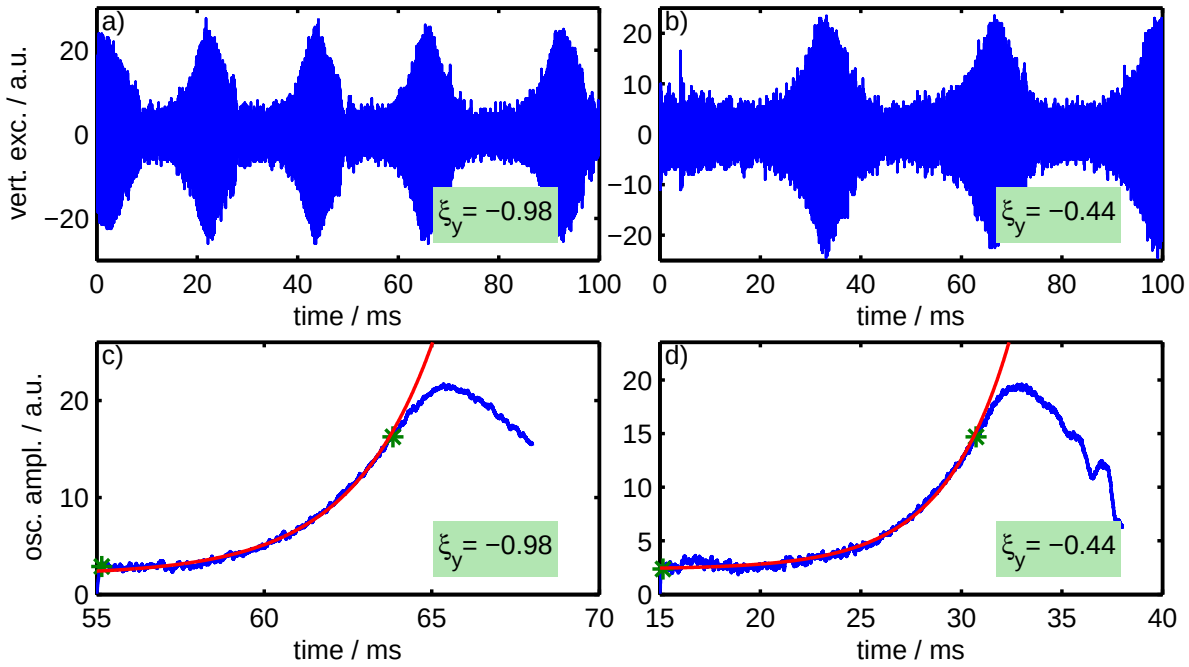

Figure 70: Vertical oscillation of a single bunch plotted in time domain for two different vertical chromaticities (a/b). The signal was high-pass filtered to suppress slow orbit fluctuations and the DC offset. An exponential fit to the envelope of the oscillation within the green marks yields the growth rate (c/d). [79]

The oscillation amplitude increases exponentially to a certain threshold and decreases afterwards due to an amplitude-dependent tune change. The growth rate of the oscillation shows a linear dependence on the chromaticity

$$\frac{1}{\tau} = -\xi_y.$$

The beating periodicity of the bunch oscillation increases with larger growth rate, since the saturation level is reached earlier.

The linear dependence of the observed single-bunch growth rate on the chromaticity suggests that the oscillation is driven by a head-tail instability. As shown in Sect. 3.4, the head-tail mode zero has a positive growth rate for negative chromaticity and shows the same linear current-dependence as observed in this measurement. Since head-tail mode zero corresponds to a center-of-mass motion of the electron bunch, this can be detected with the bunch-by-bunch feedback system.

In order to support the assumption that the instability is driven by a head tail instability, the growth rate of head-tail mode zero is calculated analytically using the equation (cf. Sect. 3.4 Eq. 3.53)

$$\frac{1}{\tau_m} = -\frac{\sqrt{2}C_m}{\pi^{5/2}} \frac{r_0 c}{\sqrt{\mu_0 \sigma_c}} \frac{N_B \xi \sqrt{\hat{z}}}{\eta \gamma b^3 \nu_\beta}$$

with the mode-dependent correction factor C_m which is given by

$$C_m = \left(\int_0^{\frac{\pi}{2}} \sqrt{\sin(x)} dx \right) \cdot \left(\int_0^{\pi} \cos(m\psi) \sqrt{\sin\left(\frac{\psi}{2}\right)} d\psi \right).$$

The quantities and their values used for the calculation are listed in Tab. 4.

Table 4: Parameters used to calculate the growth rate of head-tail mode zero.

parameter	symbol	value
velocity of light	c	$299792458\,\mathrm{m/s}$
classical electron radius	r_0	$2.818 \cdot 10^{-15}\,\mathrm{m}$
permeability of free space	μ_0	$4\pi \cdot 10^{-7}\,\mathrm{N/A^2}$
conductivity of vacuum chamber	σ_c	$1.4 \cdot 10^6\,\mathrm{S/m}$
vacuum chamber half-height	b	$2 \cdot 10^{-2}\,\mathrm{m}$
number of electrons	N_B	$3.6 \cdot 10^{10} \hat{=} 15\,\mathrm{mA}$
Lorentz factor	γ	2930
chromaticity	ξ	-1
slippage factor $\approx$ momentum-compaction factor	η	$5 \cdot 10^{-3}$
vertical fractional betatron tune	ν_β	0.286
mode-dependent correction factor	J_m	$J_0 = 2.9,\ J_1 = -0.57$
rms bunch length	$\hat{z}$	$3.6 \cdot 10^{-11}\,\mathrm{s}$

For a chromaticity of $\xi = -1$, this results in a growth rate of

$$\frac{1}{\tau_0} = 0.961 \, \frac{1}{\mathrm{ms}},$$

which is of the same order of magnitude as observed. The differences to the observed growth rate may be caused by the simplifying assumptions made for the analytical expression, such as a constant wake function, and by the fact that the measured growth rates are reduced by other damping mechanism like radiation damping or Landau damping which are not included in the analytical expression. The observed damping rates are depicted in Fig. 71.

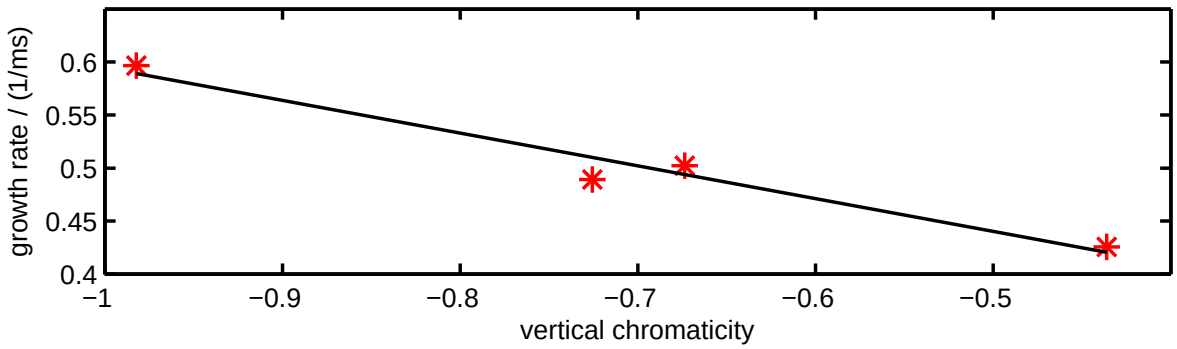

Figure 71: Measured vertical growth rate for different values of the vertical chromaticity (red) and a linear trend line (black).[79]

9 Beam Dynamics Studies

9.1 Beam Stabilization for CHG Operation

At the DELTA short-pulse facility, a femtosecond laser-pulse interacts with one electron bunch in order to generate coherent and short pulses in the VUV and THz regime (c.f. Sect. 6.2). The intensity of the coherent light pulses depends quadratically on the involved number of electrons. The electron bunch has a Gaussian charge distribution with a full width at half maximum (FWHM) of 100 ps. It is necessary to temporarily and spatially overlap the short laser pulse ($\tau_{\mathrm{FWHM}} \approx$50 fs) with the center part of the electron bunch in order to maximize the number of electrons in the interaction area and thus the light pulse intensity.
These coherent harmonic generation (CHG) measurements are usually performed with only one high-current single bunch. By observing the visible part of the synchrotron radiation of that electron bunch and the laser pulse by a fast photo diode, the temporal synchronization is achieved on a 1-ns timescale. For a fine tuning of the temporal overlap, a streak camera (c.f. Sect. 7.2) is used and synchronization can be achieved on a 10 ps timescale. For the spatial overlap, the position of the visible synchrotron radiation of the electron bunch and of the laser pulse is observed on a screen by a camera. By centering both light spots, the overlap is established, and the electron bunch starts to emit coherent VUV and THz radiation. By maximizing the THz radiation with an InSb hot-electron bolometer, the spatial and temporal overlap is further optimized.
While the temporal jitter of the laser pulse is in the fs regime and therefore negligible, a longitudinal oscillation of the electron bunch on the picosecond scale can dramatically decrease the intensity of the emitted VUV and THz radiation as sketched in Fig. 72.

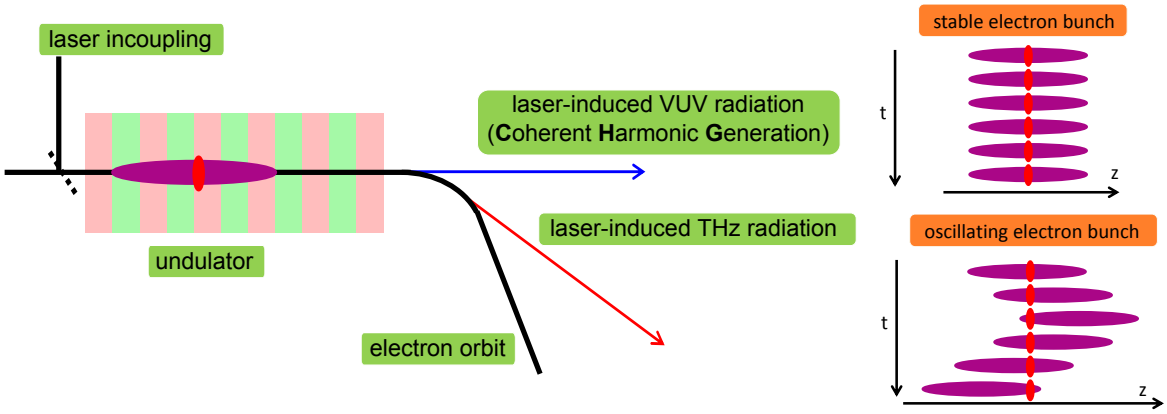

Figure 72: Sketch of the temporal overlap between the laser pulse (red) and the electron bunch (purple) in the undulator. In case of no oscillation of the electron bunch (top, right), the number of electrons in the interaction area is constant and so is the THz and VUV intensity. In case of a strong bunch oscillation, the number of electrons in the interaction area differs for each laser shot. (bottom, right).

In single-bunch operation, the CHG measurements do not suffer from these longitudinal oscillation since the electron bunch is stable up to a beam current of 25 mA. However, the situation changes when CHG measurements are performed in hybrid mode with 3/4 of the buckets filled with bunches up to 1 mA, while one bucket is filled with a high-current bunch of up to 20 mA.
In the following, the need for a hybrid mode operation at DELTA is motivated and the improvements of the CHG intensity due to the bunch stabilization by the bunch-by-bunch feedback system are shown.

9.1.1 Hybrid Mode

A hybrid filling pattern allows to operate the short-pulse facility in standard user operation of the storage ring, since it combines the needs of different beamlines. While for the CHG and THz beamlines one single bunch with high current is necessary, the other beamlines request a high total beam current and a high beam lifetime, which is achieved by distributing the beam current to many buckets. Due to the multibunch filling, all bunches couple to each other by wake fields, which give rise to a strong oscillation of the single bunch. With each laser shot, a different part of the electron bunch interacts with the laser pulse, which on average decreases the CHG and THz radiation intensity.
A complete stabilization of the bunch train with the bunch-by-bunch feedback system results in an increase of the laser-induced signals. However, the beam lifetime decreases by up to one hour when the bunch-by-bunch feedback stabilizes the entire beam as shown in Fig 73.

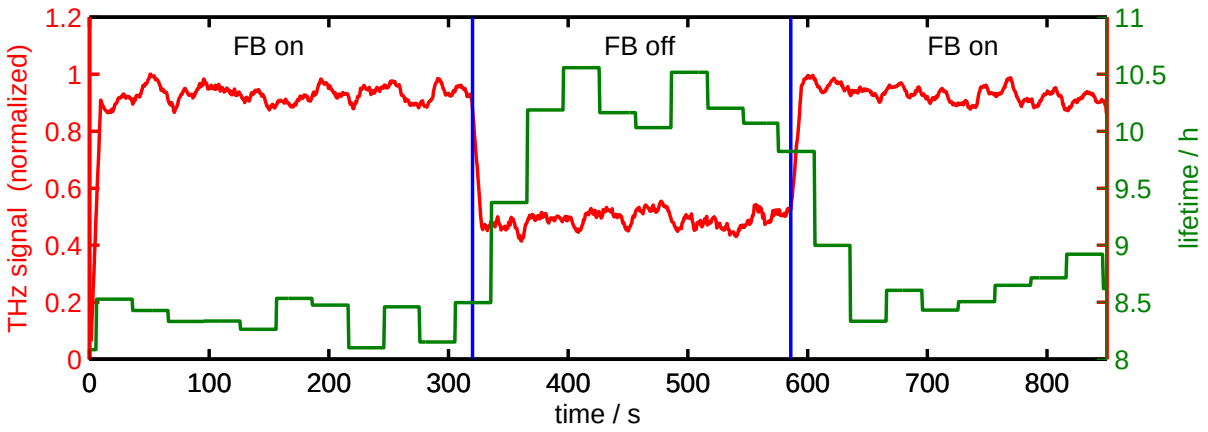

Figure 73: Laser-induced THz signal of the high-current single bunch (red). When the bunch-by-bunch feedback system is switched off, the signal amplitude decreased but the beam lifetime (green) increased by up to 1 hour.

If only the high-current single bunch is under feedback control, the excitation due to wake fields can be compensated, although the multibunch train is unstable. Furthermore, the beam lifetime is not decreased.

To study the coupling between the multibunch train and the high-current single bunch, the longitudinal bunch-by-bunch feedback unit was used to stabilize dedicated buckets of the multibunch train. While buckets 20 to 160 were filled with approximately 0.8 mA, bucket 187 was filled with 7 mA (c.f. Fig. 74). The laser was synchronized to the high-current single bunch.

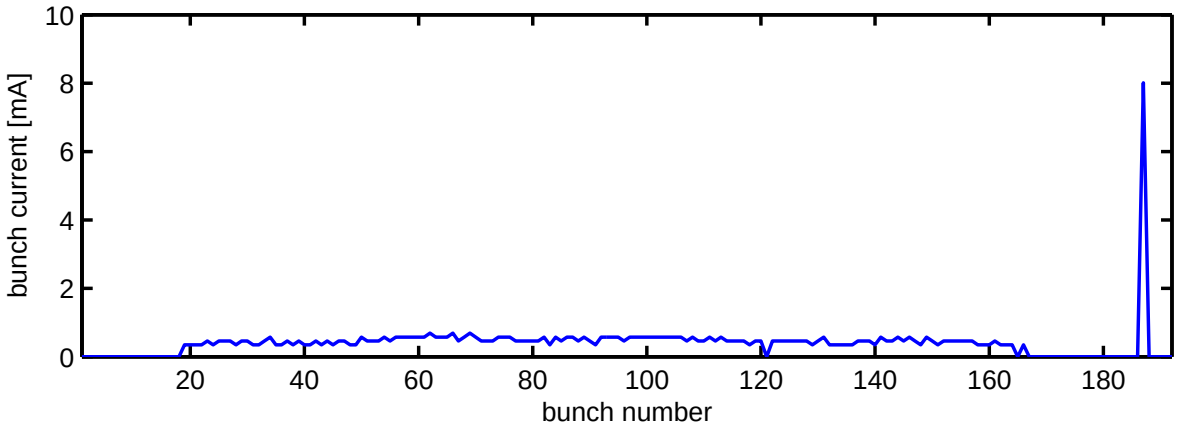

Figure 74: Hybrid filling pattern, in which the high-current single bunch (bucket 187) was used for the laser-electron interaction.

At the beginning of the measurement, the bunch-by-bunch feedback system was used to stabilize buckets 1 to 181 so that the single bunch was not included. This resulted instantly in a stabilization of the single bunch since there was no collective excitation by the multibunch train. The oscillation amplitude of the single bunch was extracted from the processing units of the bunch-by-bunch feedback system. During the measurement, the number of buckets which were stabilized by the feedback was reduced. First, the reduction was started from the head of the multibunch train, then the reduction of stabilized buckets was started from the tail of the train. In both cases there was a certain threshold, at which the single bunch starts to oscillate. Simultaneously, the THz and CHG signal was decreased. By further reducing the number of stabilized buckets, the laser-induced signals decreased proportional to an increase of the oscillation amplitude. Without stabilization, the signals reached only 50% of the initial amplitude. In Fig. 75, the respective scans are shown. In standard user operation, the beam lifetime is increased by an RF-phase modulation which will be explained in the next section. This modulation corrupts the laser-electron interaction and decreases the signal intensity. In order to operate the short-pulse facility in hybrid mode and with enabled RF-phase modulation, the feedback system can be used to recover the initial signal amplitude.

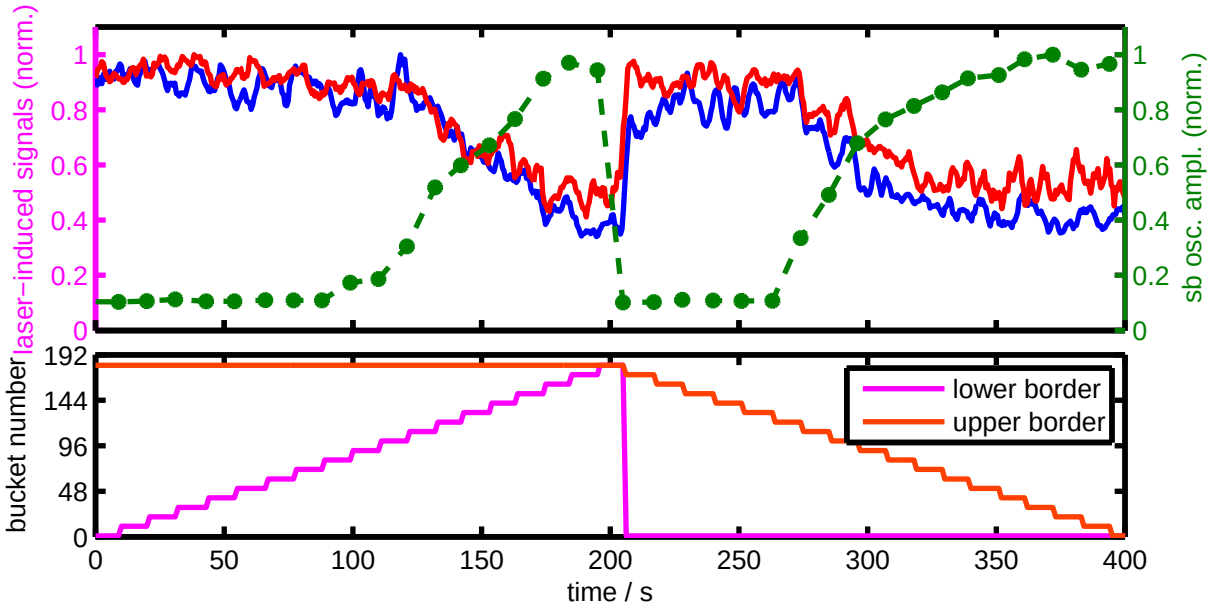

Figure 75: The laser-induced THz (red) and CHG (blue) signals are plotted versus time while changing the number buckets stabilized by the bunch-by-bunch feedback system. The decrease of the signals is correlated to the oscillation amplitude of the single bunch (green), which was detected by the feedback system. In the bottom plot, the upper and lower limits of the interval of stabilized buckets are indicated by the orange and blue lines.

9.1.2 RF-Phase Modulation

In standard user operation at DELTA, the RF signal from the master oscillator is phase-modulated [21]. To do so, an electronic phase shifter is set according to a control voltage. The frequency, amplitude and shape of the control signal can be changed. By applying a sinusoidal control signal with twice the synchrotron frequency and typically 0.7 V amplitude, the lifetime increases by 2 hours resulting from the fact, that the average bunch length is increased due to the RF-phase modulation decreasing the electron density and therefore the Touschek scattering (see [80]). The laser-induced signals (CHG and THz) are corrupted by two mechanisms, the RF-phase modulation and the wake fields of the multibunch train. While the center-of-mass oscillation can be suppressed by the bunch-by-bunch feedback, the RF-phase modulation still decreases the intensity of the laser-induced signal. In Fig. 76, the beam lifetime and the laser-induced THz and CHG signals are compared for different machine configurations. Switching on the the RF-phase modulation increases the beam lifetime but decreases the signal amplitude. By stabilizing the high-current single bunch with the bunch-by-bunch feedback system, the beam lifetime stays the same but the THz and CHG signals are restored to their initial level. Further attempts aim at the synchronization of the laser shot to the phase modulation which was already successfully demonstrated in single-bunch mode [65] but not in hybrid mode.

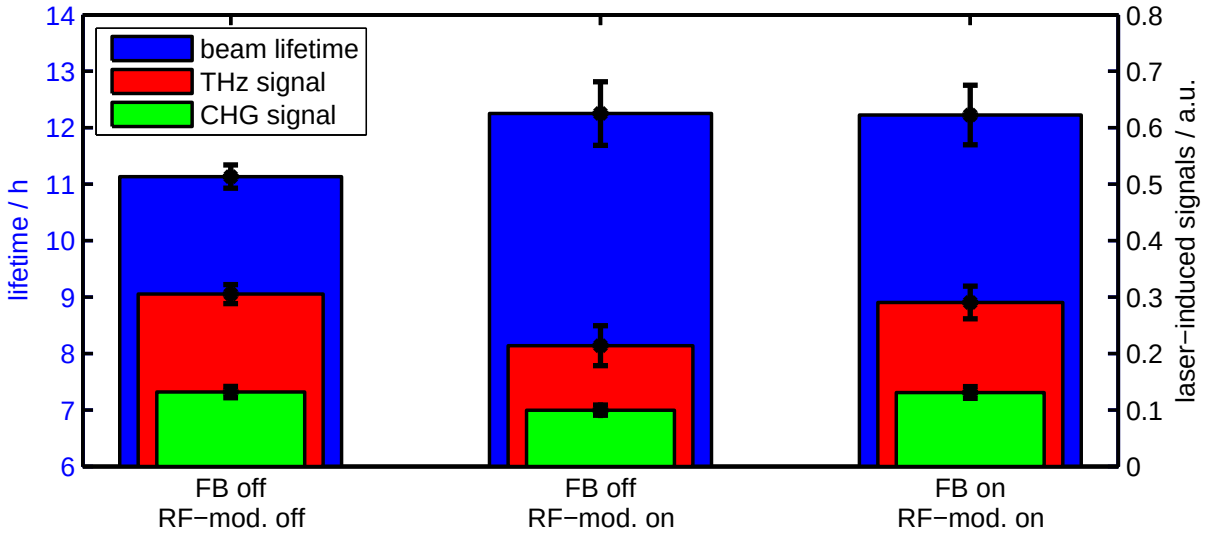

Figure 76: The laser-induced THz (red) and CHG (green) signals and the beam lifetime (blue) are compared for three different combinations of the RF-phase modulation (RF-mod) and the feedback system (FB). The measurement was performed in hybrid mode, and the feedback system was only stabilizing the high-current single bunch.

9.2 Injection Studies

In standard operation, the feedback acquisition unit is triggered internally relative to the revolution trigger. In addition, it can be triggered externally [81]. This allows to study fast transient events, which reappear on a slow timescale. Also grow-damp measurements can be started by an external trigger as it was shown in Sect. 8.4.5 in order to compare feedback measurements with streak camera images. In this section, the investigation of the injection process from the booster synchrotron BoDo to the storage ring DELTA is described. The influence of the injection on the stored electron beam and possible improvements by using the bunch-by-bunch feedback system are shown.

9.2.1 Multibunch Injection

At DELTA, the typical multibunch injection cycle takes 7.2 seconds. In each cycle, electrons are emitted in the thermionic electron gun, accelerated to 75 MeV in a linear accelerator and inserted into the booster synchrotron BoDo. The synchrotron ramps from 70 MeV to 1.5 GeV in 3.2 seconds. Typically, 1 mA is transferred to the storage ring in each cycle, distributed over eight buckets. By changing the injection trigger timing in every cycle, the desired 3/4 filling pattern is achieved. In order to extract the beam from the synchrotron to the storage ring, two extraction kicker and the extraction septum are in use. They are driven by fast high-current pulses in order to extract the entire beam of the synchrotron to the storage ring during one revolution. The extraction kicker directs the beam into the 6 m long transfer channel T2, which consists of two pulsed bending magnets and several quadrupole and steerer magnets. Finally, the beam is injected to the storage ring by the injection septum and three injection kickers which create an orbit bump to accumulate beam in the storage ring. While the kickers are enabled only for one turn in the storage ring (384 ns), the pulsed magnets in the transfer channel have a larger time interval of about 105 ms. Due to imperfect shielding, the pulsed magnets of the transfer channel have a significant influence on the storage-ring orbit during the injection. By triggering the diagnostics unit of the bunch-by-bunch feedback system on the injection, this influence was experimentally observed. In Fig. 77, the rms value of the beam oscillation is plotted as a function of time. To prove that the oscillation from 50 ms to 155 ms correspond to the transfer channel magnets, the magnetic strength of these magnets was reduced resulting in less distortion of the orbit. However, with reduced magnet strength, no injection to the storage is possible.
In addition to the distortion of the orbit by the transfer channel magnets, the injection kickers influence the orbit as well. However, they effect the beam on a smaller timescale. The narrow spike at $t = 75\,\mathrm{ms}$ in Fig. 77 corresponds to the fast kick of the injection kickers, which will be analyzed further in the following. The signal amplitude of one bunch, detected with the bunch-by-bunch feedback system during the fast kick of the injection kicker magnets, is shown in Fig. 78 for different beam currents. Here, the signal is filtered by a

high-pass filter in order to suppress the slow orbit fluctuations. A Hilbert transform (see Sect. 5.3.3) is used to calculate the envelope of the signal. Since the signal is proportional to the bunch current, the amplitude at the injection increases with increasing beam current. The fluctuations result from a timing and voltage mismatch of the three kicker magnets. While the oscillation amplitude decays in less than 150 µs after the initial kick of the kicker magnets, the beam oscillation reoccurs after about 400 µs. Since the feedback system is only capable of detecting the center-of-mass oscillation of the beam, this beating may result from an incoherent oscillation of parts of the bunch, which can not be detected.

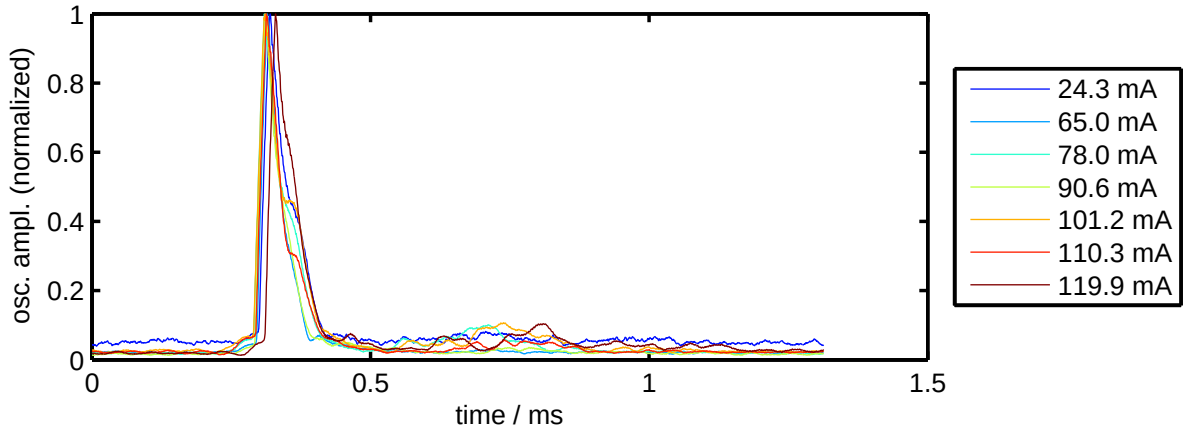

Figure 78: Normalized horizontal oscillation amplitude of one bunch of the multibunch train after the injection for different beam currents. The oscillation is damped after 0.1 ms but shows a reappearance of the bunch oscillation after 0.4 ms.

Taking one injection at 110 mA as an example, it can be shown that the reoccurence of the oscillation does not only affect one bunch but is visible for all bunches of the multibunch train. In Fig. 79, the bunch oscillation of all bunches is shown. In addition to the reocurrence of the horizontal bunch oscillation, the figure shows tilted stripes before and after the injection

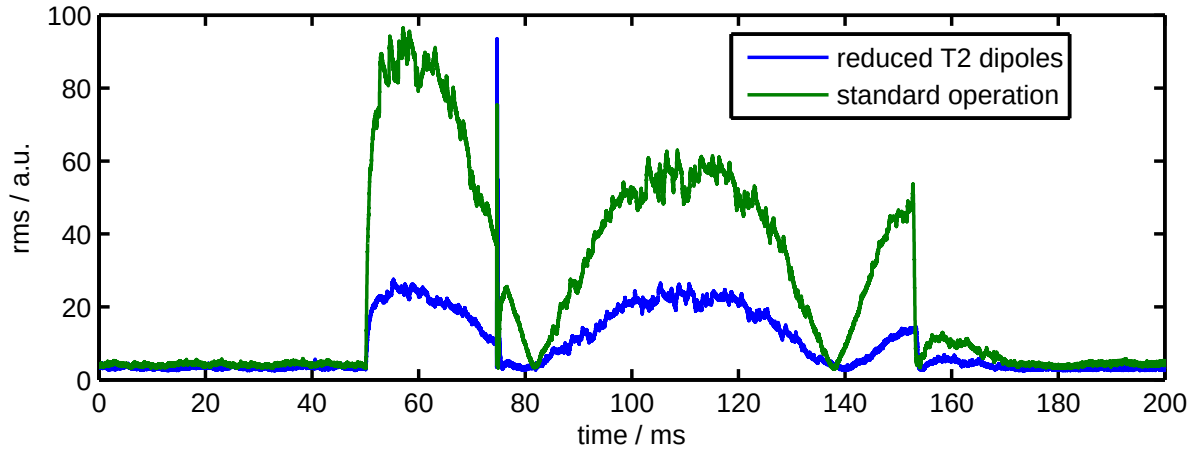

Figure 77: Horizontal rms motion of the electron beam during the injection. The slow oscillation is correlated to the magnets in the transfer channel. The narrow spike at 75 ms is caused by the injection kicker bump.

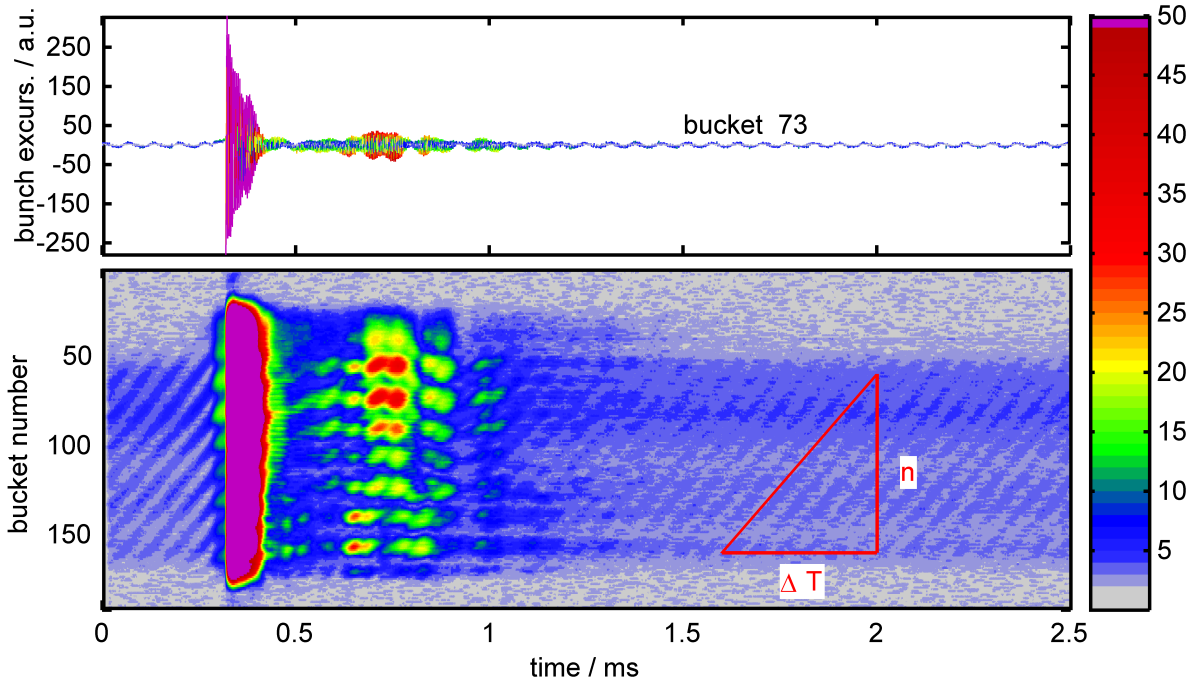

Figure 79: The horizontal beam oscillation after the injection kicker bump was fired at $t = 0.3\,\mathrm{ms}$ is displayed for all bunches (bottom) and for bucket 73 as an example (top). The non-linear colormap emphasizes the reappearance of the bunch oscillation after 0.4 ms. In addition, any oscillation amplitude above a certain level is colored in magenta. The red triangle marks the stripes used to calculate the oscillation mode of the longitudinal coupled-bunch instability.

(Fig. 79, bottom) which can be explained as follows. Due to the dispersion at the BPM position, the longitudinal motion is visible in the horizontal dataset. The tilting angle of the the stripes in Fig. 79 (red triangle) corresponds to the longitudinal multibunch mode 12, which is dominant at DELTA as shown in previous measurements (c.f. Sect. 8.4.1). This can be clearly shown by measuring the time delay ΔT_n for one synchrotron period T_{sync} of two bunches with a bucket separation of n. For a bucket separation of $n = 100$, the time delay ΔT_{100} is determined to 0.4 ms. The time delay can be expressed in terms of a phase advance of one bunch versus the other by

$$\Delta\Phi_n = \frac{\Delta T_n}{T_{\mathrm{sync}}} \cdot 2\pi,$$

which yields $\Delta\Phi_{100} = 39.2\,\mathrm{rad}$. This results in the multibunch mode number

$$\mu = \frac{h}{2\pi} \cdot \frac{\Delta\Phi_{100}}{100} \approx 12,$$

where h is the harmonic number and $\Delta\Phi_{100}/100$ is the phase advance between two adjacent buckets.

The next step is to analyze the frequency spectrum of the bunches. For this purpose, the spectrum of bunch 73 is calculated by a Fast-Fourier-Transform (FFT) for different intervals before and after the injection process. The FFT uses 400 samples of the input signal and an overlap of 200 samples to form the spectrogram given in Fig. 80. Taking 400 samples for the FFT corresponds to a frequency resolution of $f_{\mathrm{res}} = 1/(400 \cdot T_0) = 6.5\,\mathrm{kHz}$. The spectrogram shows four dominant frequency components. The frequency components can be assigned to the horizontal betatron frequency and its second harmonic, the vertical betatron frequency and the longitudinal synchrotron frequency. While the synchrotron frequency is present for the entire measurement interval, the horizontal betatron frequency is only visible for a short time interval after the injection. This is due to the fact that at DELTA the beam is transversely stable, while the beam is only unstable above the longitudinal instability threshold. In addition, the horizontal and vertical betatron frequency show a small frequency shift of about 20 kHz after the injection, which can be explained by an amplitude-dependent tune shift.

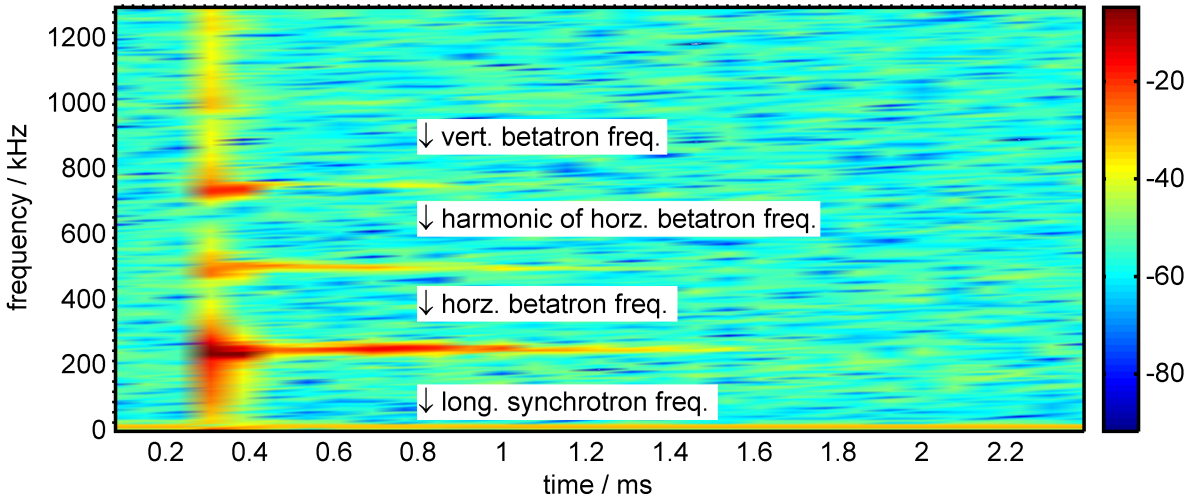

Figure 80: Spectrogram of the beam dynamics after the injection at 0.3 ms. The four different spectral components can be assigned to the synchrotron frequency, the vertical betatron frequency, horizontal betatron frequency and its second harmonic. The color-coded intensity reflects the spectral power on a logarithmic scale.

9.2.2 Optimization of the Injection

The knowledge of the transient beam oscillation directly after the injection allows to observe the oscillation amplitude in order to optimize the injection process and the kicker bump. By real-time visualization of the oscillation amplitude in the control room, a monitor is available to improve the injection process.

In Fig. 81, the variation of the oscillation amplitude when changing the voltage of one of the injection kicker magnets (kicker 1) is shown. The measurement was performed without the

gun trigger being enabled. Therefore, no beam was injected into the storage ring although the entire injection cycle was in operation. When changing the voltage of the kicker magnet beyond a certain deviation, the stored electron beam is lost due to a mismatch of the kicker bump. The measurement shows that at minimum bunch oscillation, there is no beam loss (kicker voltage≈ 21 kV). On the other hand, there is a certain voltage regime at which the beam shows an increased oscillation amplitude without any loss (kicker voltage≈ 19 kV). However, in this regime the kicker voltage is too low to actually inject electrons into the storage ring. Therefore, minimum oscillation amplitude is a good indicator for a matched kicker bump.

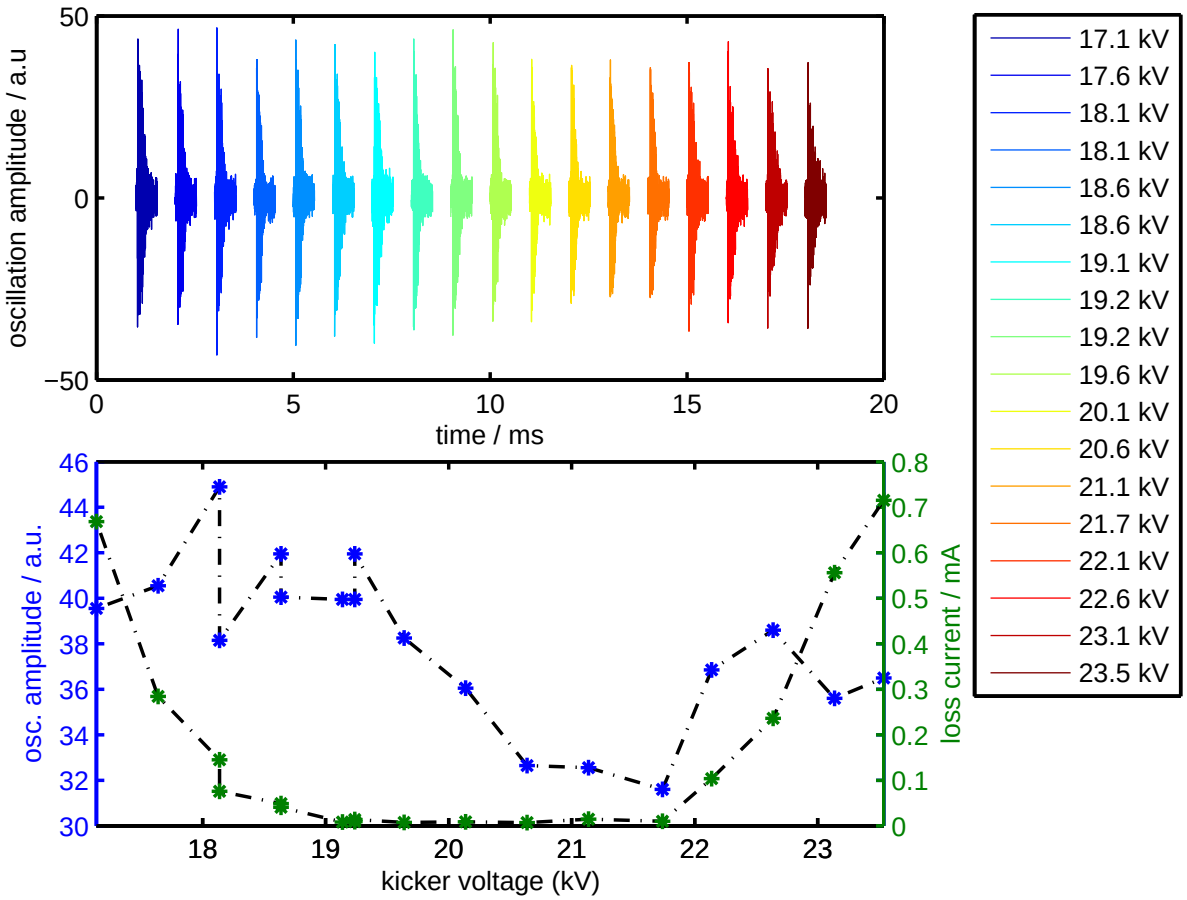

Figure 81: Time evolution of bunch oscillation for different kicker voltages (top). For better visualization, each dataset is shifted by 1 ms relative to the previous one. From the temporal evolution of the bunch after the injection, the oscillation amplitude is extracted (bottom, blue). In addition, the loss current due to a mismatch of the injection kickers is plotted (green).

9.2.3 Single-Bunch Injection

As already mentioned in Sect. 8.6, the single-bunch injection is sometimes limited to a maximum beam current. Reasons for that may be a varying betatron tune, a distorted beam orbit and therefore a slightly different chromaticity of the storage ring, which can lead to head-tail instabilities. A second effect, which reduces the injection efficiency is shown in the following measurement, at which a horizontal instability limits the maximum stored beam current. The orbit was distorted due to a badly calibrated BPM of the orbit correction system. Therefore, the maximum beam current was 4 mA. Above this threshold, additionally injected beam caused an entire beam loss. As described in the previous section, the feedback system was synchronized to the injection trigger. The data show that the beam was oscillating after injection for about 10 ms, which is much longer than the normal oscillation time of less than 1 ms as observed in multibunch operation (see Fig. 78. With the feedback loop closed, the maximum stored beam current increased by more than a factor of two to 11 mA suggesting that the beam is caused by the horizontal oscillation. In addition, the time interval of the collective transverse oscillations decreased to less than 3.5 ms. The oscillation envelope of the single bunch during the injection with open and closed feedback loop is depicted in Fig. 82.
The measurement shows the benefit of the feedback system for the injection process. Whenever a transverse instability limits the injection efficiency, the horizontal feedback can increase the maximum stored beam current.

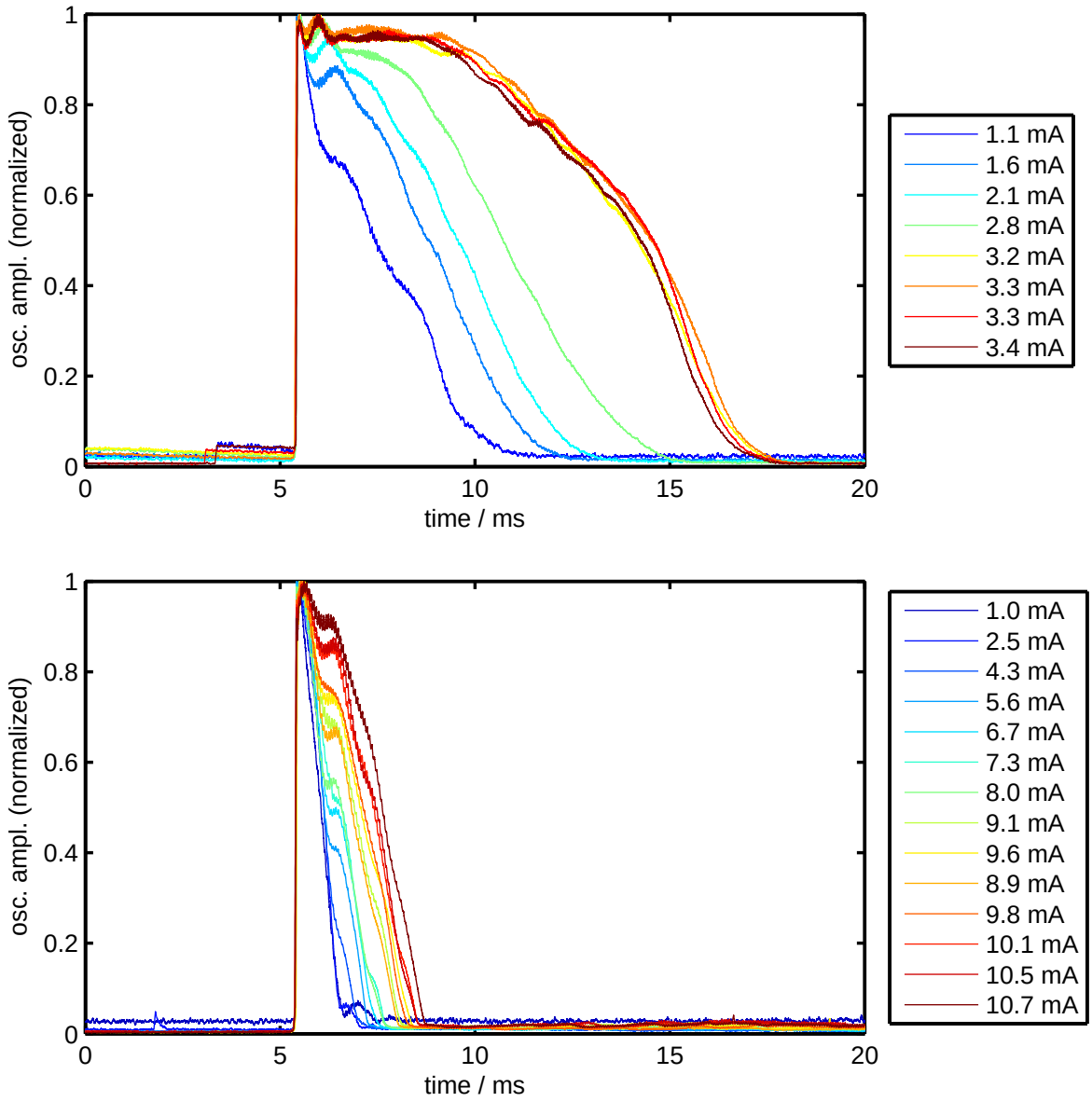

Figure 82: Normalized horizontal oscillation amplitude for different beam currents. Without feedback, the beam oscillates for about 10 ms (top), while with horizontal feedback enabled the beam is stable after less than 3.5 ms. The legend shows the beam current of each individual measurement.

9.3 Beam Loss Detection

Besides triggering the feedback processing units to the injection process, the feedback units can also be triggered to a sudden beam loss. This allows to post-process the beam-position data in order to analyze whether a coupled-bunch instability was responsible for the beam loss.

In order to create a trigger pulse whenever a beam loss occurs, the setup shown in Fig. 83 is used. At DELTA, the total beam current is measured by a parametric current transformer (PCT) of the type described in Ref. [73]. The PCT provides a voltage proportional to the beam current and a second voltage proportional its time derivative. The differential output of the PCT is connected to a threshold trigger-unit, which creates a LVTTL trigger pulse whenever the input voltage exceeds an internal threshold. The threshold can be changed to an arbitrary value in the range of 0 to 200 mV. In the current setup, the trigger threshold is set to 20 mV which corresponds to a loss rate of 205 µA/s as will be shown in this section. After the threshold trigger unit is triggered, it must be reset before it can create a new LVTTL pulse. The reset is automatically performed when the input signal decreases below 8 mV which corresponds to a loss rate of 82 µA/s. At DELTA, the multibunch beam of 130 mA has a typical lifetime of 10 h, which corresponds to a loss rate of 3.6 µA/s well below the reset level. Therefore, the threshold trigger unit is automatically reset in standard operation. Even in single-bunch operation, the typical loss rate is below the reset level (beam current of 20 mA and a typical lifetime of 0.5 h corresponds to a loss rate of 11 µA/s). In addition, the threshold trigger is reset at every injection.

Whenever the beam current shows a rapid change, the differential signal exceeds the threshold and a LVTTL trigger pulse is created to trigger the feedback unit. The feedback diagnostics unit must be set in post-mortem mode, which means that data recorded before the trigger pulse, and therefore before the beam loss, is stored for post processing.

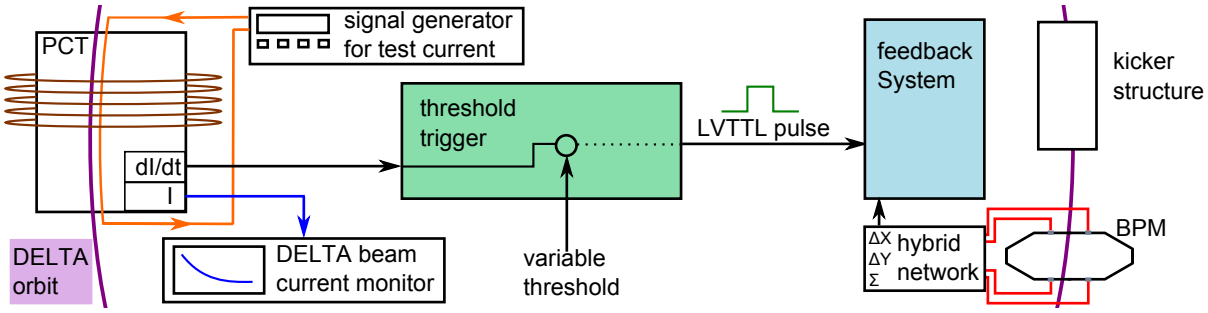

Figure 83: Setup of the beam loss trigger. A PCT provides a signal proportional to the change of the beam current. If this signal is above the manually set threshold, a LVTTL pulse is created which is used as a trigger for the feedback system. The response of the PCT can be tested by using a wire (orange), which is permanently installed inside the PCT.

In order to set the threshold of the trigger unit appropriately, the output signal of the PCT was analyzed for different loss rates. Since a real beam loss would create unwanted radiation and does not have a well-defined loss rate, the beam loss was simulated by using a test wire, which is permanently installed inside the PCT. The impedance of the wire was measured to be $(51 \pm 0.1)\,\Omega$. Therefore, the test current can be calculated from the voltage applied to the wire. In a first step, a sawtooth-shaped signal was applied to the test wire. This signal created a constant loss rate, since the slope of the signal was constant at each period. The signal amplitude for different loss rates is shown in Fig. 84. However, the differential output of the PCT did not show the derivative of the signal, but had a slow rise time. If the frequency of the sawtooth-shaped input signal was increased, in order to increase the loss rate, the differential output signal did not reach the maximum value before the loss rate was changed. Therefore, this calibration is only valid for small loss rates. A linear fit to the rising edge of the data with a fixed intercept at zero provides the following relation between the output signal U_S and the loss rate dI/dt

$$U_s = (97.4 \pm 0.6)\frac{Vs}{A} \cdot \frac{dI}{dt}.$$

Therefore, the threshold of the trigger unit of 20 mV corresponds to 205 µA/s and the reset threshold of 8 mV corresponds to 82 µA/s .

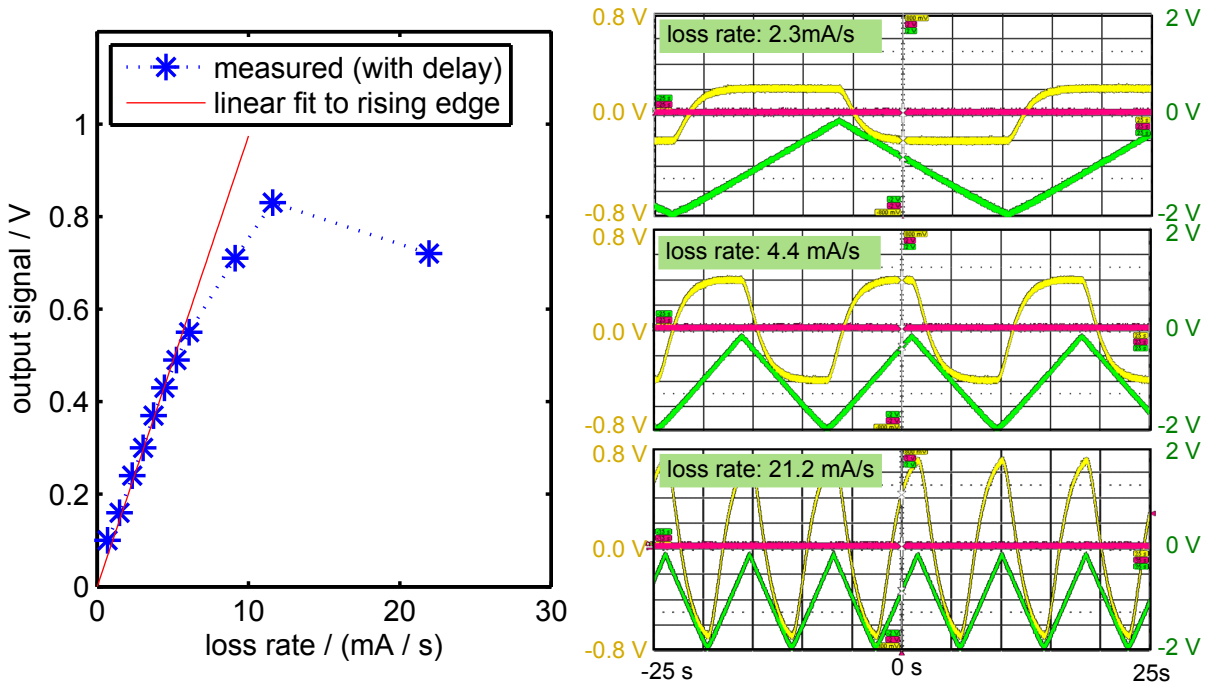

Figure 84: Differential output signal of the PCT for different loss rates (left, blue). A linear fit to the first seven datapoints allows to correlate the output signal with the loss rate (left, red). Three scope traces are shown on the right. The input signal is sawtooth-shaped (green) while the differential output signal (yellow) shows a delayed response to changes of the input signal.

A different approach uses a rectangular-shaped signal in order to simulate an immediate beam loss. The maximum output signal is plotted in Fig. 85 as function of the current loss. A linear fit provides

$$U_s = (66 \pm 0.5)\frac{V}{A}\Delta I$$

with the current loss ΔI.

Besides the amplitude of the output signal, it is important to know the time delay between the beam loss and the creation of the trigger pulse. Since the output signal of the PCT can not immediately follow the input signal, it takes several milliseconds before the trigger threshold is exceeded. This is shown in Fig. 86. The delay of the created LVTTL pulse relative to the beam loss depends on the current loss ΔI. The larger the beam loss, the smaller is the delay between the creation of the trigger pulse and the beam loss. The delay ΔT is given by

$$\Delta T = (91.5 \pm 2) \cdot \left(\frac{dI}{dt}\frac{\text{s}}{\text{mA}}\right)^{-(0.99\pm0.02)} \text{ ms}.$$

To be able to observe large beam losses as well as small ones, the feedback processing units need to acquire beam position data for more than 40 ms, since the actual delay of the trigger relative to the beam loss is not known in advance. This requires to down-sample the input data at least by a factor of two to be able to store 50 ms. This has the strong drawback that only every second turn is stored.

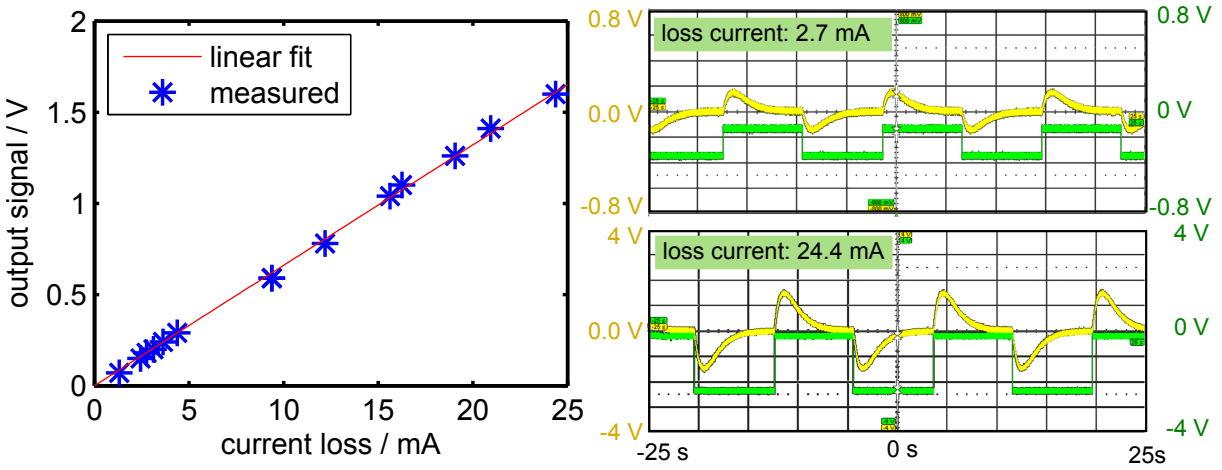

Figure 85: Differential output signal of the PCT for different current losses (left, blue). A linear fit to the data points allows to correlate the output signal with the current loss (left, red). Two scope traces are shown on the right. The input signal is rectangular-shaped (green) while the differential output signal (yellow) shows a delayed response to changes of the input signal.

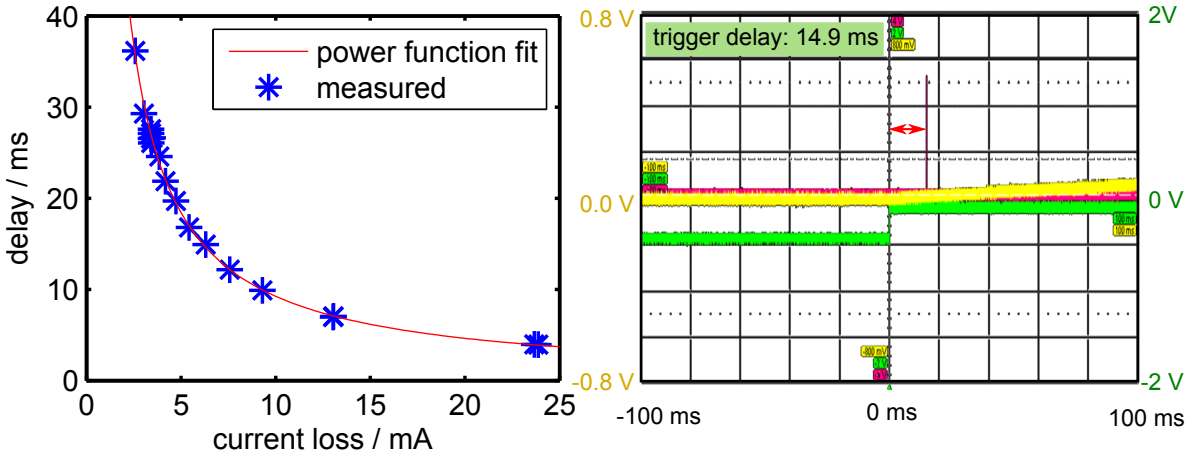

Figure 86: Delay of the LVTTL trigger pulse for different current losses (left, blue). A power function fit to the datapoints allows to correlate the trigger delay with the current loss (left, red). An scope trace is shown on the right. The input signal is rectangular-shaped (green) while the differential output signal (yellow) shows a delayed response to changes of the input signal. The LVTTL trigger pulse (red) is created 14.9 ms after the beam loss.

In Fig. 87, a example of beam loss is shown. Here, the horizontal beam oscillation is significantly increased before the beam loss, which might be responsible for the beam loss. Since only one horizontal multibunch mode is excited before the beam loss, the beam loss is most likely not caused by an RF failure but might caused by a quadrupole failure.

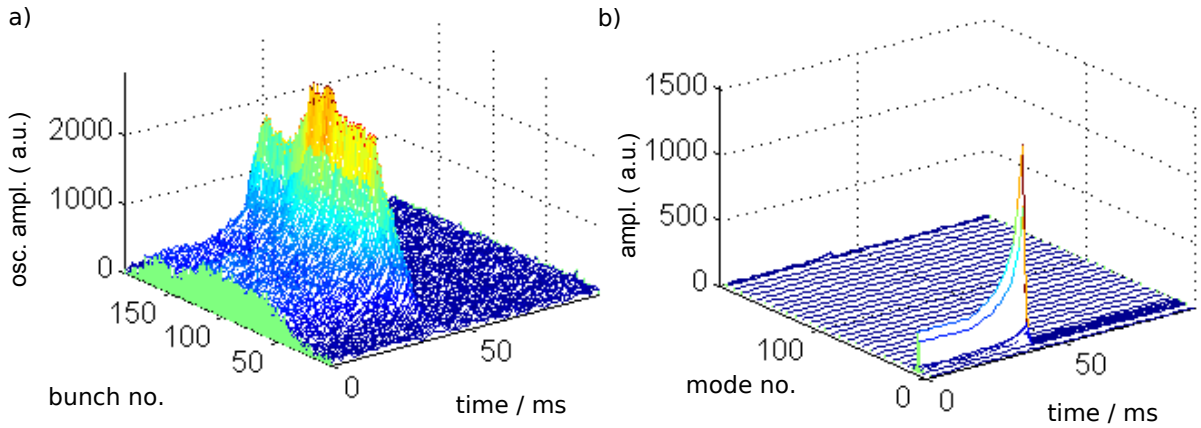

Figure 87: Horizontal beam oscillation before the entire beam was lost (left) and the corresponding mode spectrum (right).

9.4 Other Applications

Finally, two other applications of the feedback system will be shortly presented.

9.4.1 Bunch Cleaning

By using the internal NCO of the feedback system, the oscillation of every bunch can be excited individually. By exciting one bunch vertically with the vertical betatron frequency, the bunch starts to oscillate until it exceeds the aperture of the machine and is lost. Therefore, an arbitrary filling pattern can be created with the bunch-by-bunch feedback by exciting selected bunches, which is called bunch cleaning. In Fig. 88, three example filling patterns are presented, which were created by bunch cleaning. In order to match the betatron frequency of the bunch which is to be removed, the excitation frequency is periodically varied in the kHz regime with a typical period length of 100 µs. Since the kicker response shows a small coupling to the neighboring bunches as shown in Sect. 8.2, it is useful to simultaneously apply negative feedback to all other bunches which are not to be removed.

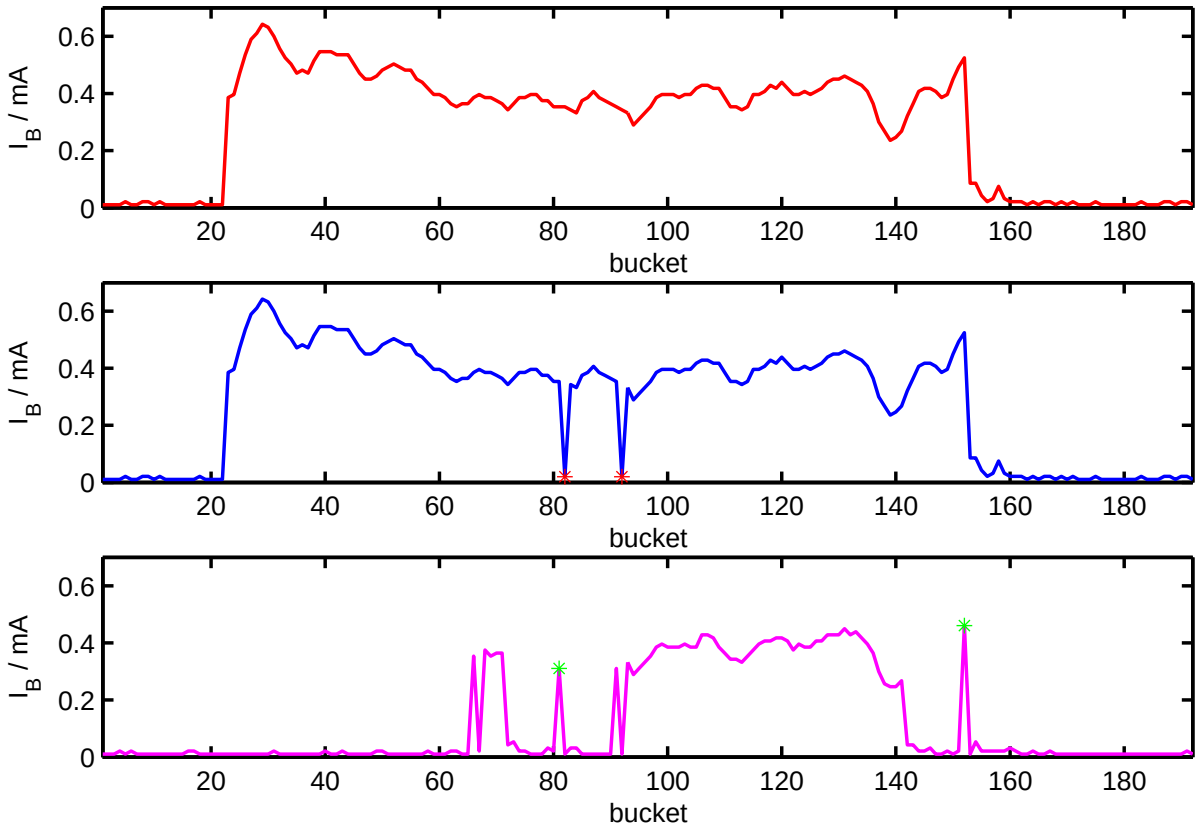

Figure 88: Three different filling patterns of the storage ring. In standard operation the ring is filled with 144 buckets (top). It is possible to kick out single bunches (center, bunches 82 and 92). This can be used to create arbitrary filling patterns and to separate single bunches from the bunch train (bottom, bunches 81 and 152).

9.4.2 Bunch-by-Bunch Data from the Booster Synchrotron

Another application of the feedback system is to use its diagnostic capabilities at the booster synchrotron BoDo. In order to operate the feedback system at the BoDo harmonic number of 84, a different configuration file must be loaded into the FPGA of the processing units. The whole ramping cycle of BoDo takes 7.2 seconds. Half of the time, the electron bunches are inside the synchrotron. Since the processing units of the feedback system are only capable to store 65000 turns without downsampling, which corresponds to approximately 10 ms at BoDo, a downsampling of 24 was used and the beam position data was stored for 250 ms. In addition, in order to take snapshots of the beam dynamics over the whole interval (3.6 s), the trigger signal was delayed by a delay generator. In Fig. 89, four different phases of the ramping cycle are shown. These are the injection into BoDo (a) and extraction (d), one snapshot at the actual ramping of the magnets (b) and one snapshot at the plateau of the the ramp cycle (d), when the magnets have reached their final field, but the beam is not yet extracted. As expected, strong phase oscillations are observed during the ramping of the synchrotron.
These measurements only demonstrate the operability of the feedback system at the booster synchrotron. Detailed studies have to follow in future measurements.

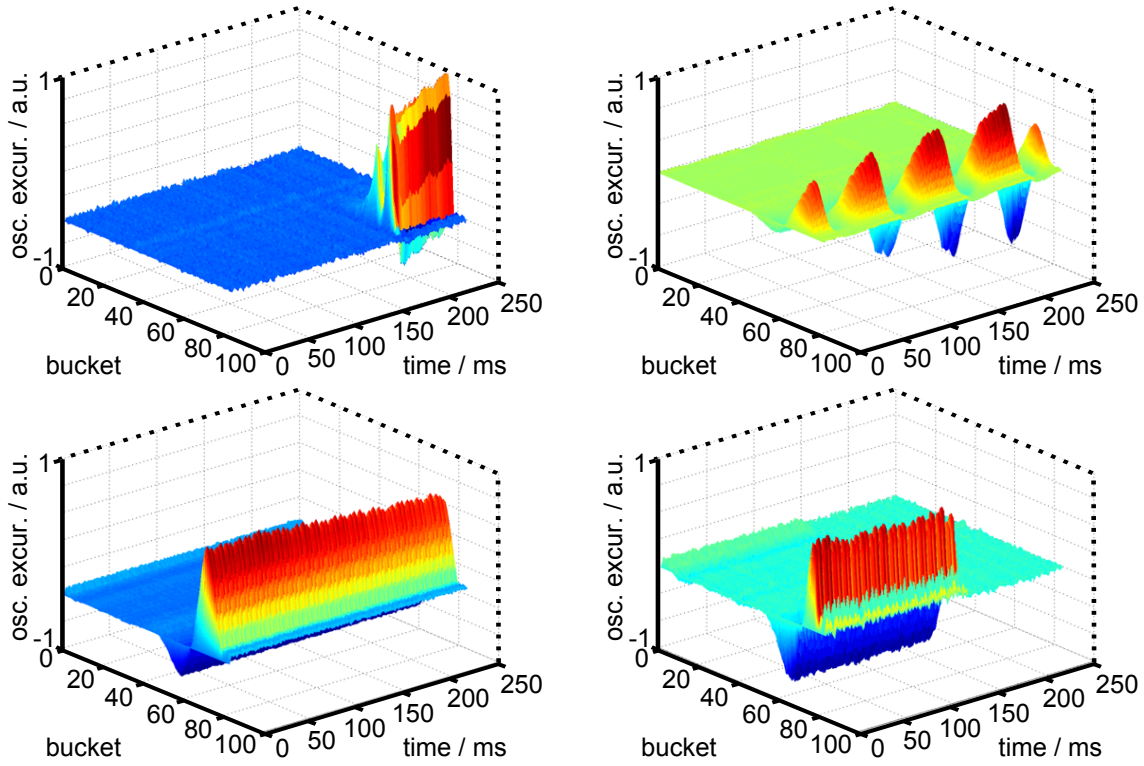

Figure 89: Longitudinal beam dynamics in the booster synchrotron BoDo at injection (a), during the ramping cycle (b), on the flat top (c) and at extraction to the storage ring (d). Since only 8 buckets are filled at each injection cycle, all other buckets show no oscillation at all.

10 Summary and Outlook

Beam instabilities decrease the brilliance of synchrotron radiation and limit the storable beam current. In order to investigate and suppress beam instabilities at DELTA, a digital bunch-by-bunch feedback system was installed and commissioned. The feedback systems allows to measure and store the beam position data for several ten thousand turns for post-processing.
By a modal analysis of this data, the mode amplitude of all multibunch modes is calculated and displayed in the control room. An integrated numerically-controlled oscillator (NCO) and the possibility of a pulsed excitation, enables to investigate the transient behaviour of coupled-bunch instabilities. In addition, the system can be triggered to external events like the beam injection or beam loss.

10.1 Characterization of Beam Instabilities at DELTA

At DELTA, the multibunch beam is longitudinally unstable at a beam currents above 55 mA without the superconducting wiggler and above 75 mA with the wiggler enabled. Depending on the actual orbit position and the RF cavity settings, these thresholds vary by up to ±5 mA. It was shown that, depending on the filling pattern, a variety of multibunch modes are present at the instability threshold. The longitudinal multibunch mode 12 ($f = 31.2\,\mathrm{kHz}$) was identified as the mode with the highest growth rate.
Since the electron beam is usually oscillating only in the mode with the highest growth rate, an external excitation was applied to the beam in order to study all other multibunch modes. This measurement was systematically repeated for all multibunch modes at different beam currents in order to characterize these modes.
For better understanding of this and other measurements, a simulation program was created, which is able to calculate the longitudinal bunch position of all bunches under the influence of narrow-band impedances like, for example, higher-order modes of the accelerating cavity. The feedback system was included in the simulation.
A set of longitudinal narrow-band impedances was calculated by which the observed damping rates could be reproduced in the simulation. Especially the symmetry between corresponding pairs of multibunch modes was reproduced by simulations. Based on the calculated impedances, the simulation tool was used to explain the coupling mechanism between different bunches.
In addition to the characterization of multibunch instabilities, single-bunch instabilities were observed. It was shown that the bunch is unstable for negative chromaticities. The transverse oscillation could be suppressed by the transverse feedback system. It was shown that the maximum stored beam current may be increased by a factor of at least two by employing the feedback system, whenever transverse instabilities are present at the injection process.

10.2 Benefits to the DELTA short-pulse facility

The DELTA short-pulse facility is in operation since 2011. Based on the coherent harmonic generation principle (CHG), the short-pulse facility provides ultrashort ($\tau_{\mathrm{FWHM}} \approx 50\,\mathrm{fs}$) radiation pulses in the VUV regime. The CHG principle uses an ultrashort laser pulse which interacts with the electrons in the first part part of the undulator U250.
Since the intensity of coherent radiation is proportional to the number of electrons squared, it is important that the laser pulse interacts with the center part of the electron bunch. Usually, CHG experiments are performed in dedicated shifts, in which a high-current single bunch is injected into the storage ring. If CHG is performed in a hybrid filling pattern, in which the high-current single bunch is injected in the gap of the standard multibunch train, the wakefields of the bunches in the multibunch train excite the single bunch to oscillate longitudinally. Therefore, the laser does not interact with the center part of the electron bunch anymore, which reduces the mean CHG signal and increases the shot-to-shot fluctuations. By damping the oscillation of the single bunch with the bunch-by-bunch feedback, it was possible to increase the CHG signal in hybrid mode by a factor of two. However, in standard multibunch operation a RF-phase modulation is routinely applied in order to increase the beam lifetime by up to 2 hours. This phase modulation does also degrade the CHG signal. It was shown that a stabilization of the single bunch with the feedback system allows to increase the CHG signal while the RF-phase modulation simultaneously increases the lifetime of the electron beam.

10.3 Outlook

At DELTA, plans are ongoing to perform CHG measurements at a lower beam energy of 500 MeV. Since the intensity of the CHG signal depends on the relative energy modulation, the signal increases when the beam energy is reduced. With reduced beam energy, the radiation damping is reduced and the growth rates of the multibunch instabilities are increased. Therefore, the bunch-by-bunch feedback system will be an important tool to allow for a stable beam operation. For the lower beam energy, the instability thresholds will change, which has to be investigated. A further step will be the comparison of instability thresholds for various beam energies.

A second topic under investigation is the analysis of damping rates of various multibunch modes under the influence of the RF-Phase modulation.

In [82] it was shown, that the beta function can be measured at all BPM positions by observing the beam response after a short excitation of the beam. So far, the excitation is applied by a kicker magnet with a repetition rate of 10 Hz. By using the NCO of the feedback system, the excitation could be applied continuously to the beam. In addition, the excitation could be limited to one bunch, which reduces the external disturbance of the total beam during standard operation. The same excitation could be used for the betatron tune

feedback which also uses the 10 Hz excitation signal in order to determine the tunes.

Finally, a new impedance model for the DELTA storage ring should be determined which is able to assign elements of the DELTA storage ring to the calculated impedances based on the damping rates. The simulation tool is able to predict beam oscillations for a given impedance pattern and can be used as benchmark for a calculated impedance pattern.

A Appendix

A.1 Graphical User Interface

In order to parametrize and operate the simulation program described in Sect. 5, a graphical user interface (GUI) was created (see Fig. 90). The GUI allows to define simulation parameters and start simulations. In addition, the simulation tool can be started from the MATLAB command shell in order to automate simulation runs with varying parameters. The GUI is structured as follows

- **machine parameters** sets the basic machine parameters, the cavity parameters and the parameters of the feedback system. Further parameters and Higher-order-modes can be inserted by a submenu or read from a file.
- **simulation parameters** sets the time intervals for the simulation. This includes the total simulation time, the turns at which the cavity loop is enabled, at which the feedback system is active and at which the beam is injected. The beam could be either used from a previous simulation or a new beam could be created. In addition, the time intervals are given graphically in the top figure. The feedback pattern and the bunch pattern are shown in the bottom figure, which are the set of buckets which are either filled (bunch pattern) or which are dealt with by the feedback (feedback pattern).
- **load dataset** allows to continue a previous simulation. In that case, the last cavity phasor, beam loading phasor and generator phasor are used for the new simulation. The particle beam can be retained as well. In that case, all bunches keep their bunch current, energy and phase.
- **setups** fills in some example simulation parameters for different types of simulations, which can be used one after the other in order to create realistic conditions for further simulations.
  - **fill cavity** starts the simulation with no beam in order to fill the cavity from the generator.
  - **cavity loop** enables the cavity feedback loops to detune the cavity accordingly.
  - **inject beam** creates a multibunch beam
  - **damped beam** enables the feedback system in order to damp any oscillation of the beam
  - **grow-damp** performs a grow-damp-measurement, where the feedback coefficient set is switched temporarily in order to excite the beam by a positive feedback.
- **start simulation** runs the simulation with the chosen parameters. The simulation can be aborted at any turn and the current beam parameters are saved.

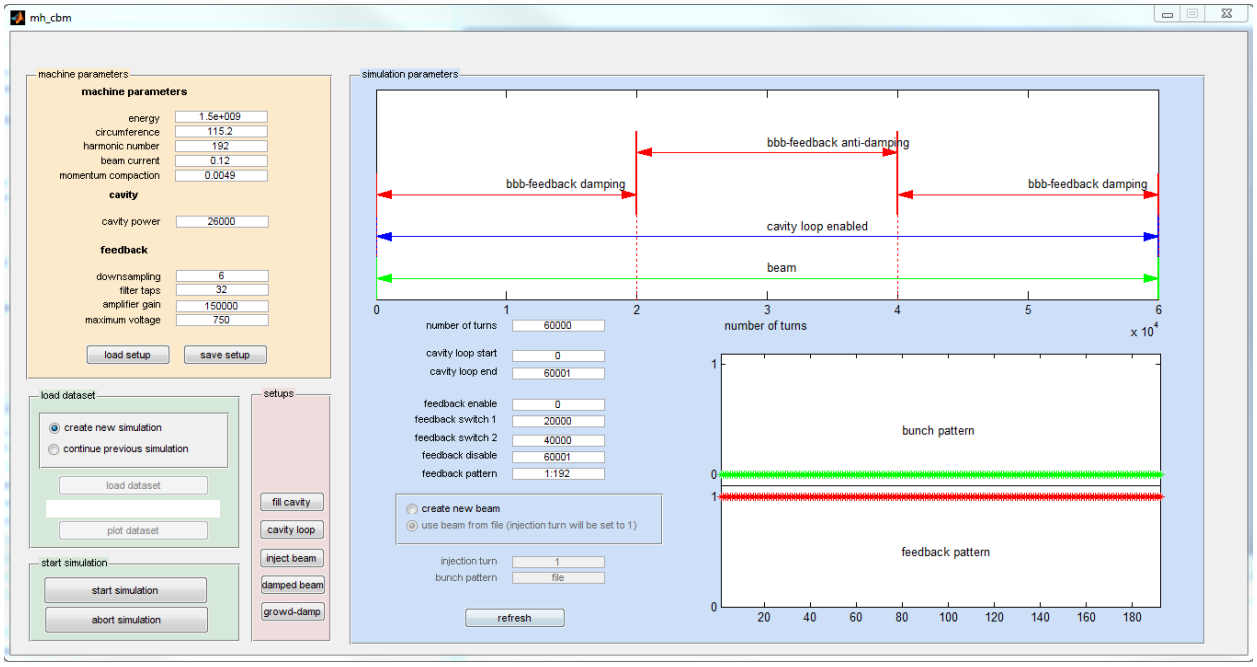

Figure 90: Graphical User Interface of the simulation tool.

A.2 Control-Room Interfaces

The feedback processing units and the feedback frontend and backend module are remotely accessible by a variety of EDM panels [83] through EPICS [84]. Detailed descriptions of the parameters can be found in [24]. Here, only the basic structure and parameters are described (cf. Fig. 91).

- **Main** allows to switch on the feedback and allows to call the setup panel .
- **Setup** provides access to all settings of the feedback units. It can be chosen between filter coefficients set one and two. It gives an overview on possible errors.
- **Coefficients** defines filter coefficients of the feedback FIR filter.
- **Devices** defines the input trigger thresholds and the coefficients of the output signal-shaping FIR filter. Gives access to external devices like power amplifiers, if configured.
- **Timing** sets the input and output delays.
- **Drive** is a numerically-controlled oscillator (NCO) to apply a signal with defined frequency and amplitude to a chosen bunch. The frequency can be automatically varied in a defined way.
- **SRAM/BRAM control** sets the acquisition time and possible intervals for switching between the two filter sets for the respective small (**BRAM**) and long (**SRAM**) data acquisition units.

- **SRAM/BRAM waveforms** provides real-time access to the mean and rms signal of every bunch and the time evolution of the bunch with largest rms signal. In addition, the bunch spectrum of chosen bunches is displayed.
- **Environment** displays voltage and temperature of relevant components of the system.
- **Config S/R** saves and restores the feedback setting of the unit.
- **Front/back-end** gives access to the frontend and backend module to change phase shifter settings and attenuation. Provides access to an automatic phase-servo loop which varies the reference phase in order to keep longitudinal plane in the phase-sensitive regime.

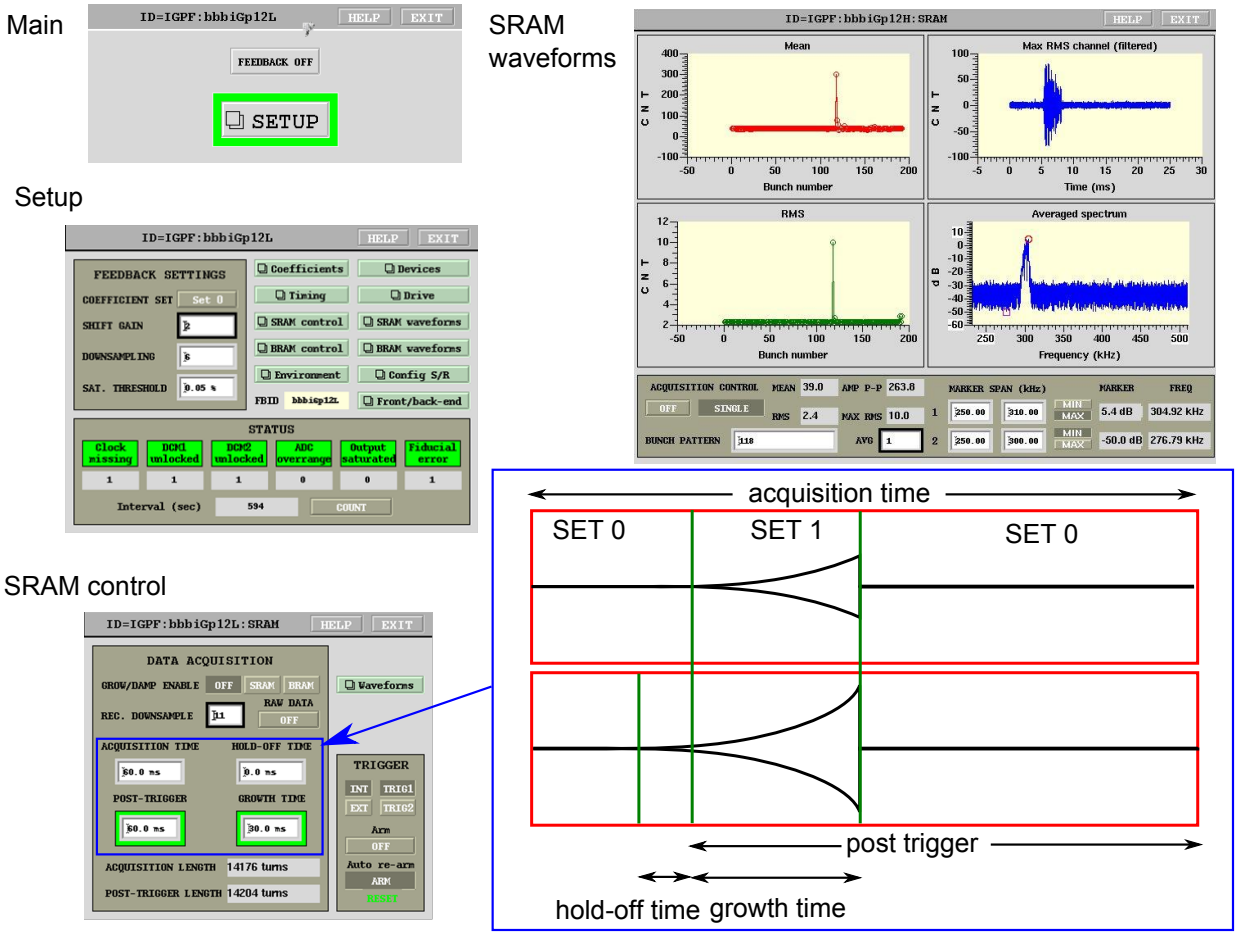

Figure 91: Overview of the main EDM panels of the feedback system [24]. The sketch next to the SRAM control panel shows the relative timing which can be applied in order to perform a switch of the filter sets.

In addition to the EDM panels, a MATLAB control interface was implemented (Fig. 92), which combines all parameters needed for data acquisition for all units. It has direct access to the feedback units via EPICS. Furthermore, additional features are added to start different

parameter scans. The capabilities of the different blocks of the panel are described in the following.

- **main** allows to enable or disable the feedback units. In addition the **setup** or **waveform** EDM panels can be opened.
- **DG535 settings** shifts the trigger delay of the external input trigger. This is, for example, useful when synchronizing the feedback acquisition to the BoDo ramping cycle. By shifting the delay, different intervals of the cycle can be observed and compared.
- **feedback control** allows to choose the feedback coefficient set, sets the NCO settings and the acquisitions settings. It is possible to apply the acquisition set for one plane to the other two planes.
- **take dataset** saves one or more datasets with user-defined name and time stamp.
- **calibration** runs a parameter scan of phase shifters and delays to find optimum setpoints for data acquisition. More details of the calibration procedure is given in Sect. 8.1.
- **sweep measurements** allows to perform several automatic measurements, e.g. the drive frequency can be changed automatically to a specific multibunch mode. The excitation unit and the units used for data acquisition can be chosen.
- **other measurements** provides several shortcuts for starting other MATLAB scripts. The "mode display" script opens a second GUI, which allow to visualize the mode spectrum during machine operation (see Fig. 93)

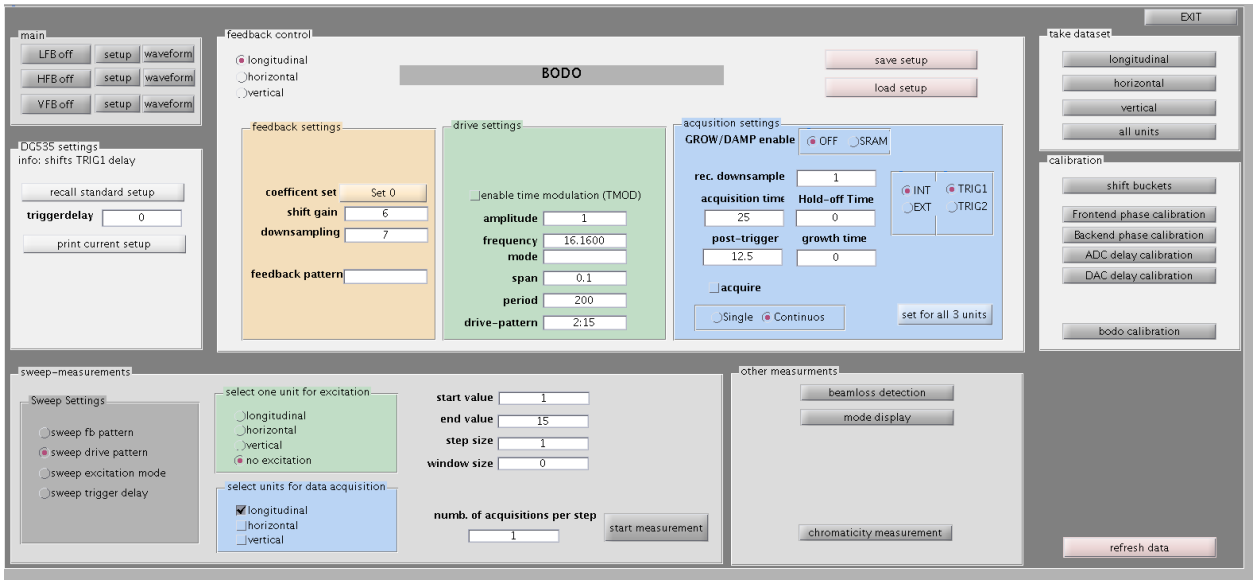

Figure 92: Overview of the MATLAB GUI to control the feedback system and to start automatic measurement runs.

The mode visualization tool calculates the mode spectrum based on the longitudinal position data. The calculation of the mode spectrum is performed as explained in Sect. 5.3.5. The different blocks of the tool are explained in the following.

- **setup** allows to set the acquisition time, the downsampling factor, the synchrotron frequency and the mode number of the mode that should be displayed.
- **long-term interval** displays the mode amplitude of the chosen mode in the long-term interval since the measurement was started (top). In addition to the mode-dependent visualization, the tool displays the spectral component at the synchrotron frequency of the single-bunch spectrum (bottom).
- **short-term interval** displays the mode amplitude for the last 70 data-acquisition steps (top). In addition, the mode amplitude of all modes is plotted for the last 70 data-acquisition steps (middle) and for the last two acquisition steps (bottom).

The tool saves the mode amplitudes of all modes, the spectral component at the synchrotron frequency and the beam current for each time step in order to enable offline analysis of the data.

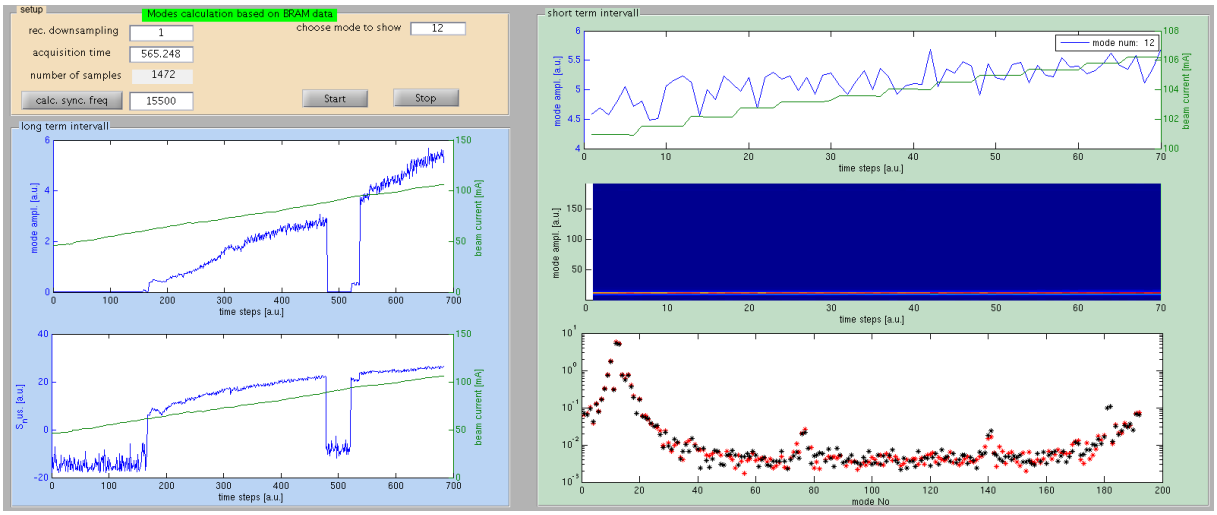

Figure 93: Overview of the mode visualization tool. The data shows the injection process, with an increase of the mode amplitude above the instability threshold. The temporary decrease of the oscillation amplitude results from beam stabilization by the longitudinal bunch-by-bunch feedback system.

A.3 Generator Power

The necessary generator power for a given cavity tuning ψ and coupling β was given in Sect. 5 in Eq. 5.18. In the following the equation will be derived.

The total cavity voltage is given by (see Eq. 5.2)

$$\tilde{V}_C = \tilde{V}_B + \tilde{V}_G \tag{A.1}$$

with the beamloading voltage (see Eq. 5.12)

$$\tilde{V}_B = -V_{B,R} \cdot \cos(\psi) \cdot e^{i\psi} \tag{A.2}$$

and the generator voltage (see Eq. 5.15)

$$\tilde{V}_G = V_{G,R} \cdot \cos(\psi) \cdot e^{i(\psi+\theta)}. \tag{A.3}$$

Taking the real part yields

$$\begin{aligned} \mathrm{Re}\left\{\tilde{V}_C\right\} &= \mathrm{Re}\left\{\tilde{V}_B + \tilde{V}_G\right\} = \mathrm{Re}\left\{-V_{B,R} \cdot \cos(\psi) \cdot e^{i\psi} + V_{G,R} \cdot \cos(\psi) \cdot e^{i(\psi+\theta)}\right\} \\ &\Leftrightarrow \qquad (A.4) \\ V_C \cdot \cos\left(\phi_S\right) &= V_{G,R} \cdot \cos(\psi) \cdot \cos(\psi+\theta) - V_{B,R} \cdot \cos^2(\psi) \qquad (A.5) \end{aligned}$$

respectively

$$V_C \cdot \cos\left(\phi_S\right) + V_{B,R} \cdot \cos^2(\psi) = V_{G,R} \cdot \cos(\psi) \cdot \cos(\psi+\theta), \tag{A.6}$$

while taking the imaginary part yields

$$\begin{aligned} \mathrm{Im}\left\{\tilde{V}_C\right\} &= \mathrm{Im}\left\{\tilde{V}_B + \tilde{V}_G\right\} = \mathrm{Im}\left\{-V_{B,R} \cdot \cos(\psi) \cdot e^{i\psi} + V_{G,R} \cdot \cos(\psi) \cdot e^{i(\psi+\theta)}\right\} \\ &\Leftrightarrow \qquad (A.7) \\ V_C \cdot \sin\left(\phi_S\right) &= V_{G,R} \cdot \cos(\psi) \cdot \sin(\psi+\theta) - V_{B,R} \cdot \cos(\psi) \cdot \sin\left(\psi\right) \qquad (A.8) \end{aligned}$$

respectively

$$V_C \cdot \sin\left(\phi_S\right) + V_{B,R} \cdot \cos(\psi) \cdot \sin\left(\psi\right) = V_{G,R} \cdot \cos(\psi) \cdot \sin(\psi+\theta). \tag{A.9}$$

Adding up Eq. (A.6) and Eq. (A.9) quadratically yields

$$V_{G,R}^2 \cdot \cos^2(\psi) = \left(V_C \cdot \cos(\phi_S) + V_{B,R} \cdot \cos^2(\psi)\right)^2 + \left(V_C \cdot \sin(\phi_S) + V_{B,R} \cdot \cos(\psi) \cdot \sin(\psi)\right)^2 \quad (A.10)$$

$$\Leftrightarrow$$

$$V_{G,R}^2 = \frac{V_C^2}{\cos^2(\psi)} \left[\left(\cos(\phi_S) + \frac{V_{B,R}}{V_C} \cdot \cos^2(\psi) \right)^2 + \left(\sin(\phi_S) + \frac{V_{B,R}}{V_C} \cdot \cos(\psi) \cdot \sin(\psi) \right)^2 \right]. \quad (A.11)$$

With $V_{G,r} = 2 \cdot \frac{\sqrt{\beta}}{1+\beta} \cdot \sqrt{2 \cdot R \cdot P_G}$ (see Eq. 5.14) the expression for the generator power is given by

$$P_G = \frac{V_C^2}{2R\cos^2(\psi)} \frac{(1+\beta)^2}{4\beta} \left[\left(\cos(\phi_S) + \frac{V_{B,R}}{V_C} \cdot \cos^2(\psi) \right)^2 + \left(\sin(\phi_S) + \frac{V_{B,R}}{V_C} \cdot \cos(\psi) \cdot \sin(\psi) \right)^2 \right] \quad (A.12)$$

With $V_{B,R} = 2I_0R_S/(1+\beta)$ the expression for the generator power is finally given by (c.f. Eq. 5.18)

$$P_G = \frac{V_C^2}{2R_S} \cdot \frac{(1+\beta)^2}{4\beta} \cdot \frac{1}{\cos^2(\psi)} \left[\left(\cos(\phi) + \frac{2I_0R_S}{V_C(1+\beta)} \cos^2(\psi) \right)^2 + \left(\sin(\phi) + \frac{2I_0R}{V_C(1+\beta)} \cos(\psi) \sin(\psi) \right)^2 \right]. \quad (A.13)$$

A APPENDIX

B References

[1] W. C. Röntgen, *Über eine neue Art von Strahlen*, Sitzungsberichte der physikalisch-medizinischen Gesellschaft zu Würzburg 132 (1895).

[2] F. Elder et al., *Radiation from electrons in a synchrotron*, Physical Review 71, 829 (1947).

[3] T. Shintake, *Radiation 2D*, www.shintakelab.com (1984).

[4] E. M. Rowe, *TANTALUS I : A Dedicated Storage Ring Synchrotron Radiation Source*, Particle Accelerators 4, 211 (1973).

[5] A. L. Robinson, *X-Ray Data Booklet Section 2.2 - History of Synchrotron Radiation*, Lawrence Berkeley National Laboratory (2001).

[6] Z. Huang and M. Park, *Brightness and Coherence of Synchrotron Radiation and FELs*, SLAC-PUB-15449 (2013).

[7] A. W. Chao, *Physics of Collective Beam Instabilities in High Energy Accelerators*, Wiley (1993).

[8] S. Khan, *Collective Phenomena in Synchrotron Radiation Sources*, Springer (2006).

[9] F. J. Sacherer, *A Longitudinal Stability Criterion for Bunched Beams*, Nuclear Science 825 (1973).

[10] F. J. Sacherer, *Transverse Bunched Beam Instabilities - Theory*, Proc. 9th International Conference on High Energy Accelerators, 347 (1974).

[11] Center for Synchrotron Radiation, *http://www.delta.tu-dortmund.de/*.

[12] K. Wille and S. Radiation, *Initial Experience with DELTA*, Proc. European Particle Accelerator Conference 1996, Barcelona, Spain, 3 (1996).

[13] G. Schmidt et al., *Status of the Synchrotron Light Source DELTA*, Proc. European Particle Accelerator Conference 2002, Paris, France, 745 (2002).

[14] R. Heine et al., *Investigations of Cavity Induced Longitudinal Coupled Bunch Mode Instability Behaviour and Mechanisms*, Proc. European Particle Accelerator Conference 2004, Lucerne, Switzerland, 1990 (2004).

[15] F. Marhauser et al., *HOM Damped 500 Mhz Cavity Design for 3rd Generation SR Sources*, Proc. Particle Accelerator Conference 2001, Chicago, USA, 846 (2001).

[16] F. Marhauser et al., *First Tests of a HOM-Damped High Power 500 Mhz Cavity*, Proc. European Particle Accelerator Conference 2004, Lucerne, Switzerland, 979 (2004).

[17] R. Heine et al., *Characterisation of the EU-HOM-Damped Normal Conducting 500 MHz Cavity from the Beam Power Spectrum at DELTA*, Proc. European Particle Accelerator Conference 2006, Edingburgh, Scotland, 2856 (2006).

[18] P. H. Lehnart, N, *Ferrit-Dämpfungsantennen gegen parasitäre Cavity-Modes in den DORIS - Hohlraum - Resonatoren*, DESY - Technische Notiz - H2-77/12 (1977).

[19] R. Heine, *Untersuchung der Wechselwirkung intensiver Elektronenstrahlen mit höheren Resonatormoden an Delta*, PhD thesis, TU Dortmund University (2006).

[20] K. Dunkel, *Monitoring der longitudinalen Speicherringimpedanz von DELTA , Einfluss auf Bunchlänge und Bunchlängenmanipulation*, PhD thesis, TU Dortmund University (2008).

[21] J. Fürsch, *Lebensdauerverbesserung und Strahlstabilisierung durch longitudinale Phasenmodulation am Elektronenspeicherring Delta*, PhD thesis, TU Dortmund University (2014).

[22] S. Khan et al., *Studies and Control of Coupled-Bunch Instabilities at DELTA*, Proc. 1st International Particle Accelerator Conference 2010, Kyoto, Japan, 2755 (2010).

[23] M. Höner et al., *Bunch-by-Bunch Feedback Systems at the DELTA Storage Ring*, Proc. 3rd Int. Particle Accelerator Conf. 2012, New Orleans, USA, 807 (2012).

[24] *http://www.dimtel.com/.*

[25] H. Wiedemann, *Particle Accelerator Physics*, Springer (2007).

[26] K. Wille, *The Physics of Particle Accelerators - An introduction*, Vieweg+Teubner (2000).

[27] E. Courant and H. Snyder, *Theory of the Alternating-Gradient Synchrotron*, Annals of Physics 281 (2000).

[28] W. Chao, *Handbook of Accelerator Physics and Engineering - Second Edition* , World Scientific (2013).

[29] K. Ng, *Physics of Intensity Dependent Beam Instabilities*, World Scientific (2006).

[30] B. W. Zotter and S. Kheifets, *Impedances and Wakes in High Energy Particle Accelerators*, World Scientific (1998).

[31] G. Rumolo, *Beam instabilities (I)*, CERN Accelerator School, Intermediate Level, Chios, Greece (2011).

[32] G. Rumolo, *Beam instabilities (II)*, CERN Accelerator School, Intermediate Level, Chios, Greece (2011).

[33] P. Wilson and J. Griffin, *High energy electron linacs: application to storage ring RF systems and linear colliders*, AIP Conference Proceedings 87, 450 (1982).

[34] R. H. Siemann, *Bunched Beam Diagnostics*, AIP Conference Proceedings, 430 (1989).

[35] P. Morse and H. Feshbach, *Methods of Theoretical Physics Part I*, Academic Press (1953).

[36] I. Gradshteyn and I. Ryzhik, *Table of Integrals, Series, and Products (7th Edition)*, Academic Press (2007).

[37] F. Pedersen and F. Sacherer, *Theory and Performance of the Longitudinal Active Damping System for the CERN PS Booster*, IEEE Transactions on Nuclear Science NS-24, 1396 (1977).

[38] R. D. Kohaupt, *Theory of Multi-Bunch Feedback Systems*, DESY 91-071 (1991).

[39] K. Balewski, *Review of Feedback Systems*, Proc. European Particle Accelerator Conference 1998, Stockholm, Sweden, 169 (1998).

[40] W. Barry et al., *Transverse coupled-bunch feedback in the Advanced Light Source (ALS)*, Proc. European Particle Accelerator Conference 1994, London, England, 122 (1994).

[41] S. Khan et al., *Commissioning Results of the Transverse Feedback System at BESSY II*, Proc. European Particle Accelerator Conference 2000, Vienna, Austria, 1912 (2000).

[42] D. Bulfone et al., *Operation of the Digital Multi-Bunch Feedback Systems at ELETTRA*, Proc. Particle Accelerator Conference 2003, Portland, USA, 3395 (2003).

[43] J. D. Fox et al., *Feedback Implementation Options and Issues for B Factory Accelerators*, SLAC-PUB-5932 (1992).

[44] S. R. W. Oppenheim, Alan V., *Discrete-Time Signal Processing*, Prentice Hall (2007).

[45] M. Lonza, *Multi-bunch Feedback Systems*, CERN Accelerator School, Chios, Greece (2011).

[46] P. B. Wilson, *Fundamental-Mode rf Design in e+ e- Storage Ring Factories*, SLAC-PUB-6062 (1993).

[47] MathWorks, *Matlab R2007b*, http://www.mathworks.com/ (2007).

[48] J. Byrd, *Simulation of the ALS Longitudinal Multibunch Feedback System*, Proc. Particle Accelerator Conference 1993, Washington DC, USA, 2349 (1993).

[49] M. Bassetti et al., *A Time Domain Simulation Code of the Longitudinal Multibunch Instabilities*, DAFNE Technical Note 1 (1993).

[50] S. Khan, *Simulation of longitudinal coupled-bunch instabilities in BESSY-II*, Proc. European Particle Accelerator Conference 1998, Stockholm, Sweden, 966 (1998).

[51] S. Prabhakar et al., *Phase Space Tracking of Coupled-Bunch Instabilities*, Phys. Rev. ST Accel. Beams 2, 084401 (1999).

[52] S. Prabhakar et al., *New diagnostics and cures for coupled-bunch instabilities*, PhD thesis, Stanford University (2001).

[53] D. Teytelman, *Architectures and Algorithms for Control and Diagnostics of Coupled-Bunch Instabilities in Circular Accelerators*, PhD thesis, Stanford University (2003).

[54] C. Sternemann et al., 10th DELTA User Meeting & Annual Report 2014, Technical report (2014).

[55] D. Schirmer, *Synchrotron radiation sources at DELTA*, Internal Report (2005).

[56] S. Khan et al., *Coherent Harmonic Generation at DELTA : A New Facility for Ultrashort Pulses in the VUV and THz Regime*, Synchrotron Radiation News 24, 37 (2011).

[57] C. Bazin and M. Billardon, *Optical Frequency Multiplication by an Optical Klystron*, Physical Review Letters 53, 2405 (1984).

[58] M. Labat et al., *Observation of Synchrotron Sidebands in a Storage-Ring-Based Seeded Free-Electron Laser*, Physical Review Letters 102, 2 (2009).

[59] G. De Ninno et al., *Generation of Ultrashort Coherent Vacuum Ultraviolet Pulses Using Electron Storage Rings: A New Bright Light Source for Experiments*, Physical Review Letters 101, 1 (2008).

[60] A. Schick, PhD thesis, TU Dortmund University (2015).

[61] *http://www.coherent.com/*.

[62] M. Höner et al., *A Dedicated THz Beamline at DELTA*, Proc. 2nd International Particle Accelerator Conference 2011, San Sebastian, Spain, 2939 (2011).

[63] P. Ungelenk et al., *Studies of Ultrashort THz Pulses at DELTA*, Proc. 5th Int. Particle Accelerator Conf. 2014, Dresden, Germany, 1936 (2014).

[64] *http://www.andor.com/*.

[65] A. Meyer auf der Heide et al., *Coherent Harmonic Generation at the DELTA Storage Ring: Towards User Operation*, Proc. 36th Free Electron Laser Conf. 2014, Basel, Switzerland, 1 (2014).

[66] M. Huck, *Characterization of VUV Pulses from the Short-Pulse Facility at DELTA and Steps towards Pump-Probe Experiments*, PhD thesis, TU Dortmund University (2015).

[67] *http://www.minicircuits.com/*.

[68] D. Teytelman and S. Jose, *Optimization of Bunch-to-Bunch Isolation in Instability Feedback Systems*, Proc. Int. Beam. Instrum. Conf. 2013, Oxford, UK, 116 (2013).

[69] *http://www.milmega.co.uk/*.

[70] *http://www.ar-deutschland.com/*.

[71] S. Khan et al., *Commissioning of the BESSY II Longitudinal Feedback System*, Proc. European Particle Accelerator Conference 2000, Vienna, Austria, 1903 (2000).

[72] *http://www.optronis.com/*.

[73] K. B. Unser, *The Parametric Current Transformer, a Beam Current Monitor Developed for LEP*, AIP Conference Proceedings, Virginia, USA, 266 (1992).

[74] J. Kettler et al., *Fast Beam Dynamics Investigation Based on an ADC Filling Pattern Measurement*, Proc. European Particle Accelerator Conference 2006, Edinburgh, Scotland, 1034 (2006).

[75] M. Switka et al., *Synchrotron Radiation Diagnostics Performance at ELSA*, Proc. 5th International Particle Accelerator Conference 2014, Dresden, Germany, 3473 (2014).

[76] M. Höner et al., *Investigation of Beam Instabilities at DELTA using Bunch-by-Bunch Feedback Systems*, Proc. 5th Int. Particle Accelerator Conf. 2014, Dresden, Germany, 3486 (2014).

[77] M. Höner et al., *Beam Diagnostics by Using Bunch-by-Bunch Feedback Systems at the DELTA Storage Ring*, Proc. 2nd Int. Particle Accelerator Conf. 2013, Shanghai, China, 485 (2013).

[78] R. G. Heine, *Untersuchung der longitudinalen Strahldynamik am Speicherring Delta*, PhD thesis (2000).

[79] M. Höner et al., *Bunch-by-Bunch Feedback Systems at the DELTA Storage Ring used for Beam Diagnostics*, Proc. 3rd International Beam Instrumentation Conference 2014, Monterey, USA, WEPD26 (2014).

[80] N. Abreu et al., *Longitudinal Dynamics with RF Phase Modulation in the Brazilian Electron Storage Ring*, Phys. Rev. ST Accel. Beams 9, 124401 (2006).

[81] D. Teytelman, *Injection Diagnostics using Triggered Bunch-by-Bunch Data Acquisition*, Proc. of DIPAC, Venice, Italy, 322 (2007).

[82] B. Riemann et al., *Model-Independent and Fast Determination of Optical Functions in Storage Rings via Multiturn and Closed-Orbit Data*, Phys. Rev. ST Accel. Beams 14, 062802 (2011).

[83] *EDM*, http://ics-web.sns.ornl.gov/edm/ (2015).

[84] *Experimental Physics and Industrial Control System*, http://www.aps.anl.gov/epics/ (2015).

C Acknowledgements

First of all I would like to thank Prof. Dr. Shaukat Khan for giving me the opportunity to work on this interesting topic. He gave me the chance to present my work at various conferences around the world. I am also grateful to Prof. Dr. Metin Tolan, who offered to be the second reviewer of my thesis.

The work would not have been possible without the continuous exchange and discussions with my colleagues at DELTA and other institutes. Especially, I would like to thank Malte Sommer for the fruitful discussions and the help during various night shifts. In addition, I would like to thank him and Dr. Peter Hartmann for their critical reading of parts of my thesis. The discussions with Dr. Dmitry Teytelman from Dimtel Inc. were also always a great help. Furthermore, I appreciate the discussions with Manuel Schedler and Michael Switka from ELSA, with Edmund Hertle and Dr. Nigel Smale from ANKA and with Dr. Andreas Schälicke from BESSY. Moreover, I would like to thank Peter Ungelenk and Carsten Mai for the fun we had in our common office.

I would like to thank my colleagues at DELTA for creating a nice working atmosphere, especially Fin Bahnsen, Jochem Friedl, Dr. Peter Hartmann, Svenja Hilbrich, Maryam Huck, Holger Huck, Benjamin Isbarn, Carsten Mai, Arne Meyer auf der Heide, Dr. Andre Nowaczyk, Bernhard Riemann, Dr. Helge Rast, Andreas Schick, Dr. Detlef Schirmer, Dr. Gerald Schmidt, Gerrit Schünemann, Dr. Gholamreza Shayeganrad, Malte Sommer, Patryk Towalski, Peter Ungelenk and Prof. Dr. Thomas Weis.

I would like to express my gratitude to all the technicians and engineers, who keep DELTA running week by week. Especially, I want to thank Wolfgang Brembt and Vadim Kniss for their help concerning electronics equipment.

Thanks to Petra Lindemann and Monika Voits-Besli for their support in administrative affairs.

The cooperation with the DELTA user community was always pleasant and thus I want to thank Dr. Stefan Cramm, Dr. Sven Döring, Dr. Michael Paulus and Dr. Christian Sternemann.

I would like to acknowledge the financial support of the TU Dortmund University, the DFG and the BMBF.

I am very thankful to my parents and my brother for their continuous support.

I am extremely grateful to my beloved Katrin for her enormous patience during the writing process of my thesis and for her continuous support and encouragement.